Phase retrieval methods in inline-holography

zur Erlangung des
Doktorgrades Dr. rer. nat. der Fakultät für
Naturwissenschaften der Universität Ulm
vorgelegt von

Amin Parvizi
aus Boyerahmad

Institute of Experimental Physics
Ulm University
Germany
2016

Dean of faculty of natural sciences: Prof. Dr. Peter Dürre

1. Gutachter : Prof. Christoph T.Koch. PhD
2. Gutachter : Prof. Dr. Ute Kaiser

Tag der Promotion: 09.05.2016

Abstract

Quantitative phase imaging, i.e. the detection of the phase delay imposed by a biological cell or thin transparent sample on the incoming electromagnetic wave, allows not only to visualize the otherwise hidden structure of a sample under investigation but also, observe and study the dynamics of refractive index and thickness fluctuation. One well-known approach toward phase reconstruction based on images acquired at different planes of focus is to solve the transport of intensity equation (TIE), which, owing to its simple mathematical formulation and straight forward procedure of acquiring the corresponding experimental data, has gained attention at different research communities over the past decades.

The TIE is a second order, elliptical, non-separable partial differential equation which relates the intensity variation along the optical axis to a Laplace-like function of the phase and yields a unique solution for the phase, provided the measured intensity at the principle plane is strictly positive and the boundary conditions are well defined. However, boundary conditions are not accessible in general and therefore, the TIE is ill-conditioned and the solution is not unique. In order to get around the problem of non-uniqueness and ill-conditionedness of the TIE, different algorithm are presented throughout my thesis.

The first algorithm presented in this research work to solve the TIE is based on the prior knowledge of free area in the image plane. This is realized by applying Dirichlet boundary conditions on the perimeter of a polygon where the phase is constant. The Neumann boundary condition is imposed to the boundary of the padded area. The TIE is solved by the finite element method in which a multigrid solver is employed in order to minimize the computation time.

The second approach towards phase retrieval from intensity measurements is called the Gradient Flipping (GF) algorithm, in which the l_0 norm of the gradient of the phase. To accomplish this task, an algorithm devised to combine the well-known fast Fourier transform (FFT) solution of the TIE with the constraint projection principle adapted from the charge flipping algorithm. In an iterative manner, the boundary condition is updated in such way that consistency between experimental data and reconstructed phase is assured. The algorithm iterates until convergence is reached. Experimental demonstration shows the superiority of the GF algorithm over the conventional FFT solution to the TIE and a l_1 minimization approach.

Finally, unlike the TIE which relies on defocused intensity measurements, a new approach based on the astigmatic intensity equation (AIE) which relies on intensity measurements at different angle of a rotating cylindrical lens is presented. The AIE offers an over-determined system of equations . An iterative algorithm based on a FFT-approach to solve the AIE has been developed. Numerical experiments demonstrate its capability to reconstruct the phase of weakly scattering object.

Declaration

I hereby declare that I wrote the present dissertation with the topic: “Phase retrieval methods in inline-holography” independently and used no other aids than those cited.
Ulm, Feb. 2016
Amin Parvizi

Acknowledgements

I would like to express my sincere gratitude to Prof. Dr. Christoph T.Koch for providing me with the opportunity to complete my PhD thesis at Ulm University and supporting me throughout the period of doing this research. His unique character was a great shelter in the time of storm. The door to his office was always open whenever I faced with obstacles or difficulties in research or drafting manuscripts. I could not have imagined having a better supervisor for my Ph.D.

My special thanks goes to Dr.Wouter Van den Broek for the stimulating discussions and insightful comments which incented me to look at the problems from various prospective. Besides, I am grateful to Dr. Stefan A.Funken for the fruitful discussions s well as promoting my knowledge in finite element approach.

I would like to thank my colleagues, Dr. Robert S. Pennington, Feng Wang and Johannes Müller for their help, support, kindness, and for all the fun we have had in the last four years.

Many thanks go to my friends, Farid Farajollahi, Parisa Bakhtiarpour, Parisa Eshraghi, Behrouz Alambeigi and Hadi Mohammadzadeh for supporting me through the Ph.D studies.

Last but not least, I express my very profound gratitude to my parents as well as my siblings for their continuous encouragement and unfailing support.

Contents

List of Figures

List of Tables

Chapter 1

Introduction

1.1 Introduction

The structure of most biological samples illuminated by visible light (e.g. light microscopy) or electrons (e.g. transmission electron microscopy) is not clearly visible due to the intrinsic low contrast of the sample. Moreover, many samples illuminated by neutrons show a weak intensity contrast which makes a difficult to observe the hidden structure of the under investigation object [5]. Furthermore, in the context of adaptive optics, i.e. a technology which aims at correcting the wave-front distortion, phase of incident light coming from far objects (e.g. stars, planets) suffers from severe distortion which degrades the quality of acquired images and real time observation [5] . Thus, phase measurement and visualization is a key step toward revealing the hidden information.

An electromagnetic wave is defined uniquely at any position and time by its modulus and phase, however, the phase information is lost upon measurement. Therefore, techniques and methods have been developed to retrieve the phase indirectly. Generally speaking, approaches toward phase reconstruction subsume under two distinct categories, namely, phase-sensitive imaging and phase measurement [5]. The approaches fallen in the first class are not capable of providing quantitative information and therefore, are qualitative, although these methods portray an unknown phase by transforming the intensity distribution to a phase map. Examples of this class are Zernike phase contrast [6], differential interference contrast [7] and Hoffman phase contrast [8]. In contrast to the first class, the techniques fallen in the second category not only visualize the phase distribution but also, provide quantitative data for the corresponding phase distribution. Interferometry [9], through-focal series [10, 11], transport of intensity equation [12] are examples of this class.In what follows we restrict our attention to the transport of intensity equation approach toward quantitative phase measurement.

The transport of intensity equation (TIE) approach is an active field of research which has opened new vistas to the researchers of different disciplines. Fig.1.1(a) shows the number of papers published per year concerning the TIE over the course of the past 20 years. Moreover, Fig.1.1(b) illustrates the number of citations at the same period which mirror the facts that not only, the TIE became a promising approach with widespread application, but also, there is an ongoing research to develop and extend the potential of the TIE [13].

TIE offers fairly easy experimental setup as well as straight-forward mathemat-

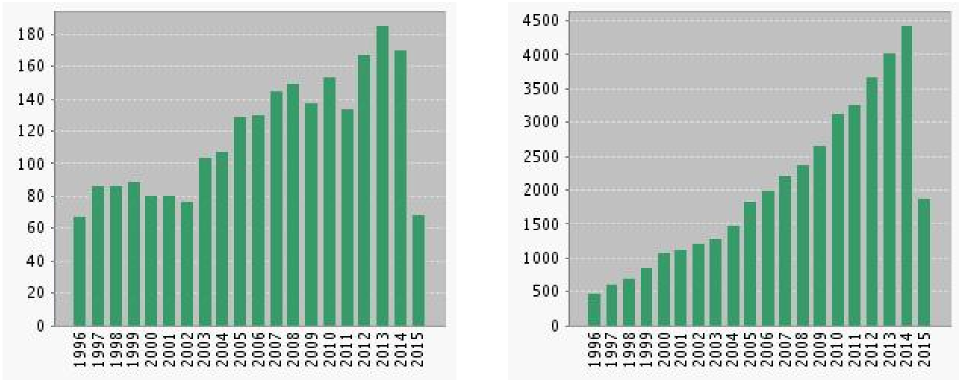

(a) (b)

Figure 1.1: Publications on the TIE: a) Published papers in each year. b) Citations in each year

ical description in which the phase of electromagnetic wave traversing through a weakly absorbing object is related to the intensity variation along the optical axis at the transverse plane from which the hidden structure is revealed. Assuming a spatially coherent source and paraxial approximation, the TIE, first derived by M. R. Teague, reads as [12],

$$\vec{\nabla}_{\perp} \cdot \left[I\left(\vec{r}_{\perp}, z\right) \vec{\nabla}_{\perp} \varphi\left(\vec{r}_{\perp}, z\right) \right] = -k \frac{\partial I\left(\vec{r}_{\perp}, z\right)}{\partial z} \tag{1.1}$$

where $k = \frac{2\pi}{\lambda}$ is the wavenumber, $\vec{r}_{\perp}$ is a vector in the plane perpendicular to the z-direction and $\vec{\nabla}_{\perp}$ denotes the Laplacian operator in the transverse plane. Furthermore, $I\left(\vec{r}_{\perp}, z\right)$ is the intensity in the principle (focused) plane and $\varphi\left(\vec{r}_{\perp}, z\right)$ denotes the unknown phase map. For strictly positive intensities the second order, non-separable and elliptical differential equation has a unique solution up to an additive constant when appropriate boundary conditions met. However, the presence of zeros in the intensity plane causes vortices in the phase distribution map from which, generally, a unique solution can not be acquired [14].

1.2 Illumination Source

The TIE is derived under the coherent illumination source assumption, however, most of the physically available sources are not perfectly coherent. Partially spatially coherent sources such as the Shell-model-type [15] may prevent speckle noise and reduce cross-talk effects[16], but they also, in some cases, neutralizes Fresnel diffraction which degrades the reconstructed phase image quality[17].

Under the assumption of a perfect imaging system and within a small defocus range, reconstructed phases are identical, independent of whether we have a coherent or partially coherent illumination source [18, 19]. D. Paganin and K. A. Nugent showed that it is possible to relate the scalar phase to the normalized transverse energy flux from which the recovered phase of the TIE under coherent illumination is interpreted as a real-valued scalar quantity whose gradient represents the Poynting vector [20]. Later, T. E. Gureyev *et al.* extended the idea of the scalar phase as a generalized eikonal to describe the evolution of the time-averaged intensity of the partially coherent field [21]. However, notably, the generalized eikonal [21] is an approximate solution to the eikonal equation for fully coherent field in the limit of the short wavelength [22, 23].

In the limit of first order approximation of the transfer cross coefficient [24] , a Gaussian enveloped is assumed to model the partial coherent illumination from which A.V. Martin *et al.* in 2006 has derived a modified version of the TIE which is non-linear to phase[25]. In 2008, C.T.Koch suggested an approach which preserves the flux between images measured at different defoci from which the induced error by partially coherent illumination on the reconstructed phase is reduced [26]. Moreover, this approach is insusceptible to the shape of the illumination source. Later, Zysk*et al.* employed the coherent mode decomposition [27] to decompose the cross-spectral-density to the superposition of the weighted coherent modes from which the TIE for partially coherent source has derived [28]. However, the modified TIE reconstructs the phase of the sum of the coherent fields and the phase of individual modes can not be retrieved from single TIE measurement[23]. Optical path length of a thin sample illuminated by a partially coherent source can be determined by the extended version of the TIE suggested by [23] which is valid for a small defocuse range provided the properties of the illumination source are know in prior. Recently, a Kalman filter[29] based approach is suggested by [30] to incorporate the characteristic of the illuminating source for large defocuse range in which convolution operator acts to model the coherence effect. More recently, in contrast to time-space representation of partially coherent illumination such as mutual intensity and cross spectral function, the phase-space framework based on the Wigner distribution function[31] is suggested by [32] from which the TIE is reformulated. In the phase-space perspective, the phase of the incident partially coherent beam can be deemed as a scalar potential whose gradient leads to an ensemble-averaged transverse energy flux vector.

1.3 Solver and Boundary Conditions

The TIE relates the axial intensity variation along the optical axis orthogonal to the direction of propagation to the Laplacian of the phase. Being a second order, non-separable, elliptical partial differential equation, it has a unique solution (up to an additive constant) for strictly positive measured intensities when appropriate boundary conditions (BC) are met [33]. However, the presence of zeros in the intensity plane entails singularities in the phase map [34]. L.J. Allen *et al.* introduced a modified version of the TIE which accounts for first order vortices [14]. Later, A. Lubk *et al.* suggested an algorithm in which the appropriate BC is defined based on topological charge and large defocus acquired image intensities are employed to ensure the accuracy of the reconstruction result [35].

Assuming the gradient of intensity is parallel to the gradient of the phase [36] and Dirichlet BC , a Green's function solution to the TIE first proposed by M. Reed Teague [12]. Notably, the validity of Teague's solution has been extensively examined for various experimental scenarios and sufficient conditions have been derived which ensure the accuracy of the reconstruction via Teague's approach [37]. Although the application of the Zerinke polynomials has been known in optical studies [38], T. E. Gureyev *et al.* provided a comprehensive understanding of the mathematical solution of the TIE with respect to Zernike polynomials based on a decomposition of the TIE into a series of Zernike functions for the case of a uniform illumination source[39]. This research work was extended further and suggested an approach based on an orthogonal series expansion which helps not only, to reconstruct the phase under non-uniform illumination source but it also, eliminates the need for an explicit BC [40]. Although the orthogonal series expansion based approaches were capable to visualize the phase, the boundary slope measurement has introduced serious difficulties [41, 42], however, in some cases, this measurement might be neglected[43, 44].

F. Roddier and C. Roddier proposed an iterative scheme based on the Fast Fourier transform (FFT) to reconstruct the phase in the context of adaptive optics in astronomy [45]. Later, T.E. Gureyev and K.A. Nugent generalized the idea of Fourier harmonics [46] and pointed out that the FFT alone can be applied to the TIE which yields a unique solution under fairly general conditions [42]. Although the FFT-based approach is computationally fast, the reconstructed phase suffers from low spatial frequency artifacts due to the periodicity inherent to the FFT approach in the case of non-periodic object. Furthermore, the quality of retrieved phase is considerably degraded in the presence of noise [14, 42]. It is worth noting that for the objects characterized by strong absorption, the solution of the FFT approach for the TIE does not coincide with the exact one owing to the negligence of the rotational flux vector which is inherent to the TIE derivation. Therefore, an extra condition was suggested which results in the phase discrepancy elimination [47]. The FFT-based symmetrization approach to the TIE, proposed by V.V. Volkov *et al.* suggests a symmetric extensions paradigm in which a recorded image extends with respect to either the mirror plane or the intrinsic symmetry of the TIE, then the FFT algorithm is employed to reconstruct the phase. Although for periodic objects, the original FFT approach yields an exact solution , this symmetrization scheme yields an approximate solution for the case of non-periodic object[4]. In most experiments the assumption of periodic boundary conditions inherent to the FFT approach is violated. Recently, C. Zuo *et al.* reformulated the TIE as an inhomogeneous Neumann boundary value problem in the presence of a hard-edge aperture which is valid for the case of uniform and non-uniform illumination source. Furthermore, they showed rather than a direct attack to the TIE, applying the discrete cosine transform to the Green's function solution of the reformulated TIE helps to eliminate the necessity of a detection-purpose scheme to differentiate the boundary signal from the interior's one [48].

Since the Laplacian operator is ill-conditioned near and at zero spatial frequency, a Tikhonov regularization characterized by a regularization parameter α [49] was suggested to improve the reconstruction quality by filtering out the low frequency artifact at atomic resolution [50]. To do this, The regularization parameter is chosen by comparing the reconstructed phases at different $\alpha-$vlues. It was demonstrated experimentally that although the Tikhonov regularization approach improves the quality of the retrieved phase profile, a loss of phase detail was still evident [51]. An alternative approach which not only reconstructs the phase profile, but also removes the low frequency artifacts,suggested by L. Tian *et al.* at MIT [52], is to reformulate the TIE in the context of a minimization problem which yields a partial differential equation for non-linear diffusion (NLD) denoising. Furthermore, the sum of magnitudes of the phase gradient is defined as the total variation and NLD denoising thus helps to eliminate low spatial frequency artifacts. Bearing in mind that the

NLD regularization approach is not a convex problem, the obtained phase is an approximate solution to the TIE. In the context of tomography, a discretized operator is formed consisting of the TIE and a transform in the Fourier domain from which a compressive reconstruction model is suggested [53]. A two-step iterative shrinkage/thresholding algorithm then yields the solution [53, 54]. Rather than the phase gradient, E. Froustey *et al.* suggested to define a regularization function base on the eigenvalue of the structure tensor from which the acquired energy minimization problem can be solved by applying the alternating direction method of multipliers [55].

In contrast to the FFT approach which portrays an approximate solution to the TIE, the multigrid solver results in an exact solution [14]. Multigrid algorithms are based on a hierarchy of grids which speed up the convergence rate of iterative solutions of the elliptical partial differential equation by iterating between fine and coarse mesh thus reducing the residual error effectively[56]. In the context of the TIE, however, the boundary condition is not known in prior and therefore, a periodic boundary condition with a constant value is assigned to the rectangular perimeter of the reconstruction phase map in [14]. Implementing the full multigrid algorithm as the preconditioner of the conjugate gradient method leads a further acceleration in convergence computation rate [57]. Recently, a finite-element discretization based method was proposed in which not only the Dirichlet BC to a polygon outlining the free area is imposed but also, a Neumann BC is defined on the padded perimeter of the field of view. Furthermore, a multigrid solver was utilized to improve the speed of convergence [58].

One major drawback of the direct reconstruction methods stems from the fact that prior information which assists to reduce the possible solution space, is difficult to be included [59]. Moreover, incorporating the TIE in iterative algorithms extends the validity range of the TIE [59, 60]. It was shown that Gerchberg–Saxton– Fienup type of algorithms [61] can be used to refine the TIE reconstructed phase[60]. In contrast to aforementioned nonlinear iterative algorithms, TIE can be combined with the first-order Born approximation from which a linear iterative approach has been devised [59]. Furthermore, it was shown that in the limit of small distances for mixed objects, the TIE solution does not match with that of the contrast transfer function (CTF) and therefore, an extension to the CTF is required[62–64].

1.4 Estimation of axial intensity variation

Accurate estimation of the axial intensity variation occurring in the right hand side of the TIE, plays a prominent role in a precise reconstruction of the phase of the object under investigation. Since it is not possible to directly record the intensity derivative along the optical axis, a finite difference scheme is employed. Mathematically, the accurate estimation of the irradiance variation along the optical axis is obtained when the defocus difference tends to zero. However, from a physical perspective, although a small defocus provides high spatial frequency information, the measurements tend to be noisy. In contrast to small defocus, images recorded at large defoucs difference would be less influenced by noise at the cost of losing high spatial frequency information.

As early as 1987, D.Van Dyck and W.Coene [65] have derived an analytical formula in which the upper bound of defocus is estimated for the case of two images captured at equal distances with respect to the principle plane (focused plane) by assuming a linear approximation to the defocus. However, for the same scenario, this can be further improved by computing the residual error term between a derivative and a finite difference formula [50]. The lower bound of the defocus is estimated by assuming a minimum Michelson visibility of 3% [66]. The upper and lower limit of defocus for the case of three symmetric images recorded with of coherent and incoherent illumination are summarized in [25]. In addition, M.Soto et al.[67] introduced the variance of the local axial derivative of the intensity as a function of two distinct variables, namely, random noise and separation distance between different state of focus. Assuming an uncorrelated random noise with zero mean, a mathematical formula is presented to determine the optimum defocus value based on the local phase analysis. Moreover, the error in the finite difference estimation of intensity variation is sandwiched between lower and upper limit. It is worth noting that the aforementioned analysis relies on the prior knowledge of phase. Later, they improved the axial intensity derivative by using the first order terms in the Taylor expansion [68]. This work has been expanded on recently by J. Martinez-Carranza et. al. [69] in that an analytical expression is provided to determine the optimum plane separation .

However, the two-image equally-spaced approach is a simple and straightforward approach which has second-order precision. These calculations suffer from not only non-linearity due to the higher order terms of the Taylor expansion but also, the measurements are vulnerable to noise. Therefore, an optimum defocus distance is needed to balance the noise effect on the measurements and the spatial frequencies still being transferred. The group of L.Waller [70] at MIT published a research work mitigating the non-linear effect of higher order intensity derivative by recording images at multiple equally spaced planes. Two different approach to the first order estimation of the axial intensity variation is brought to attention. The first method which is susceptive to noise computes a weight to each distinct measurement in such a way that higher order terms in Taylor series cancel out. To do so, the set of linear equations is solved by exploiting the Vandemonde matrix as a coefficient matrix. This work was extended later in [71] for the general case of unequally spaced sample measurements. However, the second approach which outperforms the earlier, relies on a higher order polynomial fit. Firstly the curve of intensity variation along the propagation axis for each pixel in the image plane is obtained, then, a higher order polynomial paradigm to accurately model the stack of provided curves is employed. Hence, the first order derivation can be computed. Although including higher order terms yields a more precise reconstruction, this comes at the cost of higher computation time. Notably, using only the first order terms, the second approach resemble the proposed technique in Ref. [68]. Further improvement of the estimation of the axial intensity derivative has been carried out by minimizing the mean squared error between estimated and measured intensity derivative. In order to mitigate the effect of noise on the approximate axial intensity variation, a nonlinear set of equation should be solved. A Lagrange multiplier approach is employed to solve the nonlinear optimization problem [72]. Since the measurements sampled unequally, this approach can be thought of as a generalization of an approach in [68] which assumes an equally sampled measurement. Notably, some researchers propose exponentially-spaced measurements [73]. It can be shown there is an optimal degree of polynomial fit for the specified number of measurements in which a minimum error can be achieved [74].

Although the aforementioned approaches are capable of reasonably recovering phase, but their performance depends strongly to the noise level and the spatial frequency characteristics of the sample. From the digital signal and processing perspective, all the multiple-plane-based and two plane-based measurement approaches can be categorized as a spacial form of Savitzky-Golay differentiation filter ($SGDF$) [75]. Based on this perspective, two paradigms are presented in [76]. In the first approach optimal degree of SGDF, equivalent to the optimum degree of a ploynominal which reconstructs the measurements, is chosen in such a way that the variance remains either constant or without considerable drop as the degree of ploynomial is elevated. However, the main drawback of this method lies in the fact that the fine structure of the retrieved phase image is degraded by the lower ploynomial order and the higher polynomial order reconstructs cloudy phase images. A second method relies an optimal frequency selection (OFS) thus overcoming the difficulties of the first method. The OFS approach consist of three parts, firstly, the intensity derivative is estimated with various degree of SGDF, then, the Fast Fourier transform is utilized in conjunction with a complementary filter bank with a specified cut off frequency for each respective degree of SGDF to reconstruct the phase. Finally, summing up all the reconstructions lead to the final phase.

A recent research work [77] proposes an approach to compute the axial intensity derivative without scanning along the propagation direction. To do this, a pair of encoded images, produced by placing two patterns, namely, u pattern and v pattern, in the aperture plane is recorded. Then, the partial derivatives along the transverse direction of the captured pair images estimates the axial intensity derivative. It is worth noting that a chromatic aberrations based approach based on different irradiation wavelengths is capable of retrieving the phase without scanning the propagation direction. However, a modified version of the TIE should be employed for each respective method [78, 79].

1.5 Application

1.5.1 Phase Retrieval with neutrons

The neutron is a neutral subatomic particle which consist of one up quark and two down quarks with a mass of almost one atomic mass unit. In contrast to X-ray radiation which interacts with the shell of electrons of the atom, neutron scattering is not related to the electron density of the object of interest. This is due to the fact that neutron beam interacts with the core and the magnetic momentum of the atoms [80]. The technique aiming at imaging an object of interest with neutrons is known as " Neutron imaging".

Although neutron interferometry techniques have proven to be successful [81], the associated technical complexity restricts phase imaging studies thus, introducing non-interferometric techniques as a viable and feasible alternative. B.E. Allman *et al* demonstrated experimentally that a TIE based neutron radiography phase reconstruction approach provides quantitative phase at low radiation doses which is difficult to be retrieved by other conventional methods [82]. Later, E. Lehmann *et al.* pointed out that the TIE can be exploited to reconstruct the phase of each slice of a neutron radiography tomographic data set which allows to assign a real and imaginary part of the neutron refractive index to each voxel from which the separation of materials is possible when the conventional tomography methods fail [83].

1.5.2 Phase Retrieval with Electrons

The TIE has been applied to images taken by modes of transmission electron microscopy (TEM) that keep magnetic fields away from the specimen, known as Lorentz microscopy mode, a technique which extensively has been exploited to investigate magnetic domains and vortices in thin magnetic films as well as superconductors[5, 84]. It is worth noting that the Laplacian of the phase of a magnetic structure is related to the Ampèrian current density component in the direction parallel to the incoming electron beam [85]. M. D. Graefa and Y. Zhu have applied the TIE to a series of Lorentz images of Permalloy film acquired by a JEOL4000 EX TEM operated at 400 keV and show that the reconstructed phase based on TIE is in reasonable agreement with the input phase from which the magnetic components were calculated [86]. Y.Zhu *et al* suggested to combine the TIE with holography to overcome the limitation of holography, such as the necessity of being near a vacuum area for a reference wave as well as the restricted field of view [87]. Later, V.Volkov and Z.Zhu have derived the magnetic transport of intensity equation (MTIE) based on the TIE from which the magnetization profile of a hard magnet sample (Nd-Fe-B) was reconstructed [88]. Except for very small magnetic nano-particles as well as neglecting electrostatic phase contribution to the total phase shift, the MTIE offers an accurate insight into magnetic Lorentz microscopy [88]. In order to distinguish between the contribution of the electrostatic potential to the total phase shift from that of the magnetic field, A. Kohn *et al* proposed an energy-dependent TIE scheme [89]. Bearing in mind that the contribution of electrostatic potential to the total phase shifts varies with kinetic energy of the incident electrons, the suggested scheme recognizes the contribution of electrostatic potential thus subtracting it from the retrieved phase, result in the magnetic induction field. This method not only can be exploited to identify the features originated from magnetic potential but also, successfully reconstructs the phase where the electrostatic potential is substantial [89]. In addition to the approach suggested by A.Kohn *et al*, E.Humphrey *et al* proposed two distinct TIE-like differential equation with associated Tikhonov regularization parameter to differentiate between the electrostatic potential contribution to the total electron phase shift from the magnetic one [90]. Later, L.A. Rodríguez *et al* applied the TIE approach to a sequence of cobalt L-shaped nanowire images recorded by Lorentz TEM to maximize the nucleation field by optimizing the width and thickness of the nanowire [91]. Recently, the TIE was utilized to retrieve the magnetic induction profile from a through focal series of cobalt antidot array with fixed hole diameter acquired by high resolution *in situ* Lorentz microscopy [92].

Furthermore, T.C.Petersen *et al* applied the TIE to a through focal series of images of a polyhedral nano cube namely, MgO, from which the morphology of the nano particle was visualized [93]. Noticeably, it was experimentally demonstrated that, despite the presence of experimental challenges such as charging of the non particles as well as substrate degradation, the reconstructed phase is in good agreement with that of electron holography. Later, T.C.Petersen *et al* suggested the TIE based phase retrieval approach for mapping surface plasmon excitations of metal nanoparticles [94]. However, V. J. Keast *et al* pointed out that the subtle particle instabilities under the incident electron beam as well as diffraction contrast fluctuations gave rise to discrepancies between the reconstructed phase distribution computed from the experimental gold nano particles through focal series data set and the expected theoretical profile [95].

1.5.3 Phase Retrieval with X-rays

In contrast to neutron and electron radiation, X-ray radiation interacts with the electron shell of atoms [80]. Depending on the photon energy, X-ray radiation is categorized into two distinct group namely, hard X-ray and soft X-ray. X-rays with photon energies below 5-10 keV are known as soft X-rays which have low penetrating capability and are highly absorbed in air. In contrast to soft X-ray, hard X-ray photons possess energies above 5-10 keV which increase the capability of penetration thus more easily capable of revealing the hidden structure of objects [96]. It worth noting that, the TIE based phase reconstruction approach in hard X-ray region is challenging on the account of the lack of suitable optical elements such as lenses [79].

K. A. Nugent *et al* published the first experimental demonstration of quantitative phase reconstruction from hard X-rays with beam energy of 16 keV using the TIE formalism [5, 46]. Later, T. E. Gureyev *et al* reconstruct the phase of a polystyrene sphere with negligible absorption using higher energy, 19.6 keV, hard X-ray radiation [97]. In the context of medical science, A. F. T. Leong used the TIE based X-ray phase contrast imaging approach to measure the air volume in a lung [98]. Using high energy X-rays (20 keV photons) with an energy spread of $1e^{-4}$ the phase of Xenopus laevis embryo at the 4-cell stage was retrieved via TIE and quasiparticle approach in which the latter approach outperformed the TIE in retrieving high spatial frequency information thus yielding increased spatial resolution [99].

Furthermore, the TIE has been applied to X-ray tomographic data to reconstruct the 3D phase from which the refractive index of the object under investigation is computed. M. Langer *et al* demonstrated numerically and experimentally that in comparison to the CTF approach as well as Bronnikov method which combines the TIE with the inverse Radon transform [100], TIE preforms better for noise free data or where the low dose deposition is substantial due to that fact that fewer image is needed [101]. However, mixed approach (CTF+TIE) [62] is robust against noise on account of several images taken at different plane of focus which facilitate the convergence. Assuming near a field approximation together with prior knowledge of refractive index of each presented material as well as the thickness of the object at distinct angle, M. A. Beltran *et al* suggested an iterative algorithm based on the TIE which reconstructs the phase of a multi-material object from a single tomographic data set [103, 104].

1.6 A brief review of the wave theory of optical image system

In the following sub-section, the mathematical backbone of the optical image system is reviewed with the emphasize on the mathematical formulation of the Fresenel and the Fraunhofer diffraction pattern. The material of this sub-section is based on [1].

The complex representation of a monochromatic wave traveling along the optical axis, z , with the wave vector $\vec{k}$, where $\|\vec{k}\| = \frac{2\pi}{\lambda}$ and has direction cosines, as shown in Fig. 1.2, may be written as

$$U(x, y, z; t) = \exp\left[i\left(\vec{k}\cdot\vec{r} - 2\pi\upsilon t\right)\right] \tag{1.2}$$

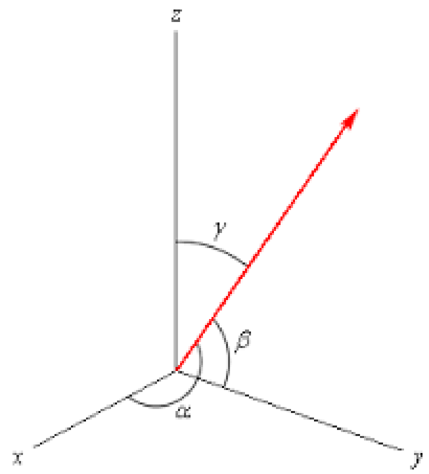

Figure 1.2: Graphical representation of direction angles.

where $\vec{k} = \frac{2\pi}{\lambda}(\alpha\hat{x} + \beta\hat{y} + \gamma\hat{z})$ as well as $\vec{r} = x\hat{x} + y\hat{y} + z\hat{z}$ is the position vector. Dropping the time dependence term of the complex representation, the complex phasor amplitude representation across the z-constant plane along the direction of propagation is given by

$$U(x, y, z) = \exp\left[i\vec{k}.\vec{r}\right] = \exp\left[i\frac{2\pi}{\lambda}(\alpha x + \beta y)\right]\exp\left(i\frac{2\pi}{\lambda}\gamma z\right) \tag{1.3}$$

Notably, γ is related to α and β through the following relation

$$\gamma = \sqrt{1 - \alpha^2 - \beta^2} \tag{1.4}$$

The Fourier transformation of the function U across the (x, y) plane at $z = 0$ is given by

$$A(f_x, f_y; 0) = \int\int U(x, y; 0)\exp\left[-i2\pi(f_x x + f_y y)\right]dxdy \tag{1.5}$$

where f_x and f_y are the variables conjugate to x and y, respectively. Comparing the exponential function $\exp\left[-j2\pi(f_x x + f_y y)\right]$ with Eq. 1.3 suggests that the exponential function might be considered as a plane wave traveling along the optical axis with the following parameters

$$\alpha = \lambda f_x \quad \beta = \lambda f_y \quad \gamma = \sqrt{1 - (\lambda f_x)^2 - (\lambda f_y)^2} \tag{1.6}$$

Therefore, the Fourier transform of the function U is rewritten as

$$A\left(\frac{\alpha}{\lambda},\frac{\beta}{\lambda};0\right)=\int\int U\left(x,y;0\right)\exp\left[-i2\pi\left(\frac{\alpha}{\lambda}x+\frac{\beta}{\lambda}y\right)\right]dxdy \tag{1.7}$$

and the function $A\left(\frac{\alpha}{\lambda},\frac{\beta}{\lambda};0\right)$ is called the angular spectrum of the optical wave $U(x,y;0)$.

In order to draw a relation between the initial angular spectrum, $A\left(\frac{\alpha}{\lambda},\frac{\beta}{\lambda};0\right)$, and the angular spectrum along the optical axis across the (x,y) plane at an arbitrary distance z, $A\left(\frac{\alpha}{\lambda},\frac{\beta}{\lambda};z\right)$, the optical disturbance $U\left(x,y,z\right)$ is written

$$U\left(x,y,z\right)=\int\int A\left(\frac{\alpha}{\lambda},\frac{\beta}{\lambda};z\right)\exp\left[i2\pi\left(\frac{\alpha}{\lambda}x+\frac{\beta}{\lambda}y\right)\right]d\frac{\alpha}{\lambda}d\frac{\beta}{\lambda} \tag{1.8}$$

In addition to the above relation, the optical wave U should also satisfy the source-free Helmholtz equation; that is

$$\left(\nabla^2+k^2\right)U=0 \tag{1.9}$$

Substituting Eq. 1.8 into the Helmholtz equation, namely Eq. 1.9, results in the following second order differential equation for the unknown $A\left(\frac{\alpha}{\lambda},\frac{\beta}{\lambda};z\right)$; that is

$$\frac{d^2}{dz^2}A\left(\frac{\alpha}{\lambda},\frac{\beta}{\lambda};z\right)+\left(\frac{2\pi}{\lambda}\right)^2\left[1-\alpha^2-\beta^2\right]A\left(\frac{\alpha}{\lambda},\frac{\beta}{\lambda};z\right)=0 \tag{1.10}$$

the solution to the equatio 1.10 can be written in the form of the exponential function; that is

$$A\left(\frac{\alpha}{\lambda},\frac{\beta}{\lambda};z\right)=A\left(\frac{\alpha}{\lambda},\frac{\beta}{\lambda};0\right)\exp\left(i\frac{2\pi}{\lambda}\sqrt{1-\alpha^2-\beta^2}z\right) \tag{1.11}$$

which states that if the direction cosines condition, namely $\alpha^2+\beta^2<1$, is satisfied then the various components of the angular spectrum experience a change of the phase shift over the course of distance z.

However, when $\alpha^2+\beta^2>1$, the right most term turns to a real number and the Eq. 1.11 can be written as

$$A\left(\frac{\alpha}{\lambda},\frac{\beta}{\lambda};z\right)=A\left(\frac{\alpha}{\lambda},\frac{\beta}{\lambda};0\right)\exp\left(-\mu z\right) \tag{1.12}$$

where

$$\mu=\frac{2\pi}{\lambda}\sqrt{\alpha^2+\beta^2-1}$$

μ is a positive real valued number which indicates that the components of the wave which do not satisfy the direction cosines condition will be swiftly attenuated over the course of propagation where no energy is transported. Such a component of the wave is called evanescent wave.

Considering Eq. 1.11, it is now possible to relate the disturbance U across any arbitrary plan (x,y) at distance z to the initial angular spectrum; that is

$$\begin{aligned}U\left(x,y,z\right)=\int\int A\left(\frac{\alpha}{\lambda},\frac{\beta}{\lambda};0\right)\exp\left(i\frac{2\pi}{\lambda}\sqrt{1-\alpha^2-\beta^2}z\right)\times\\ \mathrm{CIRC}\left(\sqrt{\alpha^2+\beta^2}\right)\exp\left[j2\pi\left(\frac{\alpha}{\lambda}x+\frac{\beta}{\lambda}y\right)\right]d\frac{\alpha}{\lambda}d\frac{\beta}{\lambda}\end{aligned} \tag{1.13}$$

where the CIRC function is defined as

$$\operatorname{CIRC}\left(\sqrt{\alpha^2+\beta^2}\right)=\begin{cases}1 & \sqrt{\alpha^2+\beta^2}=1\\ 0 & \text{Otherwise.}\end{cases} \tag{1.14}$$

which restricts the region of the calculation to the region where the direction cosines condition is satisfied. In other words, only those component of the angular spectrum which satisfies the direction cosines condition contributes to the optical wave U and those which satisfy the evanescent wave condition will be eliminated by the CIRC function.

Substituting Eq. 1.6 into the right-hand side of Eq. 1.14 results in

$$\begin{aligned} U(x,y,z)=\int\int A(f_x,f_y;0)\exp\left(i\frac{2\pi}{\lambda}\sqrt{1-(\lambda f_x)^2-(\lambda f_y)^2 z}\right)\times \\ \operatorname{CIRC}\left(\sqrt{(\lambda f_x)^2+(\lambda f_y)^2}\right)\exp\left[i2\pi\left(f_x x+f_y y\right)\right]df_x df_y \end{aligned} \tag{1.15}$$

In addition, if we let the angular spectrum of $U(x,y,z)$ to be shown again with $A(f_x,f_y;z)$, then $U(x,y,z)$ may be written as

$$U(x,y,z)=\int\int A(f_x,f_y;z)\exp\left[i2\pi\left(f_x x+f_y y\right)\right]df_x df_y \tag{1.16}$$

comparing Eq. 1.15 and Eq. 1.16 leads us to a formula which describes how the angular spectrum evolves over the course of propagation; that is

$$\begin{aligned} A(f_x,f_y;z)=&A(f_x,f_y;0)\operatorname{CIRC}\left(\sqrt{(\lambda f_x)^2+(\lambda f_y)^2}\right) \\ &\exp\left(i\frac{2\pi}{\lambda}\sqrt{1-(\lambda f_x)^2-(\lambda f_y)^2}\right) \end{aligned} \tag{1.17}$$

Therefore, the transfer function of the angular spectrum can be written as

$$H(f_x,f_y)=\begin{cases}\exp\left(i\frac{2\pi z}{\lambda}\sqrt{1-(\lambda f_x)^2-(\lambda f_y)^2}\right) & \sqrt{f_x^2+f_y^2}<\left(\frac{1}{\lambda}\right)\\ 0 & \text{Otherwise.}\end{cases} \tag{1.18}$$

The propagation of the angular spectrum reveals itself as a linear, dispersive spatial filter with a bandwidth restricted to the spatial frequencies which satisfy $\sqrt{f_x^2+f_y^2}<\left(\frac{1}{\lambda}\right)$ in which a frequency dependent phase shift is introduced with the modulus of unity. High spatial frequency components result in a significant phase dispersion while the spatial frequency components close to zero yield less phase dispersion. Nevertheless, for a fixed pair of spatial frequencies, longer propagation distances introduce higher dispersion in the optical system.

In order to simplify the transfer function of the angular spectrum, binomial expansion is employed. Let q be a positive, real valued number and less than one. Therefore, the binomial expansion of the expression $\sqrt{1+q}$ is given by

$$\sqrt{1+q}=1+\frac{1}{2}q-\frac{1}{8}q^2+\cdots \tag{1.19}$$

Direct application of the binomial expansion on the transfer function results the following form of the transfer function

$$\exp\left(i\frac{2\pi z}{\lambda}\sqrt{1-(\lambda f_x)^2-(\lambda f_y)^2}\right) = \exp\left(i\frac{2\pi z}{\lambda}\left(1-\frac{1}{2}(\lambda f_x)^2-\frac{1}{2}(\lambda f_y)^2\right)\right)$$
$$= \exp\left(i\frac{2\pi z}{\lambda}\right)\exp\left(-j\pi z\lambda\left(f_x^2+f_y^2\right)\right) \tag{1.20}$$

which is called Fresnel approximation and the region within which Fresnel approximation is valid, is called Fresnel diffraction region. The first exponential term on the right hand side of the Eq. 1.20 signifies a constant phase shift which is experienced by all the spatial frequency components. The second exponential term, introduces a quadratic frequency-dependent phase shift which differs for various components of the wave traveling along the optical axis. In order to complete the discussion of the Fresnel approximation and Fresnel diffraction region, we will derive the Fresnel integral diffraction. To do so, we first apply inverse Fourier transform to the bandwidth limited transfer function; that is

$$\begin{aligned} h(x,y) &= \mathscr{F}^{-1}\left(\exp\left(i\frac{2\pi z}{\lambda}\right)\exp\left(-i\pi z\lambda\left(f_x^2+f_y^2\right)\right)\right) \\ &= \frac{\exp(ikz)}{i\lambda z}\exp\left(\frac{i\pi}{\lambda z}\left(x^2+y^2\right)\right) \end{aligned} \tag{1.21}$$

Considering the function $h(x,y)$ as the convolution kernel and employing convolution theorem, the Fresnel diffraction integral reads as

$$U(x,y) = \frac{\exp(ikz)}{i\lambda z}\int\int U(\xi,\eta)\exp\left(i\frac{k}{2z}\left[(x-\xi)^2+(y-\eta)^2\right]\right)d\xi d\eta \tag{1.22}$$

in which $U(\xi,\eta)$ is the wavefiled across the (ξ,η) plane located at origin, $z=0$, and $U(x,y)$ is the wavefield across the (x,y) plane located at distance z from the origin.If we factor the exponential term, $\exp\left(\frac{ik}{2z}\left(x^2+y^2\right)\right)$, another form of the Fresnel diffraction integral can be written as

$$\begin{aligned} U(x,y) = \frac{\exp(ikz)}{j\lambda z}\exp\left(\frac{ik}{2z}\left(x^2+y^2\right)\right)\int\int U(\xi,\eta) \\ \exp\left(\frac{ik}{2z}\left(\xi^2+\eta^2\right)\right)\exp\left(-i\frac{2\pi}{\lambda z}\left(x\xi+y\eta\right)\right)d\xi d\eta \end{aligned} \tag{1.23}$$

Although we employ the result of angular spectrum calculation as well as convolution theorem to yield an expression for Fresnel diffraction integral, it worth noting that the most elegant way to prove the Fresnel diffraction integral formula originate from first Rayleigh-Sommerfeld theorem. A close inspection of the quadratic term in the integral suggests that if the following approximation which is called Fraunhofer approximation is valid, the value of quadratic term over the aperture area would be close to one. The Fraunhofer approximation reads as

$$z \gg k\frac{\xi^2+\eta^2}{2} \tag{1.24}$$

the direct application of the Fraunhofer approximation on the Fresnel diffraction integral shows that

$$\begin{aligned} U(x,y) = \frac{\exp(ikz)}{j\lambda z}\exp\left(\frac{ik}{2z}\left(x^2+y^2\right)\right)\int\int U(\xi,\eta) \\ \exp\left(-i\frac{2\pi}{\lambda z}(x\xi+y\eta)\right)d\xi d\eta \end{aligned} \tag{1.25}$$

which states that when the Fraunhofer approximation is valid, the observed wavefiled across the (x, y) plane is simply (aside from the factors preceding the integral) the Fourier transform of the aperture profile.

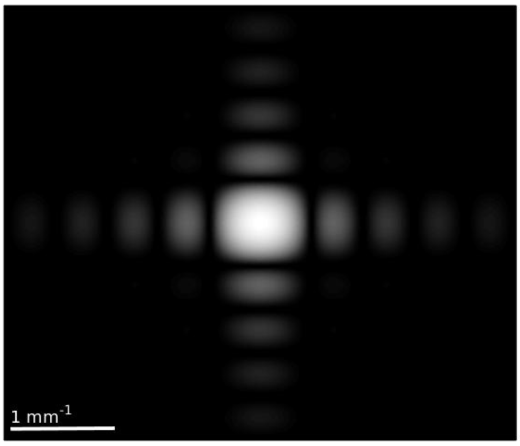

Figure 1.3: Frauenhofer diffraction pattern of a square aperture with side length 1μm.

Fig. 1.3 illustrates the Fraunhofer diffraction pattern of the square aperture. However, it is worth pointing out that, employing the Fraunhofer approximation in order to simplify the Fresnel diffraction integration, has eliminated the shift-invariant property of the Fresnel diffraction which as a result, no transfer function can be related to the Fraunhofer diffraction integral.

Since, We have employed a 4f-lens system to carry out the experimental investigations described in subsequent chapters, our discussion would not be complete if we do not investigate the effect of the lenses on the incoming monochromatic optical wave.

Fig. 1.4 illustrate a lens from front view as well as side view. As shown clearly, Δ_0 denotes the on axis thickness of the lens and $\Delta(x, y)$ signifies the thickness of the lens at different points in the (x, y) coordinate plane. The phase shift induced by the lens on the incoming plane wave is given by

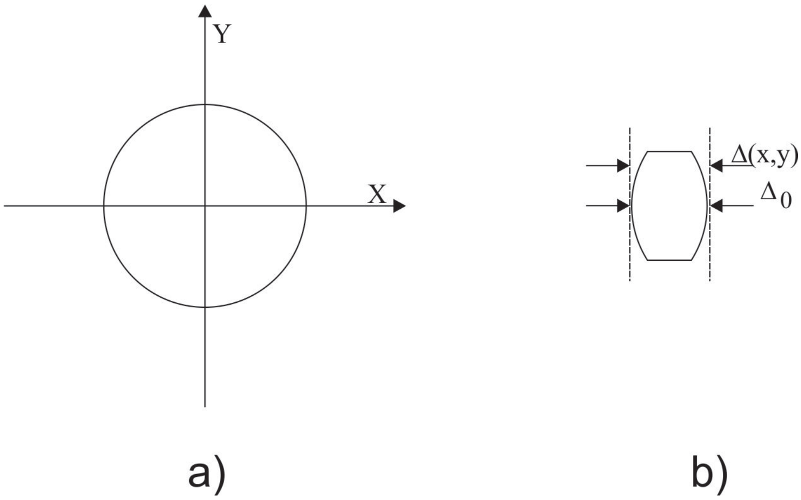

Figure 1.4: A typical lens a) Front view b)Side view.

$$\phi(x,y) = kn\Delta(x,y) + k(\Delta_0 - \Delta(x,y)) \tag{1.26}$$

where n denotes the refractive index of the lens. The first term, $Kn\Delta(x,y)$ signifies the amount of phase shift induced by the lens and the second term, $k(\Delta_0 - \Delta(x,y))$, denotes the a amount of phase shift induced by the remaining free space region bounded by two planes which is indicated by the broken line in Fig. 1.4. However, the phase delay introduced by the lens can more elegantly be represented in the form of multiplicative exponential function; that is

$$t_l(x,y) = \exp(ik\Delta_0)\exp(ik(n-1)\Delta(x,y)) \tag{1.27}$$

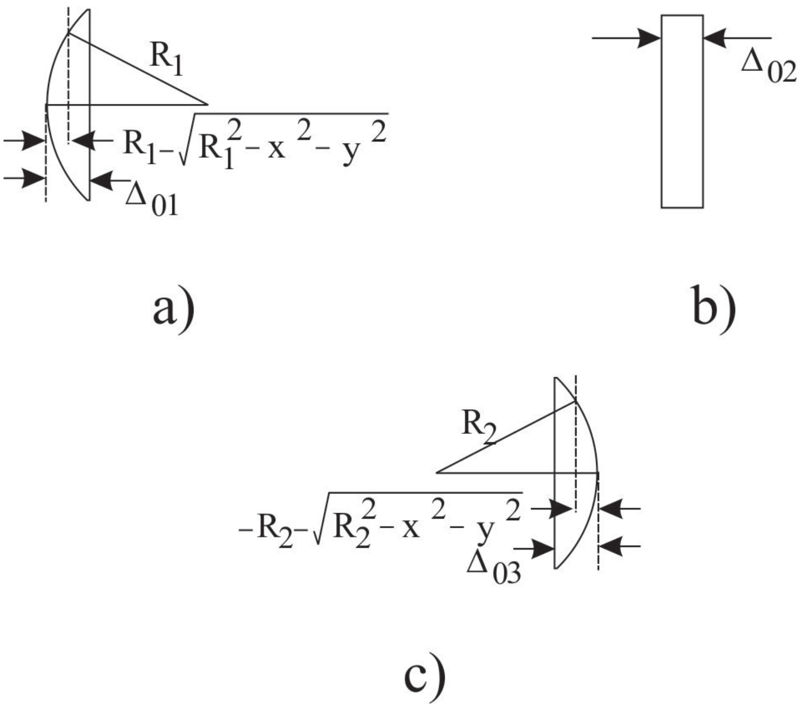

Figure 1.5: Graphical representation of a) Δ_{01} b)Δ_{02} c)Δ_{03} .

It is worth noting that the complex field behind the lens is simply computed by multiplying the complex field in front of the lens by the phase transformation function of the lens which depends tightly on the geometry of the lens. Having defined the lens phase transformation function, the thickness function should be derived. In order to derive a mathematical representation for the thickness of a lens, we divide the lens in to three different parts which are illustrated graphically in Fig. 1.5. The total thickness of the lens is written as

$$\Delta(x,y) = \Delta_1(x,y) + \Delta_2(x,y) + \Delta_3(x,y) \tag{1.28}$$

where the subscripts refer to different part of the lens. Considering Fig. 1.5a, the thickness of the first part of the lens, $\Delta_1(x,y)$ can be written as

$$\begin{aligned}\Delta_1(x,y) &= \Delta_{01} - \left(R_1 - \sqrt{R_1^2 - x^2 - y^2}\right)\\ &= \Delta_{01} - R_1\left(1 - \sqrt{1 - \frac{x^2+y^2}{R_1^2}}\right)\end{aligned} \tag{1.29}$$

where R_1 is factored out of the square root in order to facilitate the analytical calculation. The thickness of the second part of the lens is simply a constant $\Delta_{02}(x,y)$. The thickness of the third component of the lens thickness function reads as

$$\begin{aligned}\Delta_3(x,y) &= \Delta_{03} - \left(R_2 - \sqrt{R_2^2 - x^2 - y^2}\right)\\ &= \Delta_{03} + R_2\left(1 - \sqrt{1 - \frac{x^2+y^2}{R_2^2}}\right)\end{aligned} \tag{1.30}$$

Therefore, the three expression is combined and finally, the thickness function of the lens is seen to be

$$\begin{aligned}\Delta(x,y) = [\Delta_{01} + \Delta_{02} + \Delta_{03}] - R_1\left(1 - \sqrt{1 - \frac{x^2+y^2}{R_1^2}}\right) +\\ R_2\left(1 - \sqrt{1 - \frac{x^2+y^2}{R_2^2}}\right)\end{aligned} \tag{1.31}$$

The lengthy formula for the thickness of the lens can be simplified by the paraxial approximation. In the paraxial approximation, we direct our attention to the portion of the complex wave field which either coincides with or travels close to the lens axis. Hence, for the approximation to be valid, we assume small values of x and y and therefore,

$$\begin{aligned}\sqrt{1 - \frac{x^2+y^2}{R_1^2}} &= 1 - \frac{x^2+y^2}{2R_1^2}\\ \sqrt{1 - \frac{x^2+y^2}{R_2^2}} &= 1 - \frac{x^2+y^2}{2R_2^2}\end{aligned} \tag{1.32}$$

A close inspection of the formulas in Eq. 1.32 mirrors the fact that, by the paraxial approximation in fact we approximate the spherical surface of the lens by the parabolic surface. In other words, the rays which lie either on or close to the optical (lens) axis see a parabolic surface. Therefore, the thickness function of the lens under the light of the paraxial approximation reads as

$$\Delta(x,y) = (\Delta_{01} + \Delta_{02} + \Delta_{03}) - \frac{x^2+y^2}{2}\left(\frac{1}{R_1} - \frac{1}{R_2}\right) \tag{1.33}$$

Having derived the mathematical representation for the thickness variation of the lens, we can then substitute Eq. 1.33 into Eq. 1.27 which results in the following expression

$$t_l(x,y) = \exp(ik\Delta_0)\exp\left(-ik(n-1)\frac{x^2+y^2}{2}\left(\frac{1}{R_1} - \frac{1}{R_2}\right)\right) \tag{1.34}$$

In order to rewrite Eq. 1.34 in a compact form, it is advisable to combine the physical properties of the lens, namely R_1,R_2 as well as n, to a single number called focal length, denoted by f here, which is defined as

$$f \equiv (n-1)\left(\frac{1}{R_1} - \frac{1}{R_2}\right) \tag{1.35}$$

Therefore, substituting focal number into Eq. 1.34 yields

$$t_l(x,y) = \exp\left(-i\frac{k}{2f}\left(x^2+y^2\right)\right) \tag{1.36}$$

which serves as a basis for our future calculation. However, our derivation of the lens transformation function which explains the effect of the lens on the incident wave relies mainly on the paraxial approximation which is restricted to the portion of the wave which lies close to or on the lens axis. Moreover, if the focal length, f, is positive then the emerging spherical wave tends to converge to a point on the axis at the distance f and if the focal length is negative, then the emerging spherical wave behind the lens tends to diverge which results in virtual focal point in front of the lens at the distance f.

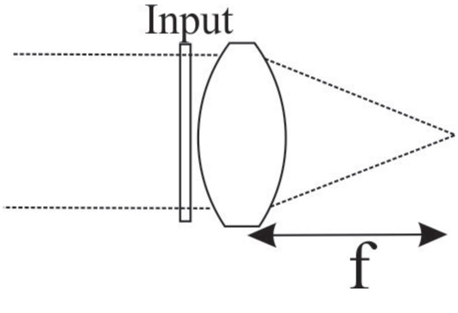

Figure 1.6: The geometry of a transparent input in front of a single positive lens.

Having derived the lens transform function as well as Fresnel diffraction integral, we turn our attention on how these two phenomena are combined together to compute the optical wavefield at the back focal plane of the lens in the presence of a transparent object located immediately in front of the lens, as illustrated graphically in Fig. 1.6. The amplitude transmittance is denoted by $t_A(x,y)$ and the amplitude of the incoming monochromatic is signified by A. Therefore, the amplitude of the incident wave on the lens, denoted by $U(x,y)$ is given by

$$U(x,y) = At_A(x,y) \tag{1.37}$$

The Lens pupil function, $P(x,y)$, is defined to reflect the finite extent of the lens; that is

$$P(x,y) = \begin{cases} 1 & \text{inside the lens aperture} \\ 0 & \text{Otherwise.} \end{cases} \tag{1.38}$$

therefore, the amplitude of the disturbance immediately behind the lens using the lens transform function, Eq. 1.36, can be written as

$$U_l'(x,y) = U_l(x,y)\,P(x,y)\exp\left(-i\frac{k}{2f}\left(x^2+y^2\right)\right) \tag{1.39}$$

To find the amplitude distribution at the back focal plane, $U_f(u,v)$, we employ the Fresnel diffraction integral, namely Eq. 1.23 and replace z with f. Therefore the amplitude of disturbance reads as

$$\begin{aligned} U_f(x,y) = \frac{1}{i\lambda f}\exp\left(\frac{ik}{2f}\left(u^2+v^2\right)\right)\int\int U_l'(x,y) \\ \exp\left(\frac{ik}{2z}\left(x^2+y^2\right)\right)\exp\left(-i\frac{2\pi}{\lambda f}(xu+yv)\right)dxdy \end{aligned} \tag{1.40}$$

where a constant phase delay is dropped. Substituting Eq. 1.39 into Eq. 1.40 yields

$$\begin{aligned} U_f(x,y) = \frac{1}{j\lambda f}\exp\left(\frac{jk}{2f}\left(u^2+v^2\right)\right)\int\int U_l(x,y)\,P(x,y) \\ \exp\left(-i\frac{2\pi}{\lambda f}(xu+yv)\right)dxdy \end{aligned} \tag{1.41}$$

Thus the amplitude of disturbance at the back focal plane is proportional to the Fourier transform of the limited portion of the incoming wave by the aperture. However, the factor of $P(x,y)$ can be ignored if we assume that the diameter of the incoming wave is smaller than the aperture. Therefore, we have

$$U_f(x,y) = \frac{1}{i\lambda f}\exp\left(\frac{ik}{2f}\left(u^2+v^2\right)\right)\int\int U_l(x,y)\exp\left(-i\frac{2\pi}{\lambda f}(xu+yv)\right)dxdy \tag{1.42}$$

Although the distance criteria of the Frauenhofer diffraction is not fulfilled, it is of great importance to notice that the complex amplitude distribution of the field at the back focal plane is just the Fraunhofer diffraction pattern of the incident wave on the lens and it is determined by the input Fourier transform evaluated at $f_x = \frac{u}{\lambda f}$ and $f_y = \frac{v}{\lambda f}$

1.7 Elements of Multigrid

Existing classes of numerical solution techniques for sparse systems of linear equations stemming from boundary value partial differential equations can be categorized in two groups: direct methods and iterative methods. It is worth noting that this sub-section is based on [2].

Direct methods, of which Gaussian elimination is an example, seek the exact solution of a linear system of equations via a limited number of arithmetic operations. Much of the algorithms are not only fast due to being based on the fast Fourier transform algorithm but also, computationally inexpensive compare to iterative algorithms. However, this class of numerical methods are rather specialized and limited to a linear system of equations stemming from self-adjoint boundary value problems.

In contrast to the direct methods, iterative algorithms begin from an initial guess and then, aim to converge (ideally) to an exact solution. To do this, the current approximation is improved through a sequence of iterative steps. In comparison to most of the direct algorithms, the latter group of algorithms have broader range of application and are easier to implement. However, iterative algorithms suffer from smooth error which increase the convergence rate. Multigrid algorithms were developed to overcome these obstacles.

The main idea behind the multigird algorithm stems from the fact that, low frequency components of the error vector appear to be high frequency on the coarse grid and high frequency components of the error vector disappear on the early few iterations. To explain the algorithm, we assume that a partial differential equation is represented by

$$\mathbf{A}u = f \tag{1.43}$$

where $\mathbf{A}$ denotes a tridiagonal, positive definite and symmetric matrix and u is the exact solution. Moreover, f denotes the source term. If v is an approximation to the exact solution and the residual $r = f - \mathbf{A}v$ then, the residual equation is given by

$$r = \mathbf{A}e \tag{1.44}$$

where e denotes the error defined by $e = u - v$. The residual relationship states that e satisfies the same set of equations as the unknown solution u if f is replaced by the residual r. This equation is of great importance owing to the fact that it assists to correct the approximate solution.

A linear interpolation operator is employed on a coarse grid to produce the correspondence vector on a fine grid. For example, for the case of 1-D, the interval $\{t : 0 \leq t \leq 1\}$ is partitioned on p subintervals with the distance h, where $h = \frac{1}{p}$, results in grid points $t_j = jh$ on the domain Ω^h.Therefore, the linear interpolation operator denoted by I_{2h}^h according to $I_{2p}^h v^{2h} = v^h$ is defined as

$$\begin{aligned} v_{2j}^h =& v_j^{2h} \\ v_{2j+1}^h =& \frac{1}{2}\left(v_j^{2h} + v_{j+1}^{2h}\right), 0 \leq j \leq \frac{p}{2} - 1 \end{aligned} \tag{1.45}$$

which says for the even grid points the value on the fine grid is the same as the one on the coarse grid, however, for the odd grid points the value on the fine grid is the average of its neighbor values. This is shown graphically in Fig. 1.7.

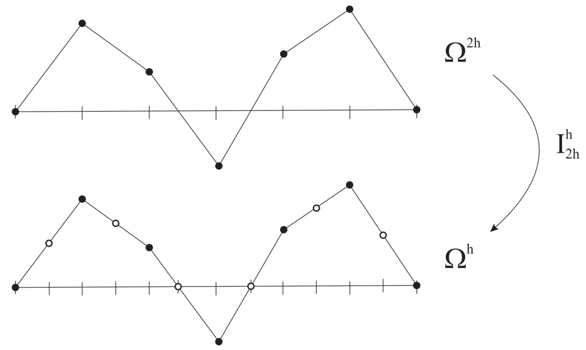

Figure 1.7: Interpolation from coarse grid to a fine grid

In contrast to the linear interpolation operator which moves a vector from a coarse grid to a fine one, restriction operators, of which injection operator is utilized here donated by I_h^{2h}, are employed to transfer the values from the fine grid to a coarse grid. The injection operator is defined as

$$v_j^{2h} = v_{2j}^{h} \tag{1.46}$$

which simply states that the values on the coarse grid are the values of the even grid points of the fine grid. This is demonstrated graphically in Fig. 1.8.

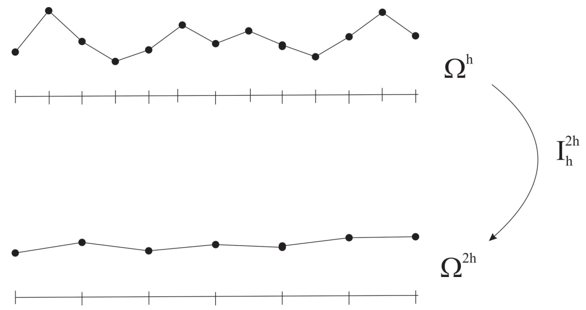

Figure 1.8: Restriction of a fine grid to a coarse grid

Having defined the interpolation operator as well as restriction operator and residual equation, the $V-cycle$ multigrid algorithm may be written for grid spacing $h, 2h, 4h, ..., Lh$ where $L = 2^{l-1}$ and l is the grid points, as :

- Iterate on $\mathbf{A}^h u^h = f^h$ $\lambda 1$ times with initial guess v^h.
- Compute $r^{2h} = I_h^{2h} r^h$.
- Iterate on $\mathbf{A}^{2h} e^{2h} = r^{2h}$ $\lambda 1$ times with initial guess $e^{2h} = 0$.
- Compute $r^{4h} = I_{2h}^{4h} r^{2h}$.
- Iterate on $\mathbf{A}^{4h} e^{4h} = r^{4h}$ $\lambda 1$ times with initial guess $e^{4h} = 0$.
- Compute $r^{8h} = I_{4h}^{8h} r^{4h}$.

  $\vdots$

- solve $\mathbf{A}^{Lh}u^{Lh} = f^{Lh}$.

  $\vdots$

- Correct $e^{4h} \leftarrow e^{4h} + I_{8h}^{4h}e^{8h}$.
- Iterate on $\mathbf{A}^{4h}e^{4h} = r^{4h}$ $\lambda 2$ with the initial guess e^{4h}.
- Correct $e^{2h} \leftarrow e^{2h} + I_{4h}^{2h}e^{4h}$.
- Iterate on $\mathbf{A}^{2h}e^{2h} = r^{2h}$ $\lambda 2$ with the initial guess e^{2h}.
- Correct $v^{h} \leftarrow v^{h} + I_{2h}^{h}v^{2h}$.
- Iterate on $\mathbf{A}^{h}v^{h} = f^{h}$ $\lambda 2$ with the initial guess v^{h}.

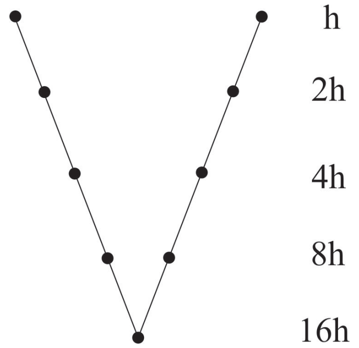

Figure 1.9: Graphical representation of *V-cycle* algorithm

Fig. 1.9 graphically illustrate the order of grids in which they are seen. Owing to its V-shape pattern, the algorithm is called the $V - cycle$. Bearing in mind that nested iteration algorithm suggested that to produce an improved initial guess, coarse grid solution should be obtained as well as the V-cycle algorithm, one can combine both of the algorithms which results in a *Full multigrid algorithm (FMG)*. Although FMG algorithm is more expensive than its V-cycle counterpart, the rate of convergence is faster. Fig. 1.10 demonstrates the FMG pattern graphically .

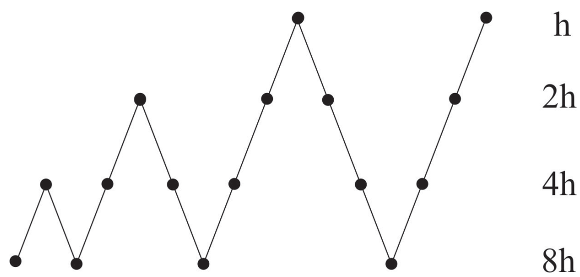

Figure 1.10: Graphical representation of a *FMG* algorithm

1.8 Derivation of TIE

We assume a scalar electromagnetic wave traveling along the optical axis, namely, z axis, in the following form:

$$\psi\left(\vec{r}_{\perp}, z\right) = A\left(\vec{r}_{\perp}, z\right) \exp\left(ikz\right) \tag{1.47}$$

where $\vec{r}_{\perp}$ denotes the plane perpendicular to optical axis direction and $k = \frac{2\pi}{\lambda}$ is the wavenumber of the assumed electromagnetic wave. The Helmholtz equation in three dimensional Cartesian coordinates for the propagation of a wave in free space is given by

$$\left(\nabla^2 + k^2\right) \psi\left(\vec{r}_{\perp}, z\right) = 0 \tag{1.48}$$

where ∇^2 is the three-dimensional Laplace operator. Assuming that the complex envelope $A\left(\vec{r}_{\perp}, z\right)$ changes slowly with respect to z within a wavelength distance signifies that $\frac{\partial^2 A}{\partial z^2} << k^2 A$. Bearing in mind the slowly varying approximation as well as substituting the right hand side of equation 1.47 into the equation 1.48 leads to the following equation which is often called paraxial Helmholtz equation:

$$\left(\nabla_{\perp}^2 + 2ik\frac{\partial}{\partial z}\right) \left[A\left(\vec{r}_{\perp}, z\right) \exp\left(ikz\right)\right] = 0 \tag{1.49}$$

The complex envelope of electromagnetic wave in 1.47 may be defined in terms of intensity I and phase φ as

$$A\left(\vec{r}_{\perp}, z\right) = \sqrt{I\left(\vec{r}_{\perp}, z\right)} \exp\left(i\varphi\left(\vec{r}_{\perp}, z\right)\right) \tag{1.50}$$

In order to derive the TIE, first we derive the required terms separately

$$\begin{aligned}
\frac{\partial^2 A}{\partial x^2} =& \frac{1}{2} \times \frac{\partial^2 I}{\partial x^2} \times I^{\frac{-1}{2}} \times \exp\left(i\varphi\right) \\
&+ \frac{1}{2} \times \frac{\partial I}{\partial x} \times \frac{\partial I}{\partial x} \times I^{\frac{-3}{2}} \times \exp\left(i\varphi\right) \\
&+ \frac{1}{2} \times \frac{\partial I}{\partial x} \times I^{\frac{-1}{2}} \times 1i \times \frac{\partial \varphi}{\partial x} \times \exp\left(i\varphi\right) \\
&+ 1i \times \frac{\partial^2 \varphi}{\partial x^2} \times \exp\left(i\varphi\right) \times I^{\frac{1}{2}} \\
&+ 1i \times \frac{\partial \varphi}{\partial x} \times 1i \times \frac{\partial \varphi}{\partial x} \times \exp\left(i\varphi\right) \times I^{\frac{1}{2}} \\
&+ 1i \times \frac{\partial \varphi}{\partial x} \times \exp\left(i\varphi\right) \times \frac{1}{2} \times \frac{\partial I}{\partial x} \times I^{\frac{-1}{2}}
\end{aligned} \tag{1.51}$$

$$
\begin{aligned}
\frac{\partial^2 A}{\partial y^2} =& \frac{1}{2} \times \frac{\partial^2 I}{\partial y^2} \times I^{\frac{-1}{2}} \times \exp(i\varphi) \\
&+ \frac{1}{2} \times \frac{\partial I}{\partial y} \times \frac{\partial I}{\partial y} \times I^{\frac{-3}{2}} \times \exp(i\varphi) \\
&+ \frac{1}{2} \times \frac{\partial I}{\partial y} \times I^{\frac{-1}{2}} \times 1i \times \frac{\partial \varphi}{\partial y} \times \exp(i\varphi) \\
&+ 1i \times \frac{\partial^2 \varphi}{\partial y^2} \times \exp(i\varphi) \times I^{\frac{1}{2}} \\
&+ 1i \times \frac{\partial \varphi}{\partial y} \times 1i \times \frac{\partial \varphi}{\partial y} \times \exp(i\varphi) \times I^{\frac{1}{2}} \\
&+ 1i \times \frac{\partial \varphi}{\partial y} \times \exp(i\varphi) \times \frac{1}{2} \times \frac{\partial I}{\partial y} \times I^{\frac{-1}{2}}
\end{aligned}
\tag{1.52}
$$

$$
\begin{aligned}
2ik\frac{\partial A}{\partial z} =& ik \times \frac{\partial I}{\partial z} \times I^{\frac{-1}{2}} \times \exp(i\varphi) \\
&- 2 \times \frac{\partial \varphi}{\partial z} \times I^{\frac{1}{2}} \times \exp(i\varphi)
\end{aligned}
\tag{1.53}
$$

Having derived the necessary terms, we substitute the $A(\vec{r}_\perp, z)$ from 1.50 into the left hand side of 1.49, considering just imaginary part on either sides lead us to the so called TIE

$$
\vec{\nabla}_\perp \cdot \left[I(\vec{r}_\perp, z) \vec{\nabla}_\perp \varphi(\vec{r}_\perp, z) \right] = -k\frac{\partial I(\vec{r}_\perp, z)}{\partial z} \tag{1.54}
$$

TIE which is first proposed by Teague [12] is a second order, non-separable and elliptical partial differential equation which relates the intensity variation along the optical axis to the Laplacian of the phase. For strictly positive intensity measurement in the principle plane, the TIE yields a unique solution up to an additive constant where an appropriate boundary condition is defined. However, the zeros in the measurement plane results in the discontinuity in the phase plane in which a unique information can not be retrieved.

1.9 TVAL3

As suggested by the name, TVAL3 was constructed to solve total variation (TV) regularized compressed sensing problems by the augmented Lagrangian algorithm as well as non monotone line search scheme in which the Barzilai-Borwein step [105] is employed to accelerate the rate of convergence.

In order to elucidate the TVAL3 scheme, we assume the following compress sensing problem with TV regularization, that is

$$
min \quad TV(u) \equiv \sum_i \|D_i u\|, s.t. \quad Au = b, \tag{1.55}
$$

where D_i is the discrete gradient matrix at the pixel i as well as A denotes a linear measurement matrix applied to u which results an observation matrix denoted by

b. In other words, the solution to Eq. 4.3 features the lowest discontinuity among other solutions in the solution space.

Variable splitting is then employed to rewrite Eq. 4.3 in the following form

$$min_{w_i,u} \sum_i \|w_i\|, s.t. \quad Au = b \quad \text{and} \quad D_i u = w_i, \quad \text{for all pixels } i. \tag{1.56}$$

The augmented Lagrangian of the expression1.56 denoted by $\mathscr{L}_A$ can be written as

$$\begin{aligned} \mathscr{L}_A\left(w_i, u\right) = \sum_i \left(\|w_i\| - \nu_i^T \left(D_i u - w_i\right) + \frac{\beta_i}{2} \|D_i u - w_i\|^2 \right) \\ - \lambda^T \left(Au - b\right) + \frac{\mu}{2} \|Au - b\|^2, \end{aligned} \tag{1.57}$$

where ν as well as λ are the Lagrangian multipliers and β as well as μ are the penalty parameters. It is worthy to note that the augmented Lagrangian differs from the quadratic penalty function due to the presence of the Lagrange multiplier term which restricts the penalty term. This results to alleviate the difficulties raised by the large penalty term such as ill conditioning. On the other hand, owing to the presence of the squared term, the augmented Lagrangian differs from his precursor, namely the classical Lagrangian method. Therefore, the augmented Lagrangian function is a combination of the squared penalty function and classical Lagrangian function which overcomes the corruption of the numerical conditioning [106, 107].

Now we turn our attention to the new sub-problem, namely, minimization of Eq. 1.57. In light of the optimality condition [106, 107], minimizing Eq. 1.57 with respect to w_i at the iteration results in an analytic expression for $w_{i,k+1}$ which is called shrinkage formula; that is [106]

$$w_{i,k+1} = \max\{\|D_i u_k - \frac{\nu_i}{\beta_i}\| - \frac{1}{\beta_i}, 0\} \frac{\left(D_i u_k - \frac{\nu_i}{\beta_i}\right)}{\|D_i u_k - \frac{\nu_i}{\beta_i}\|}. \tag{1.58}$$

Moreover, the gradient of Eq. 1.57 with respect to u denoted by $d_k\left(u\right)$ can be easily computed; that is[106]

$$d_k\left(u\right) = \sum_i \left(\beta_i D_i^T \left(D_i u - w_{i,k+1}\right) - D_i^T \nu_i\right) + \mu A^T \left(Au - b\right) - A^T \lambda \tag{1.59}$$

As it is demonstrated, rather than minimizing the augmented Lagrangian problem directly, we split it into two sub-problem, namely, minimizing Eq. 1.58 as well as Eq. 1.59. An alternating direction scheme is then employed to solve the sub-problems in which the implemented non-monotone line search algorithm ensures the convergence. It worth pointing out that to increase the speed of convergence as well as decreasing the iteration cost, Barzilai-Borwein method is used to select the adjustable step length. Hence, the implemented TVAL3 scheme after variable splitting reads as[106]

Algorithm (General TVAL3)

initialization

While $\|\tilde{\nabla}\mathscr{L}_A\left(u^k, \lambda^k\right)\| > tol$ **Do**

set starting points $w_0^{k+1} = w^k$ *and* $u_0^{k+1} = u^k$ *for the sub-problems*;

Find minimizer w_0^{k+1} *and* u_0^{k+1} *of* $\mathscr{L}_A\left(w, u, \lambda^k; \mu^k\right)$ *using non-monotone alternating direction*;

Update the multiplier and non-decrease the penalty term;

End Do

It is worth mentioning that C.Li compared the performance of TVAL3 with other packages such as l_1-magic [108, 109] and TwIST [54] as well as NESTA[110] for different scenarios [106]. It was demonstrated that TVAL3 outperforms other stat-of-art implementations and reveal his potential to solve the compress sensing problem with TV minimization in an affordable time with high accuracy[106, 111].

1.10 Scope of this work

In chapter two, A finite element based approach is presented to solve the TIE where we know the position of a free area in an image plane. Dirichlet boundary conditions are defined on the perimeter of a polygon which covers partially the free area and furthermore, the Neumann boundary condition is imposed to the perimeter of the image area. Since TIE is a elliptical differential equation, a built-in multigrid solver is employed to accelerate the convergence speed. finally, experimental demonstration shows the superiority of the proposed method to the conventional method such as fast Fourier transform (FFT) as well as the symmetrization method [3, 58].

A gradient flipping algorithm (GFA) is proposed in chapter three. The GFA is constructed upon two column: sparsity and the charge flipping algorithm. The charge flipping algorithm is a simple but yet, effective algorithm which is applied in crystallography for solving the crystallographic phase problem [112]. In the context of the TIE, charge flipping algorithm is applied to the gradient of the phase which leads to a phase with sparse gradient. Experimental demonstration reveals the potential of the GFA for the phase retrieval application [117].

In chapter four, we compare the proposed GFA algorithm with a TV- regularization approach. The TVAL3 package is considered as routine to solve the TV-regularization problem. Different scenarios are considered to highlight the limitation, weakness and strength of each approach such as a partially piece-wise constant object and piece-wise linear objects [132].

The astigmatic intensity equation (AIE) is presented in chapter five. AIE offers an over determined system of equations to retrieve the phase shift of objects. Moreover, unlike the TIE, the measurements are obtained by rotating a cylindrical lens which helps to lessen the systematic error. An iterative algorithm is suggested and simulated measurements are employed to verify the algorithm. A comparison with the TIE shows that the AIE outperforms the TIE in low frequency information reconstruction.

An overview of the different approaches presented in this work as well as potential future work is presented in chapter six.

Chapter 2

A Finite Element based approach

2.1 Overview

The transport of intensity equation (TIE) provides a very straight forward way to computationally reconstruct wavefronts from measurements of the intensity and the derivative of this intensity along the optical axis of the system. However, solving the TIE requires knowledge of boundary conditions which cannot easily be obtained experimentally. The solution one obtains is therefore not guaranteed to be accurate. In addition, noise and systematic measurement errors can very easily lead to low-frequency artefacts.

In this chapter, a new combination of flux-preserving and Dirichlet boundary condition based on prior knowledge of regions of constant phase in the image plane is introduced (e.g. a region not covered by the object, or a hole in the object). The advantage of the proposed combination of boundary conditions lies in the ability to reconstruct wave fronts also in case we cannot make any reasonable assumption of the boundary conditions on the outer edge of the field of view (e.g. where the assumption of periodic BCs is not justified). Comsol, a finite-element based software, is employed to impose the above-mentioned boundary condition and furthermore, the reconstructed phase by proposed method is compared with that of retrieved by FFT approach as well as symmetrization method [3].

It should be noted that some of the material of this chapter are directly taken from the manuscript [58] of which I am the first author.

2.2 Fourier Transform solution of TIE

An approximate solution of the TIE proposed by Teague [12] is based on the Helmholtz's decomposition theorem in which the vector field $I(\vec{r}_\perp, z)\,\vec{\nabla}_\perp \varphi(\vec{r}_\perp, z)$ can be decomposed as

$$I(\vec{r}_\perp, z)\,\vec{\nabla}_\perp \varphi(\vec{r}_\perp, z) = \vec{\nabla}_\perp \cdot \Phi(\vec{r}_\perp, z) + \vec{\nabla}_\perp \times \Psi(\vec{r}_\perp, z) \tag{2.1}$$

where $\Phi(\vec{r}_\perp, z)$ is a continuous scalar field and $\Psi(\vec{r}_\perp, z)$ is a vector potential. Considering equation 1.54 as well as assuming that the traveling electromagnetic wave is divergence free, one gets

$$\vec{\nabla}_\perp^2 \Phi(\vec{r}_\perp, z) = -k \frac{\partial I(\vec{r}_\perp, z)}{\partial z} \tag{2.2}$$

which is a Poission type auxiliary function. Although Teague suggested to apply the Green function theorem to equation 2.2, we will utilize the Fourier transform(FT) approach denoted by $\mathscr{F}$ to determine the phase which was first proposed by [42].

The derivative identity in the Fourier space can be written as

$$\nabla_\perp f(x,y) = i\hat{\mathbf{x}}\mathscr{F}^{-1}q_x\mathscr{F}[f(x,y)] + i\hat{\mathbf{y}}\mathscr{F}^{-1}q_y\mathscr{F}[f(x,y)] \tag{2.3}$$

where q_x and q_y denote the variable conjugate to x and y in Fourier space respectively and $\hat{\mathbf{x}}$ and $\hat{\mathbf{y}}$ are the unit vectors along the x and y direction. It follows from equation 2.3

$$\begin{aligned}\nabla_\perp^2 f(x,y) &= -\mathscr{F}^{-1}\left(q_x^2+q_y^2\right)\mathscr{F}[f(x,y)] \\ &\equiv -\mathscr{F}^{-1}q_\perp^2\mathscr{F}[f(r_\perp)]\end{aligned} \tag{2.4}$$

where $q_\perp$ denotes the magnitude of the variable conjugate to $r_\perp$. Utilizing equation 2.4, the solution of equation 2.2 can be written as

$$\Phi(\vec{r}_\perp,z) = \mathscr{F}^{-1}q_\perp^{-2}\mathscr{F}\left(k\frac{\partial I(\vec{r}_\perp,z)}{\partial z}\right) \tag{2.5}$$

having derived the solution for Φ, one can reconstruct the following quantity from equation 2.1

$$\nabla_\perp^2\varphi(\vec{r}_\perp,z) = \vec{\nabla}_\perp\cdot\left[I^{-1}(\vec{r}_\perp,z)\vec{\nabla}_\perp\Phi(\vec{r}_\perp,z)\right] \tag{2.6}$$

then using equation 2.4, the solution of the TIE for the phase using FT approach is given by

$$\varphi(\vec{r}_\perp,z) = \mathscr{F}^{-1}q_\perp^{-2}\mathscr{F}\left[I^{-1}(\vec{r}_\perp,z)\vec{\nabla}_\perp\Phi(\vec{r}_\perp,z)\right] \tag{2.7}$$

It worth noting that an implicit periodic boundary condition is assumed in the above derivation. Later, we will show for the case of an object with non-periodic boundary condition, the FT-phase retrieval approach suffers from low frequency artifacts. Besides, owing to the fact that $q_\perp^{-2}$ tends to infinity for very low special frequency indicates that low special frequencies can not be fully recovered. However, in order to compensate for the point close to zero, a cut-off parameter is defined. The points in the principle plane with the value lower than cut-off value will be replaced by cut-off value in the equation 2.7.

2.3 A Finite element based approach

The starting point of our discussion is the Poynting theorem which is given by

$$\nabla.\vec{S} = \frac{\partial W}{\partial t} \tag{2.8}$$

where $\vec{S}$ denotes Poynting vector and W is the amount of energy stored in the medium. Comparing equations 2.8 and 1.54 suggests that the quantity $I(\vec{r}_\perp,z)\vec{\nabla}_\perp\varphi(\vec{r}_\perp,z)$ expresses the intensity flux along the optical direction of propagation or the transverse component of Poynting vector. Therefore, the transverse component of Poynting vector might be written as

$$\vec{S_\perp} = I(\vec{r}_\perp,z)\vec{\nabla}_\perp\varphi(\vec{r}_\perp,z) \tag{2.9}$$

Recall that Green's theorem over the field of view $D(x, y)$ bounded by perimeter P for a vector field F is given by

$$\int\int_D \left(\vec{\nabla}.\vec{F}\right) dD = \oint_P \left(\vec{F}.\hat{n}\right) dP \tag{2.10}$$

where $\hat{n}$ denotes the unit vector normal to the boundaries in the directional plane. Hence, one can derive an equation for the amount of the lost and gained flux by integrating both side of equation 1.54 and then, applying Green's theorem to the left hand side of the equation 1.54 which reads as

$$\begin{aligned}\int\int_D \left(\vec{\nabla}.\vec{S}\right) dD &= \oint_P \left(\vec{S}.\hat{n}\right) dP \\ &= \int\int_D \partial_z I(x, y)\, dD\end{aligned} \tag{2.11}$$

Described already in the work of Tegue [12],conservation of intensity is assumed for the TIE to have a unique solution

$$\oint_P \left(\vec{S}.\hat{n}\right) dP = \int\int_D \partial_z I(x, y)\, dD \tag{2.12}$$

which say that the conservation of intensity is valid if the amount of flux crossing the boundaries is zero.Therefore,

$$\begin{aligned}\oint_P \left(\vec{S}.\hat{n}\right) dP &= 0 \\ \oint_P \left(\left[I(\vec{r}_\perp, z)\, \vec{\nabla}_\perp \varphi(\vec{r}_\perp, z)\right].\hat{n}\right) &= 0 \\ \frac{\partial \varphi}{\partial \hat{n}} &= 0\end{aligned} \tag{2.13}$$

which is the Neumann boundary condition for the phase.

As expressed in the literature review, there are different approaches toward estimation of intensity variation along the optical axis, however, here we employ the simple first order finite difference method. Typically image intensities are detected at the following three planes of focus: $f = -\Delta f, 0, +\Delta f$ where $f = 0$ is the in-focus image and Δf is some fixed defocus step. In practice, when acquiring images under different defocus values intensity is not preserved. Therefore, a straightforward solution to the TIE does not generally exist. In order to overcome mentioned obstacle, we pad the experimental images with the overall mean value of the experimental data by embedding the images into much larger arrays. This kind of padding has been applied by other groups as well [113]. It has been shown that when applying padding in simulated focal series, even iterative algorithms are capable of recovering also very low spatial frequencies of the phase shift, albeit at a prohibitively large number of iterations [114].

We also take advantage of the fact that we can define an area of empty space common to the different images. We define a polygon within this region. The integrated intensity within this polygon can be used for normalizing the data, in case of small variations in the exposure time or illumination flux during the experiment.

The normalized images are then padded with the mean intensity of all three images and since we can assume the phase to be constant in areas of free space, the Dirichlet boundary condition $\varphi = 0$ can be imposed at the edge of the polygon. Imposing this Dirichlet boundary condition leads to a constant phase in this area of free space and also helps to constrain some very low spatial frequency components of the phase.

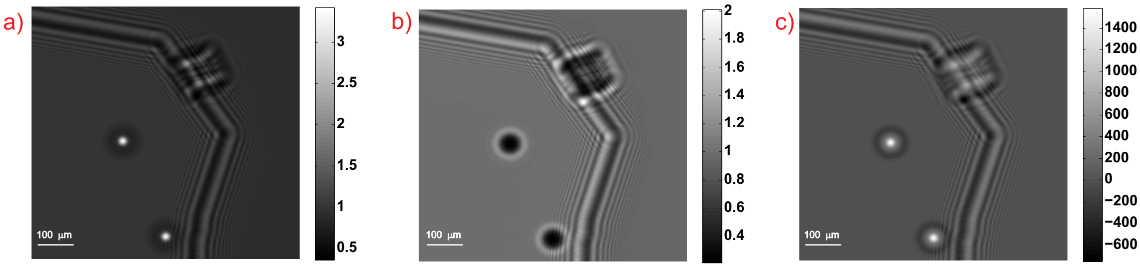

Figure 2.1: Simulated images of a test phase object, a wavelength of $\lambda = 500nm$ a defocus step of $\Delta f = 1$ mm, a pixel size of $dx = 1\mu$m, and a numerical aperture of $NA = 0.3$: a) Over-foused image, b) Under-focused image, c) Intensity variation computed by finite difference method.

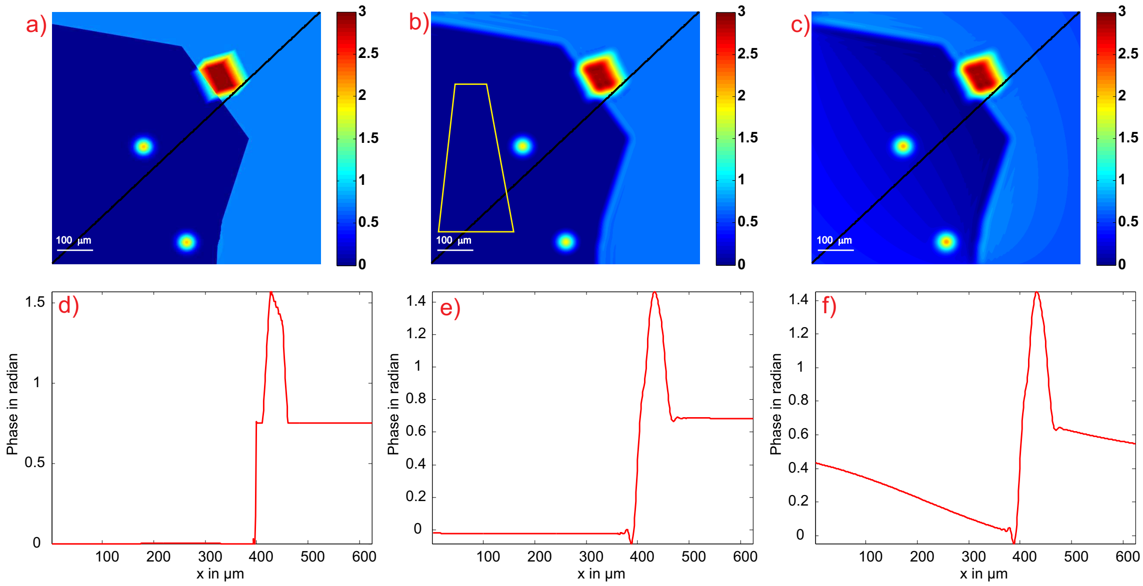

Figure 2.2: a) Original phase, b) Phase reconstructed by the method presented here, c) Phase reconstructed by the FFT method, d) The plot of extracted data along black line in original phase, e) The plot of extracted data along black line in FEM-based approach, f)The plot of extracted data along black line in FFT method.

Figure 2.1 shows an over-focused image, an under-focused image, and the estimation of intensity variation along the optical axis by means of finite difference approach. From the same simulated data, Figure 2.2 compares phase maps reconstructed by different methods. Figure 2.2a shows the original phase.

Figure 2.2c) shows the phase recovered by the Fourier method and our finite element multigrid solution obtained by using the software package COMSOL is shown in Figure 2.2b) in which the above mentioned Dirichlet boundary condition is imposed to the yellow line. The line profile of the original phase shown in Fig. 2.2d), agrees better with that extracted from the FEM-based reconstruction (Fig. 2.2e) than with the line profile extracted from the phase obtained by the conventional FFT method (Fig. 2.2f). Although COMSOL has been applied before to solve the TIE in order to define branch cuts in the phase in the presence of vortices [115], to our knowledge the present work describes the first application of FEM for solving the TIE with the aim to improve the quality of reconstruction of low spatial frequencies in the phase. In order to investigate the performance of the outlined technique in the presence of noise, we added 10 % of Gaussian noise. Figure 4.3 shows the map of reconstructed phase by the FFT and the FEM-based methods in the presence of noise. To highlight the differences, line profiles extracted along the black lines are shown in Figure 4.3b) and Figure 4.3c). Although both plots reveal some gradient in areas where the phase should be constant, the FFT method features much more severe deviations from the original phase used to simulate the input data set. We thus conclude that adding some reasonable prior information may help to yield much more realistic results. The padding applied in both of these reconstruction has increased the image size by a factor of close to 2, i.e. from 624×624 pixels to 1224×1224 pixels. The effect of padding on the FEM-based reconstruction will be discussed in the next section.

2.4 Experiment and reconstruction

Based on a simple optical setup, light optical experiments were conducted in order to investigate the performance of the outlined technique. The wavelength of the collimated incident irradiation was 530 nm and a $4f$ lens system was adopted to acquire images at different planes of focus. The wing of a fly was chosen as a quasi-transparent object, positioned a distance r before the first lens of focal length f, where $f < r < 2f$. An iris aperture is positioned at the back focal plane to limit the range of spatial frequencies of the wave producing the images. A $2k \times 2k$ camera at the focal length of a second lens captures the images with size of 691×691 pixels. Figure 2.4 shows the schematic of the experimental setup.

Estimation of the intensity variation by the finite difference method requires a minimum of two images. Images with different defocus values were captured by translating the camera along the optical axis with a step size of 1 mm. The raw images suffer considerably from artifacts such as Newton rings and dust particles on the lenses. All images were dark-current corrected and normalized by a gain reference image acquired with no object in place. Figures 2.5a) and 2.5b) show the under and over focused gain-referenced experimental images. As pointed out earlier, the $\partial_z I\left(x, y\right)$ - map obtained by the finite difference approach is shown in Figure 2.5c).

We carried out our finite element method (FEM) reconstruction using the Comsol Multiphysics (Comsol Inc.) software package. This software has implemented the

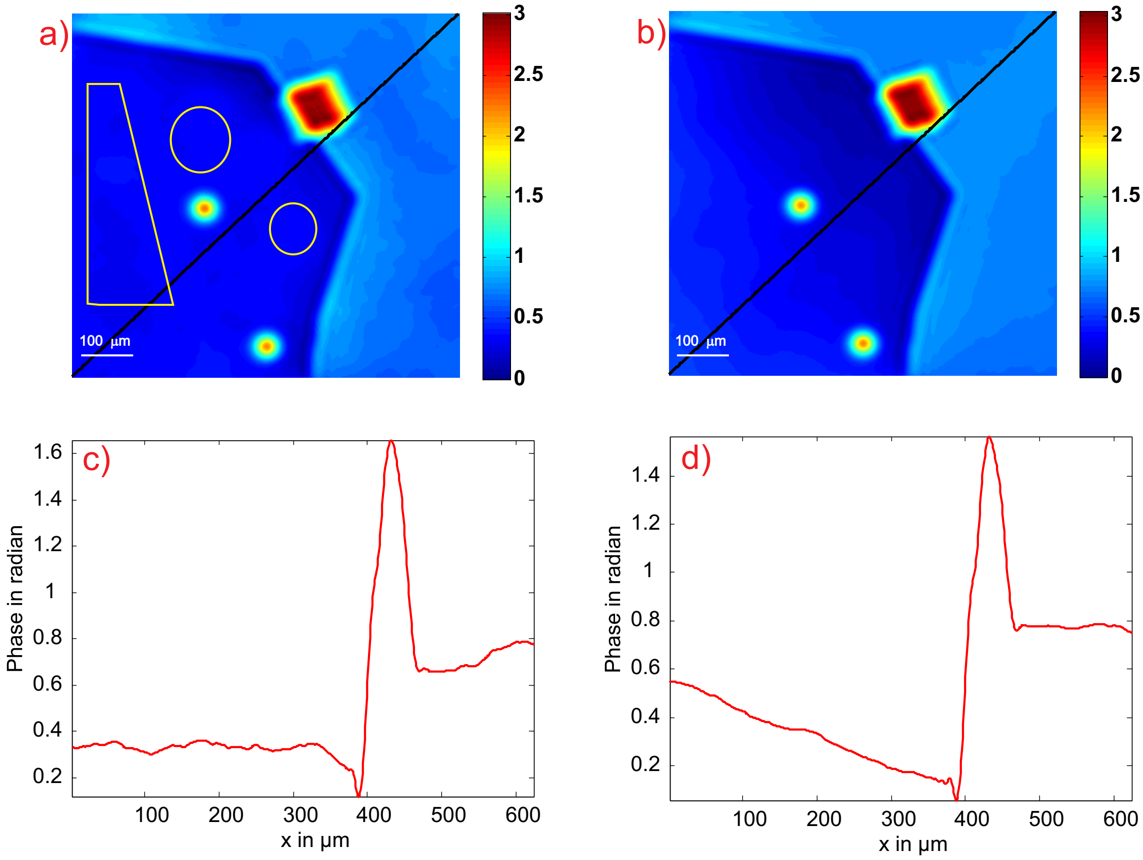

[!ht]

Figure 2.3: a)Phase reconstructed by FEM-based approach,the yellow line shows the outline of the polygon used to identify an area of free space, b) Phase reconstructed by the FFT method, c)The plot of extracted data along black line in FEM-based approach, d) The plot of extracted data along black line in FFT method.

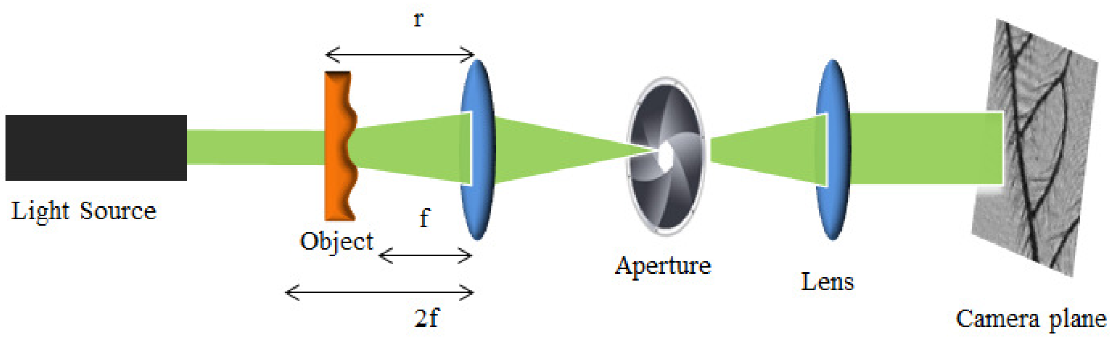

Figure 2.4: schematic of experimental setup.

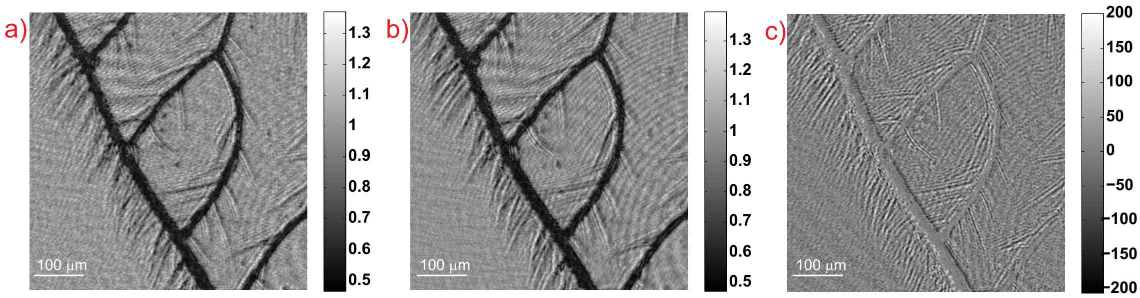

Figure 2.5: Light optical experimental images of a fly's wing: a) Under-focused image b) Over-focused image c) Intensity variation approximated by the finite difference method.

multigrid method as a fast, reliable and powerful method for solving elliptical partial differential equations, The Multigrid method is based on iterating between a fine and a coarse grid, making use of the fact that low frequency errors appear at higher frequencies on the coarse grid. It is worth noting that the Multigrid algorithm has linear complexity in time [116]. In our reconstruction, we took advantage of the full Multigrid scheme as a solver.

To evaluate the effect of padding on both the proposed and conventional (FFT) reconstruction algorithm, the three experimental images (underfocussed, in-focus, and overfocussed) of size 691 × 691 pixels have been padded out to yield image sizes of 891 × 891 and 1291 × 1291 pixels. In addition, we also considered the case of the images without any padding. The reconstructed phases obtained for these different scenarios are shown in Fig. 2.6. The phase maps obtained by the FFT method exhibit stronger low spatial frequency artifacts than the FEM-based reconstructions, however, also the FEM-based approach seems to benefit from an increase in the amount of padding. This fact may become obvious when comparing the region in the reconstructed phase pointed out by the blue arrows.

Since periodic boundary conditions are inherent to the FFT based approach, the FFT solution to the TIE equation may work very well, if the boundary of the image is a uniform support film, but in case of non-periodic objects severe artifacts may arise. Notably, Volkov et al. extensively investigated the FFT approach in connection with a special type of Neumann boundary condition [3]. It was argued there that a new symmetrization of the data would implicitly impose Neumann and periodic boundary conditions. However, mirror padding proposed by Volkov et al. adds again extra information to the data - a procedure that is only justified in rare

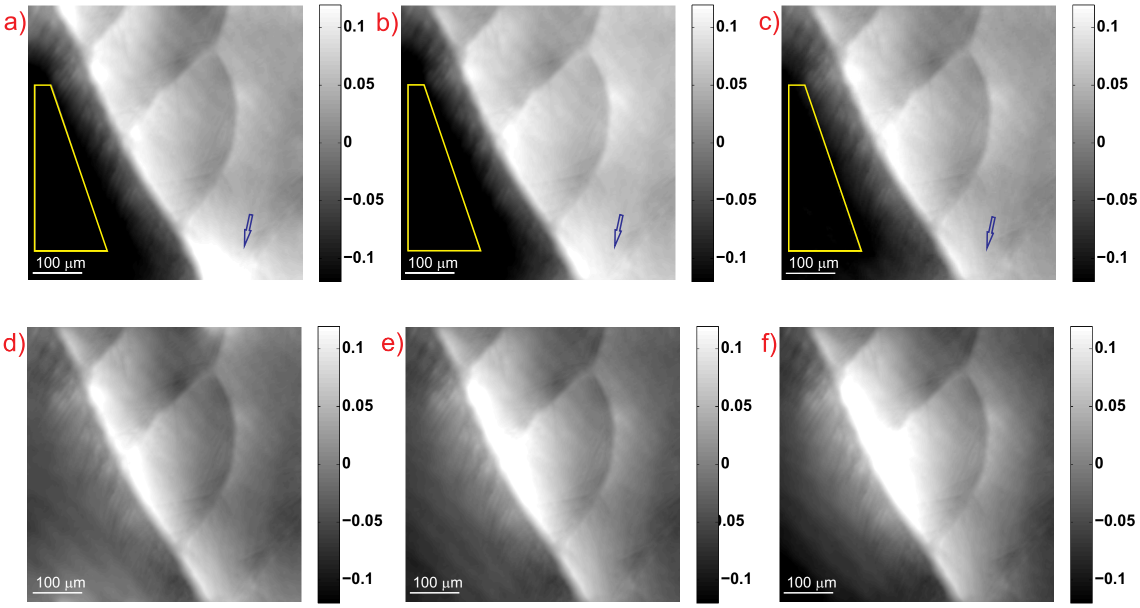

Figure 2.6: Phase maps reconstructed by a) the FEM-based method from the original images of size 691 × 691 pixels, b) the FEM-based method, for images padded to 891 × 891 pixels, c) the FEM-based method, for images padded to 1291 × 1291 pixels, d) the FFT-based method applied to the original images, e) the FFT method, applied images padded to 891 × 891 pixels, f) the FFT method applied to images padded to 1291 × 1291 pixels.

cases. This can be illustrated by looking at the phase map and extracted line profile shown in Figs. 2.7c) and 2.7f): If the phase at the edge does not satisfy the Neuman boundary condition, artefacts are expected to appear. Note that the dynamic range of the phase reconstructed by the mirror padding method (Fig. 2.7c)) is much larger than that of any of the other two reconstructions.

As clearly shown in Figure 2.6, the FFT solution of the TIE suffers effectively from low-frequency artifacts due to imposing periodic boundary conditions. However, the phase retrieved by means of the method proposed in this work is free from these artifacts. Figs. 2.7d) and 2.7e) show line profiles across the FFT and FEM-based phase distribution map, respectively, and Fig. 2.7f) shows the reconstruction obtained by the symmmetrization. These show, that the phase reconstructed by the finite-element based method fluctuates around a constant value in the free space area and is also relatively flat towards the center of the wing, while the FFT-reconstructed phase maps feature severe slopes. We attribute this much more realistic profile of the FEM-reconstructed phase to the Dirichlet boundary condition that was applied to the boundary of the polygon in the free-space region. This greatly helped in recovering low spatial frequency information much more reliably. A successful reconstruction of the hairs at the edge of the wing indicates the capability of this method of retrieving also high frequency information rather well.

2.5 Summary

The TIE is a non-interferometric method for retrieving the phase of wave fronts of optical or matter waves. The TIE has a relatively simple mathematical formulation,

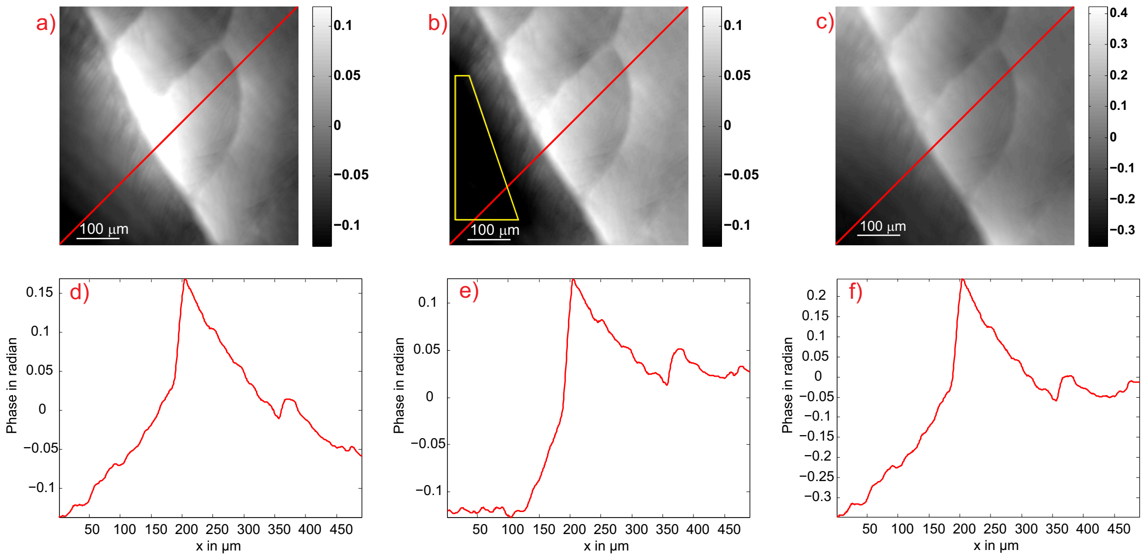

Figure 2.7: a) Phase map reconstructed by the FFT method (with padding), b) Phase map reconstructed by the FEM-based method, c) Phase map reconstructed by the symmetrized solution by Volkov et al. [3] (mirror padding) d), e), and f) Line profiles extracted along the red lines in each of the phase maps shown above. Note that in these line profiles the dynamic range differs between all three different plots.

however; knowledge of the boundary conditions on the phase are necessary to solve it.

In this chapter, I proposed a method for solving the TIE which makes use of prior knowledge of regions of constant phase in the image plane. This is realized by applying Dirichlet boundary condition to the perimeter of a polygon outlining the area of free space. In addition, the experimental data was padded in order to avoid imposing any boundary conditions to the perimeter of the field of view. Neuman boundary conditions were imposed to the boundaries of the padded data. A Multigrid based calculation minimizes the computation time. Application of the proposed approach to a set of simulated and experimental optical data was demonstrated. Comparison of the outlined method with FFT-based approaches as well as symmetrization method reveals the fact that the suggested combination of boundary conditions yields potentially more accurate result.

Chapter 3

Gradient flipping algorithm

3.1 Overview

In this chapter, a new algorithm namely, the gradient flipping algorithm (GFA) based on the charge flipping algorithm as well as the concept of sparsity is introduced. The GFA combines the reciprocal space solution of the TIE with the charge flipping algorithm in order to eliminate the need to explicit boundary conditions. Due to the iterative nature of the algorithm, boundary values are updated in the padded area such that consistency with the experimental measurement is assured.

Different scenarios are assumed to show the potential of the suggested method in boundary value retrieval as well as low frequency information reconstruction. Application of this algorithm to experimental data and comparison with conventionally used algorithms demonstrates an improved retrieval of the low spatial frequencies of the phase.

The material of this chapter is taken directly from the submited manuscript [117] of which I am the first author.

3.2 Introduction

Wavefront sensing, i.e. the detection of relative phase shifts in propagating waves provides essential information in imaging applications where the scattering process affects the phase of the probing wave. Examples which highlight the importance of being able to detect phase shifts of waves passing through transparent objects include imaging of unstained cells under the optical microscope and imaging of soft matter (e.g. DNA, viruses, proteins and other macromolecules, polymers, etc.) in the transmission electron microscope (TEM). In 1953, Frits Zernike received the Nobel Prize in Physics for the development of phase contrast microscopy, a technique which allows part of the phase information carried by a wave to be converted into an amplitude signal, making it detectable as part of the intensity variations in the image. In 1971, Dennis Gabor received the Nobel Prize in Physics for developing the holographic principle [118], a technique by which the phase of a wave could be extracted by post-processing images. Gabor's first holograms were inline holograms recorded in the electron microscope. Later, iterative [119, 120] and deterministic [12, 121–123] mathematical formulations and associated computer algorithms were developed by which both phase and amplitude of a wave could be recovered from intensity measurements at different planes along the optic axis, a so-called focal series.

One very popular approach toward wavefront reconstruction from intensity measurements at different planes of focus is the transport of intensity equation (TIE) [12, 124] which, due to its simple mathematical formulation and straight-forward computational implementation, has attracted much attention in research communities as diverse as cold atom clouds [125], digital optical holography [126] and medical X-ray imaging [98].

Many algorithms such as the fast Fourier transform [122], the finite element method [58, 115], multigrid methods [97], a special symmetrization approach [4], each requiring Neumann, Dirichlet, or periodic boundary conditions have been proposed and applied for solving the TIE.

For wavefront reconstruction from focal series of images, the high spatial frequency components of the phase are well-defined by the data, but the low spatial frequency components are largely determined by the boundary conditions, which are usually unknown. Gureyev et al. [39, 40] and later Zuo et al. [48] introduced hard-edge apertures or, more generally non-uniform illumination during the experiment and thus physically enforced Neumann boundary conditions, allowing orthogonal series expansion based approaches to be used to solve the TIE. Such an approach to make the boundary conditions physically accessible may be feasible in some setups, but not generally. In the TEM, for example, the field of view is often so small that no aperture with perfectly abrupt edges exists, in particular not at atomic resolution.

There have been attempts to improve the recovery of low spatial frequency information in the context of the TIE by reformulating it as a total-variation optimization problem, [52, 127]; however, these approaches require a piecewise constant phase. Other approaches include the application of structured illumination [128]; the experimentally much more complicated interferometric set-up [129]; or prior knowledge of the measurement variation [73]. Therefore the problem of faithfully recovering low spatial frequency components of arbitrarily shaped phases remains, at least for a very large range of applications of wave front sensing.

In this work, we propose a simple iterative algorithm, gradient flipping (GF), with an emphasis on objects that are non-periodic and non-piecewise linear. GF imposes sparsity on the gradient of the phase by either driving a certain percentage of the phase gradient to zero, or forcing all phase gradients below a certain positive threshold to zero. By combining the conventional Fourier method to solve the TIE with principles adapted from the charge flipping algorithm in crystallography, GF determines boundary conditions on the phase, while preserving consistency with the higher frequencies of the experimental data.

In Sec. 3.3 the TIE and its conventional Fourier solution are introduced; Sec. 3.4 details the gradient flipping algorithm; then, in Sec. 3.5 it is demonstrated with simulations that the GF algorithm retrieves the boundaries and low spatial frequencies of two test objects; experimental results on a fly wing are presented in Sec. 3.6; and, finally, conclusions are drawn in Sec. 4.6.

3.3 The transport of intensity equation

The TIE is a second order elliptical, non-separable and inhomogeneous partial differential equation which relates the irradiance as well as the variation of the irradiance along the direction of propagation to a Laplacian-like function of the phase:

$$\vec{\nabla}_{\perp} \cdot \left[I\left(\vec{r}\right) \vec{\nabla}_{\perp} \varphi\left(\vec{r}_{\perp}\right) \right] = -k \frac{\partial I\left(\vec{r}\right)}{\partial z} \tag{3.1}$$

where k denotes the wave number of the incident radiation, and $\vec{r}_{\perp}$ is a vector in the plane normal to the optic axis. $\frac{\partial I(\vec{r})}{\partial z}$ denotes the variation of intensity along the optical axis z. This quantity is most often approximated by the simple first order finite difference approximation

$$\frac{\partial I\left(\vec{r}\right)}{\partial z} \approx \frac{I\left(\vec{r}, +\Delta z\right) - I\left(\vec{r}, -\Delta z\right)}{2\Delta z} \tag{3.2}$$

Here Δz is a small distance along the optic axis. If the image $I(\vec{r})$ is recorded in the exact focus of the imaging system, then $I\left(\vec{r}, +\Delta z\right)$ and $I\left(\vec{r}, -\Delta z\right)$ are images recorded under over-focus and under-focus condition respectively. Note that $I\left(\vec{r}\right)$ has to be non-zero, for this equation to have a well defined solution.

Expression (4.1) can be rewritten in the following form

$$\varphi\left(\vec{r}_{\perp}\right) = -k\nabla^{-2}\vec{\nabla}_{\perp} \cdot \frac{\vec{\nabla}_{\perp}\nabla^{-2}\frac{\partial I(\vec{r})}{\partial z}}{I\left(\vec{r}\right)} \tag{3.3}$$

where $\nabla^{-2} = (\vec{\nabla}_{\perp} \cdot \vec{\nabla}_{\perp})^{-1}$. A detailed discussion on the validity and range of applicability of equation (3.3) can be found in [37].

The nature of this equation implies that boundary conditions must be applied to solve it. Assuming different boundary conditions will yield different solutions for the phase $\varphi\left(\vec{r}_{\perp}\right)$. A number of different algorithms have been developed to solve the TIE (e.g. [4, 14, 39, 70, 72, 113, 122, 130]), many of which are based on the very popular approach by Paganin and Nugent [122] which makes use of the fact that

$$\nabla^{-2} f\left(\vec{r}_{\perp}\right) = \mathcal{F}^{-1}\left\{\left|\vec{q}_{\perp}\right|^{-2} \mathcal{F}\left[f\left(\vec{r}_{\perp}\right)\right]\right\} \tag{3.4}$$

where $\mathcal{F}$ and $\mathcal{F}^{-1}$ are the two-dimensional forward and inverse Fourier transform, respectively, and $\vec{q}_{\perp}$ is the two-dimensional reciprocal space coordinate in the plane of $f\left(\vec{r}_{\perp}\right)$. At $|q_{\perp}| = 0$ this expression diverges, so at that reciprocal space point one can simply multiply by zero instead. This is a physically legitimate procedure, since this defines the mean value of the phase—a physically undefined quantity—as zero.

This expression is straightforward to implement computationally, since it makes the expression (3.3) fully deterministic. However, by using discrete Fourier transforms periodic boundary conditions are implicitly imposed. Also for iterative approaches, such as finite element [58, 115] or multigrid [14] methods the boundary conditions must be specified and are often chosen to either be periodic, or of the Neumann type, or even both [14].

In the context of wavefront sensing the investigated objects often have sparse phase gradients

$$\vec{G}\left(\vec{r}\right) = \vec{\nabla}_{\perp}\varphi\left(\vec{r}\right) = -k\frac{\vec{\nabla}_{\perp}\nabla^{-2}\frac{\partial I(\vec{r})}{\partial z}}{I\left(\vec{r}\right)}. \tag{3.5}$$

This means they contain areas where the phase is rather flat. Examples of such sparse objects include live cells in biological, biochemical, or biophysical applications, a large fraction of objects (e.g. nanoparticles) observed in the TEM, but also objects that extend well beyond the detected field of view, but have regions of constant optical thickness (e.g. the experimental example shown below).

3.4 Gradient flipping

Gradient flipping (GF), is based off the charge flipping (CF) algorithm which was originally developed for X-ray crystallography [112] where it is very effective in finding sparse solutions of the charge density consistent with experimental diffraction data.

GF pads the input data $I(\vec{r})$ with its mean value so that the padded image is twice as large along each of its two dimensions as the original image [131]. Also $\partial I(\vec{r})/\partial z$ is padded to the same size, with zeros around its perimeter. The data in the padded area is then iteratively updated such that the phase gradient within the area corresponding to the measurement either has a certain percentage driven to zero, or has the gradient in all pixels the absolute value of which is below a certain positive threshold minimized.

The GF algorithm iterates between $\vec{G}(\vec{r})$ in Eq. 3.5 and the following expression for $\partial I(\vec{r})/\partial z$:

$$D\left(\vec{G}'\right) = \frac{-\vec{\nabla}\cdot I(\vec{r})\vec{G}'(\vec{r})}{k}, \tag{3.6}$$

where gradient flipping is applied as

$$\vec{G}'\left(\vec{r_\perp}\right) = \begin{cases} \vec{G}\left(\vec{r_\perp}\right) & \text{if } \left\|\vec{G}\left(\vec{r_\perp}\right)\right\|_1 > \delta \\ -\beta\vec{G}\left(\vec{r_\perp}\right) & \text{if } \left\|\vec{G}\left(\vec{r_\perp}\right)\right\|_1 \leq \delta. \end{cases} \tag{3.7}$$

The parameter β is chosen slightly below 1, i.e. $\beta = 0.97$ in order to improve convergence. Furthermore, δ defines a threshold between 5% and 20% of the maximum value of $\|\vec{G}\left(\vec{r_\perp}\right)\|_1$, this proved to keep the balance between perturbation and algorithmic stability as suggested in [112].

At each iteration the left hand side of (3.6) is updated with the experimental data $dI_z^{\text{exp.}}\left(\vec{r_\perp}\right)$ by

$$dI_z\left(\vec{r_\perp}\right) = \begin{cases} D\left(\vec{G}'\right) & \text{if } \vec{r_\perp} \in \text{padded area} \\ \mathcal{F}^{-1}\left[h\mathcal{F}\left(D\left(\vec{G}'\right)\right) + (1-h)\mathcal{F}\left(dI_z^{\text{exp.}}\left(\vec{r_\perp}\right)\right)\right] & \text{if } \vec{r_\perp} \in \text{experimental area}, \end{cases} \tag{3.8}$$

where h is defined in reciprocal space as

$$h\left(\vec{q}_\perp\right) = \exp\left(-R_{LP}^2\left|\vec{q}_\perp\right|^{-2}\right). \tag{3.9}$$

The mask h acts as a Gaussian low-pass filter for the flipped gradient $\vec{G}'(\vec{r})$ with a characteristic length of $2\pi R_{LP}$. This updating rule thus preserves the high spatial frequencies from the measurements, which are generally well-defined by the experiments, and lets the low-frequency information, which is only weakly present in the measurements, be dictated by the gradient flipping.

$dI_z(\vec{r})$ is initialized with the experimental values $dI_z^{\text{exp.}}(\vec{r})$ and zero-padded. Then it is fed into an iterative procedure which loops over the operations defined in expressions (3.3), (3.5), (3.7), and (3.8), feeding the updated $dI_z\left(\vec{r_\perp}\right)$ again into expression (3.3). Convergence is reached when successive estimates of the phase are sufficiently similar. Fig.3.1 shows a flowchart of the proposed algorithm.

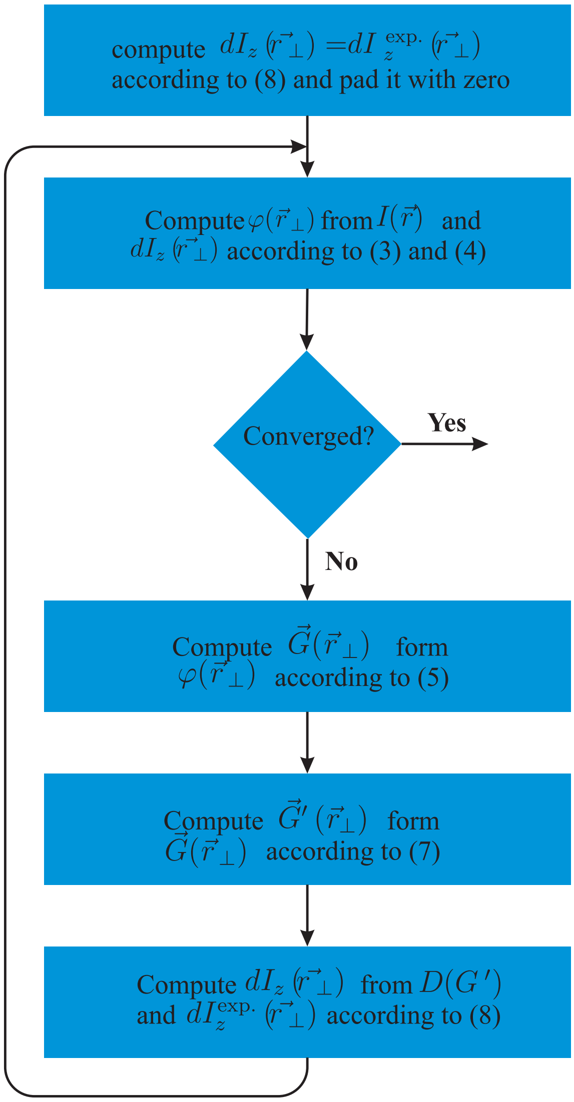

Figure 3.1: The flowchart of the proposed TIE-based algorithm.

3.4.1 Free parameters δ and R_{LP}

A careful selection of the threshold parameter δ is a matter of great importance owing to its role as a trade-off between stabilization and perturbation of the algorithm. The threshold is defined as $\delta = \zeta\sigma$, where σ is the standard deviation of the phase gradient and ζ is a constant. As shown in Fig.3.2, despite the variation of σ during the initial iterations, it remains almost constant throughout the rest of the proposed iterative algorithm. This confirms the eligibility of σ to be a reasonable basis for the optimum choice of δ. Following the suggestion of Oszlányi et al. [112], we chose the value of ζ between 1.0 and 1.2.

The characteristic length scale of the mask h in (3.8), R_{LP}, is the second free parameter in the proposed algorithm and is determined entirely from the experimental data by setting it to the value that minimizes χ^2 in (3.10). The χ^2 figure-of-merit

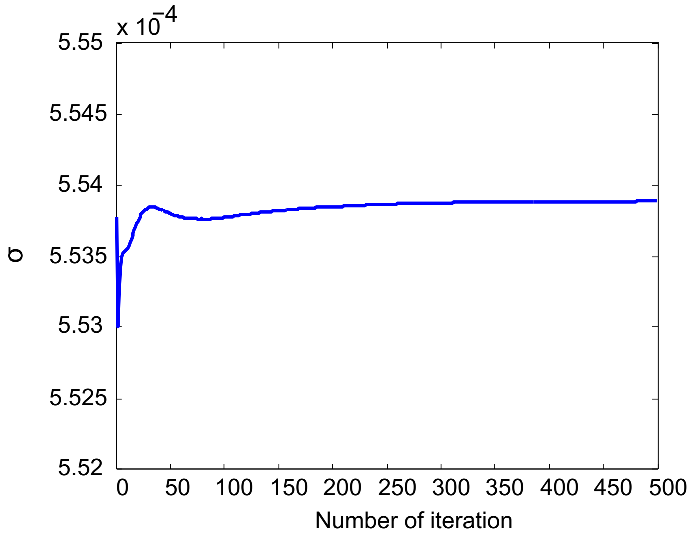

Figure 3.2: Plot of σ as a function of iterations, an almost constant value of σ furnishes a basis for selecting optimum δ.

is defined as,

$$\chi^2 = \frac{\sum_{x,y,z} \left[I^{sim}\left(\vec{r}, z, R_{LP}\right) - I^{exp}\left(\vec{r}, z, \right) \right]^2}{\sum_{x,y,z} I^{exp}\left(\vec{r}, z, \right)} \tag{3.10}$$

where the values of z being summed over are the under- and over-focus at which the experimental images have been recorded, and x and y span the area of those images. Furthermore, $I^{sim}(\vec{r}_\perp, R_{LP})$ are the images simulated from the phase $\varphi(\vec{r}, R_{LP})$ that has been reconstructed with R_{LP} and the amplitude $A(\vec{r}) = \sqrt{I(\vec{r}, z = 0)}$. $I^{exp.}$ denotes the experimental data.

3.5 Simulations

In this section the performance of GF is demonstrated on simulations of two specimens: the projection of a cube and a L-shaped membrane.

3.5.1 Projected cube

Images of a test object are simulated for a wavelength of $\lambda = 500$ nm, a defocus step of $\Delta f = 1$ mm, a numerical aperture of 0.3 and a pixel size of 1 μ m. Fig. 3.3 shows an under focused, and an over focused image, as well as the finite difference estimate of the intensity variation along the optical axis determined from those. The images were padded by a factor close to 2, i.e. from 624×624 to 1200×1200 pixels.

The threshold δ was set to $6.64e^{-4}$, corresponding to a ζ of 1.2. From the graph in Fig. 3.4 it is apparent that χ^2 is minimal for values of R_{LP} greater than 17.77 μ m and R_{LP} is thus set to this value.

Fig. 4.1(b) shows the retrieved phase by means of the proposed approach and Fig.4.1(a) displays the original phase of the wave used to simulate the input data shown in Fig. 3.3. In Fig. 4.1(c) the boundaries of the original phase and its reconstruction are compared.

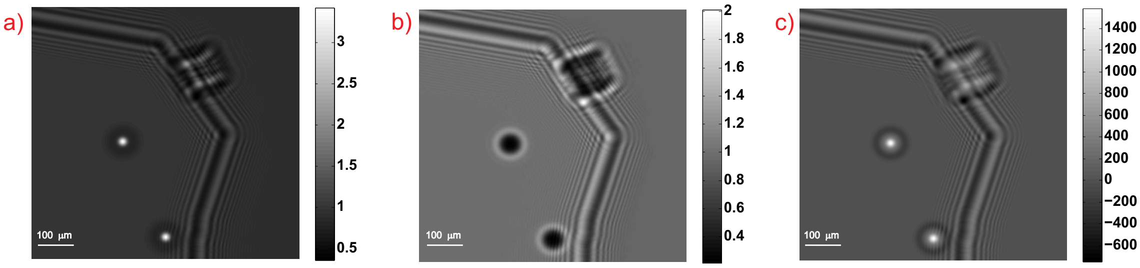

Figure 3.3: a) Under-focused b) Over-focused c) Finite-difference estimate of the intensity variation according (3.2).

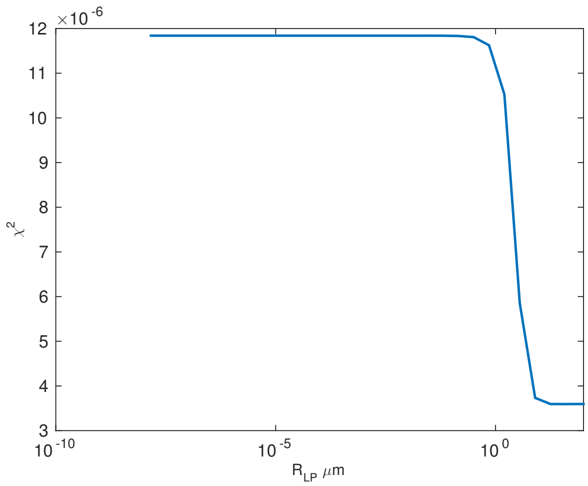

R

Figure 3.4: χ^2 as a function of R_{LP}.

3.5.2 L-shaped membrane

To further investigate the performance of the proposed algorithm for properly recovering also slowly varying phases, we constructed a phase object with the phase given by a continuous function that is not piecewise constant (Fig. 3.6(a)), namely the L-shaped membrane; this function can be obtained by the MATLAB expression `'membrane()'`. Fig. 3.6(c) shows the phase map retrieved by means of the FFT approach, which assumes periodic boundary conditions, while Fig. 3.6(b) shows the reconstruction obtained by the symmetrization method [4]. As clearly shown in Fig. 3.6(d) , the proposed algorithm yields a more accurate reconstruction than the aforementioned approaches. Furthermore, from Fig. 3.6(d) it is clear that GF retrieves the boundaries much better.

For this reconstruction the parameter δ has been set such that the number of pixels being flipped corresponded to one quarter of the total number of the pixels in the field of view. And R_{LP} has chosen to be 34.52μm by minimizing χ^2.

3.6 Experiment

The GF algorithm is tested further using experimental data acquired from the simple optical setup shown in Fig. 3.7. The system is comprised of a laser with integrated collimator emitting green light at a wavelength of λ = 520 nm, two lenses with a focal length of f = 150 mm, an iris diaphragm and a 2048 × 2048 pixel CCD

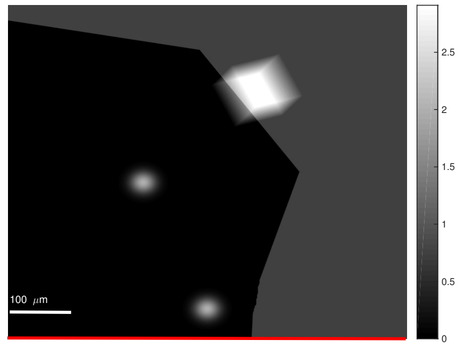

(a)

(b)

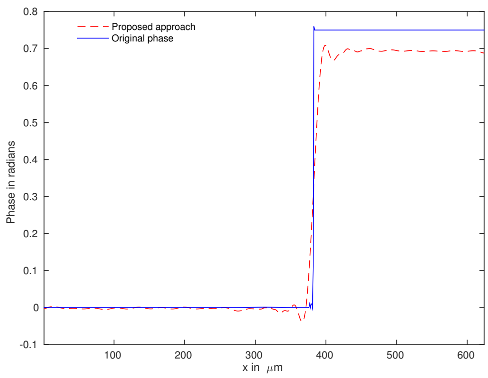

(c)

Figure 3.5: a)Original phase. b) Reconstructed phase by proposed method. c)Line profile extracted along the red line in each of the phase maps.

detector. The wing of a fly was used as a test object positioned at a distance r in front of the first lens, with $f < r < 2f$. The diaphragm was placed at the back focal plane of the first lens in order to limit the numerical aperture of the system to about 0.1. Images at the three focal planes $z = -\Delta z$, $z = 0$, and $z = +\Delta z$ were acquired by translating the camera along the optic axis with a defocus step of $\Delta z = 1$ mm.

All three images were dark-current corrected, and a gain reference image with no object in place was used for normalization. Since a difference in defocus leads to a difference in contrast between these three images and motivated by the fact that

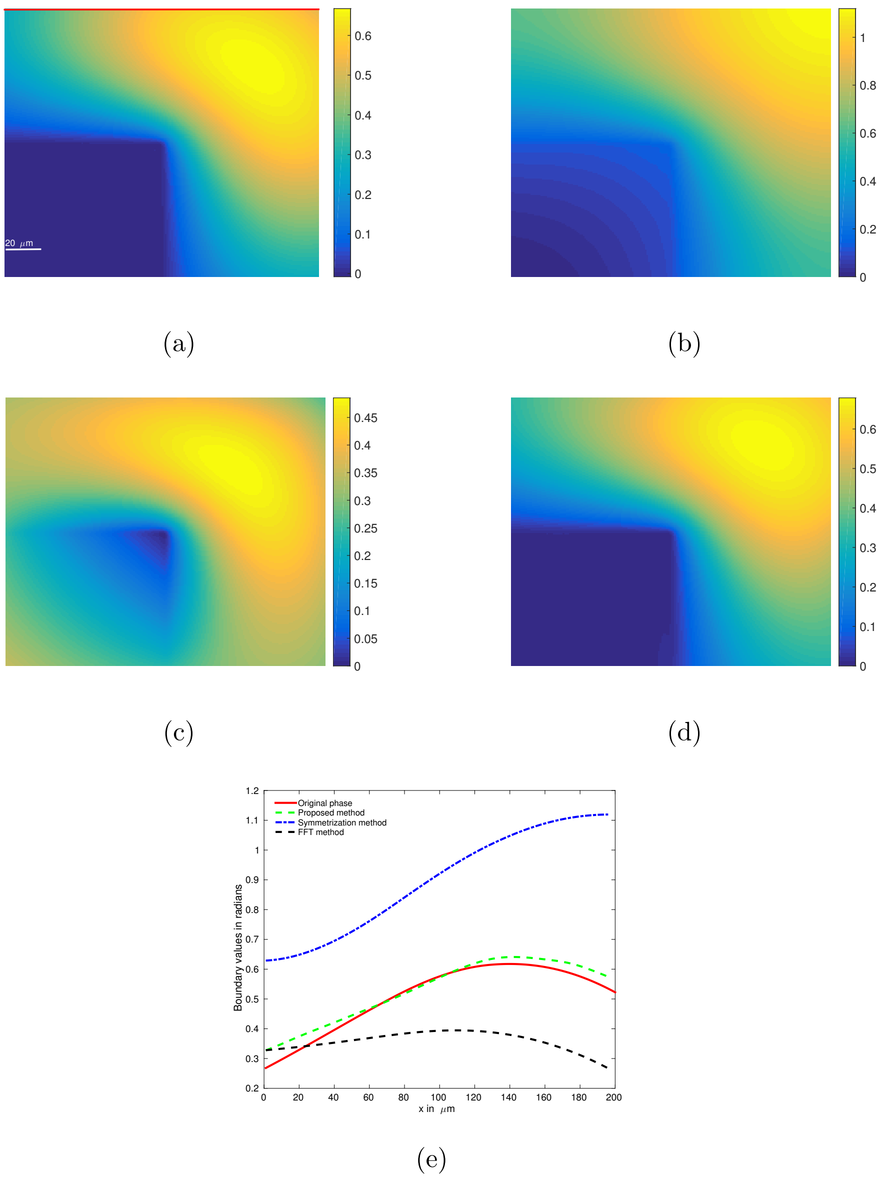

Figure 3.6: Phase reconstructed by means of a)Original phase obtained by the Matlab expression `'membrane()'`, b) the symmetrization method (Neumann boundary conditions), c) the FFT approach (periodic boundary conditions), d)and the approach proposed here. e)Line profile extracted along the red line shown at the top of (a) in each of the phase maps.

$I(\vec{r}, +\Delta z) + I(\vec{r}, -\Delta z) \approx 2I(\vec{r})$ the two defocused images $I(\vec{r}, \pm\Delta z)$ were registered to the focused image $I(\vec{r})$ by iterating the following two steps until convergence:

Step 1: Shift $I(\vec{r}, +\Delta z)$ to the position of the maximum of the cross correlation of that image with $2I(\vec{r}) - I(\vec{r}, -\Delta z)$, and

Step 2: Shift $I(\vec{r}, -\Delta z)$ to the position of the maximum of the cross correlation of that image with $2I(\vec{r}) - I(\vec{r}, +\Delta z)$,

each time using the shifted defocused image from the previous iteration for constructing the new reference.

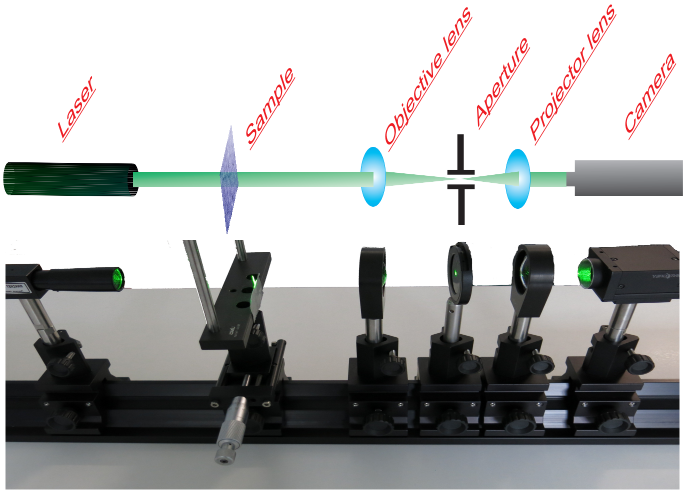

Figure 3.7: Experimental setup: the wing of a fly is imaged by a NA-limiting 4f-system at a magnification of $M \approx 1$. The focal series in Fig. 3.8 was acquired by shifting the detector by ± 1 mm.

The under-focused and over-focused image, as well as $dI_z^{\text{exp.}}(\vec{r_\perp})$ computed according to (3.8) are shown in Fig. 3.8. Setting $\zeta = 1.2$ converged to a δ-value of 5.22×10^{-5}.

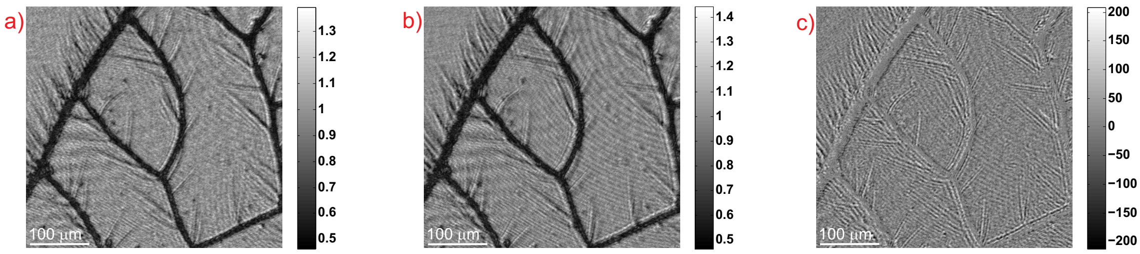

Figure 3.8: a) Under-focused image b) Over-focused image c) Finite difference estimate of the intensity derivative along the optical axis.

Furthermore, the minimum of χ^2 occurs at $R_{LP} = 91.2\ \mu$ m(see Fig. 3.9). The algorithm was iterated for 20 epochs with the above-mentioned parameters.

Fig. 3.10 shows phase maps $\varphi(\vec{r_\perp})$ reconstructed by three different techniques: a) the conventional FFT method applying (3.3) and (3.4), b) the symmetrization mirror padding approach proposed by Volkov et al. [4], and c) the GF scheme proposed here. For both the conventional FFT method (a), as well as the proposed GF algorithm (c) the experimental data were padded as described above to result in data of twice the original image dimensions.

All three phase maps shown in Fig. 3.10 are consistent with the experimental data, but the applied boundary conditions differ. The reconstructed phase maps shown in Figs. 3.10a) and 3.10b) are unphysical, because in both cases the phase shift inside the wing drops below the phase shift in the empty area. The FFT reconstruction shown in Fig. 3.10a) also features a severe overall phase slope in the empty area which cannot be deemed physical. The line profiles across the reconstructed phase maps show good agreement between the three different reconstruction results for fine details, but they also highlight the large differences at low spatial frequencies.

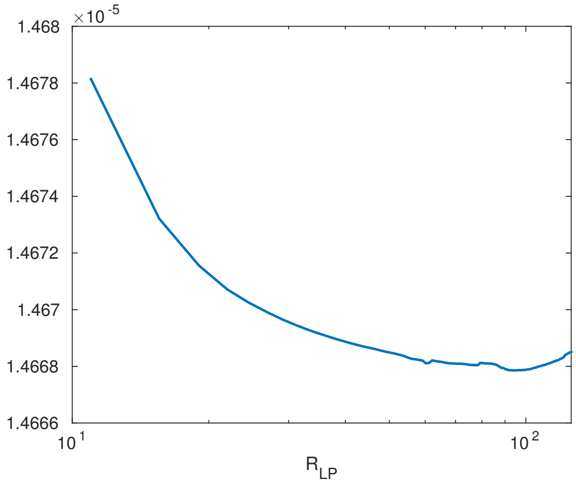

Figure 3.9: Plot of χ^2 as function of R_{LP} (in μm).

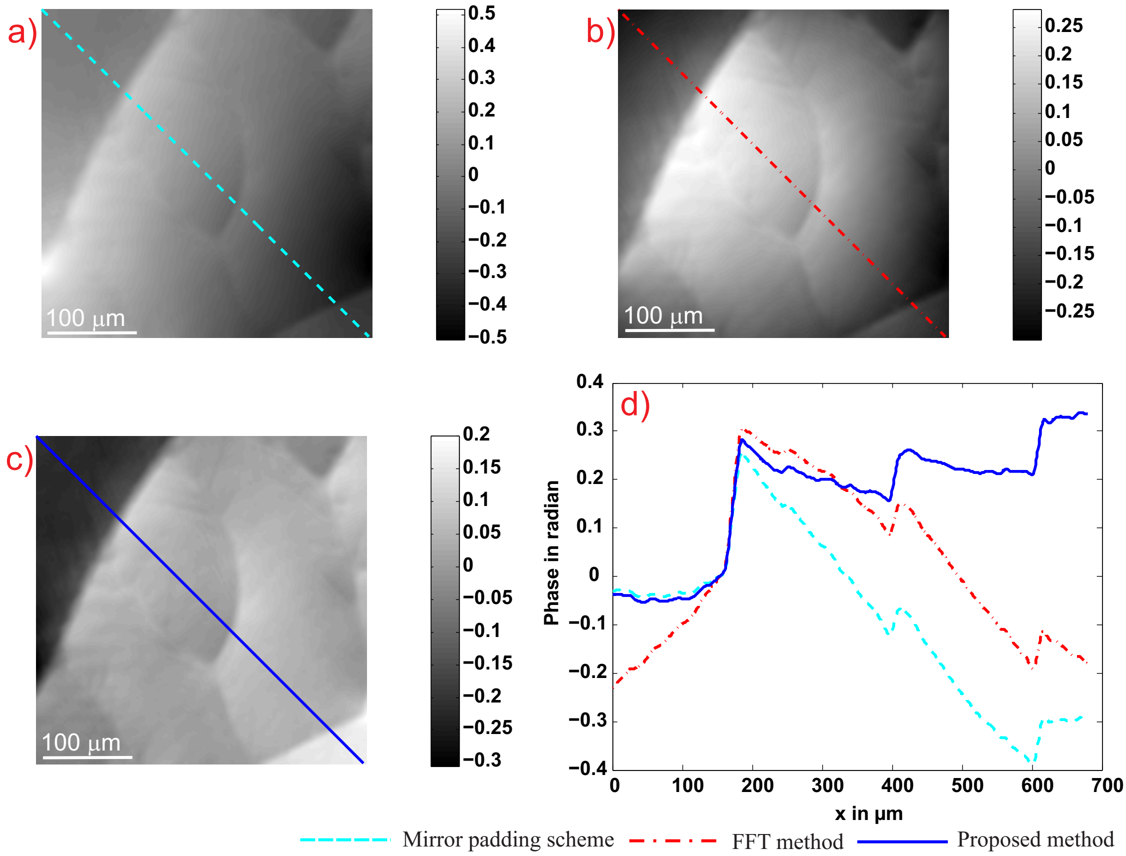

Figure 3.10: Phase maps reconstructed by three different approaches: a) the conventional FFT method (incl. padding), b) the mirror padding scheme by Volkov et al. [4], and c) our GF algorithm (same padding as for (a)). d) Diagonal line profiles extracted from each of the three reconstructions.

3.7 Conclusion

In this work, we proposed a simple iterative algorithm, gradient flipping (GF), which imposes sparsity on the phase gradient by either driving a certain percentage of values to zero, or forcing all values below a certain positive threshold to zero. By combining the conventional Fourier method with these principles adapted from the charge flipping algorithm in crystallography, GF determines boundary conditions on the phase, while preserving consistency with the higher frequencies of the experimental data.

It was shown with simulations and experiments of non-periodic and non-piecewise linear objects that these boundary conditions contribute to GF'S much improved lower spatial frequencies compared to that of the more conventional FFT method and symmetrization method.

Chapter 4

A non-convex constraint

4.1 Overview

As elucidated in the last chapter, the GFA forces the gradient of the phase below a pre-determined threshold. This non-convex constraint is advantageous to eliminate the low frequency artifact. In this chapter, the reconstructions obtained by the GFA are compared with those of the total variation minimization approach which enjoy the l_1 minimization constraint. It will be shown that the introduction of the non-convex constraint is necessary for special class of phase objects.

The material of this chapter is directly taken from [132] of which I am the first author.

4.2 Introduction

The transport of intensity equation (TIE) is a second order elliptical, non-separable and inhomogeneous partial differential equation which relates the irradiance and the variation of the irradiance along the direction of propagation to a Laplacian-like function of the phase:

$$\nabla \left(I \vec{\nabla} \varphi \right) = -k \frac{\partial I}{\partial z}. \tag{4.1}$$

The symbol $\vec{\nabla}$ denotes the gradient in the plane normal to the beam direction, I is the image intensity at the plane of interest normal to the optic axis at z, φ is the phase change induced by the sample, k is the wave vector and z is the coordinate along the direction of propagation. Since the right-hand side, $\partial I/\partial z$, is accessible through experiment as a finite difference derivative in the defocus, the phase shift, φ, can in principle, be retrieved by solving the TIE. Various authors have proposed solutions to this problem [4, 39, 133, 134], see [117] for an overview.

For the TIE to have a unique solution, the boundary conditions of the problem need to be specified. These are often taken as periodic [42], or Dirichlet or Neumann boundary conditions are assumed on the measurements' edges [4] or in a user-defined region [58]. As it is often difficult to impose realistic boundary conditions, one might opt to go without them and instead consider the TIE an underdetermined problem and remedy its ill-conditionedness and non-uniqueness by imposing one or more additional constraints to the solution. A limited degree of spatial coherence often causes the additional problem in many experimental setups that the low spatial frequency information of the $\frac{\partial I}{\partial z}$ measurement is either noisy (e.g. if the defocus has been changed only over a limited range, or at spatial frequencies approaching the lateral coherence length) and/or contains systematic errors (e.g. by some incoherent background signal or the neglect of image distortions when obtaining this measurement by a finite difference approach). Both, problems, unspecified boundary conditions, as well as unreliable low-frequency components of the measurement can be addressed by introducing physically reasonable constraints to the solution.

Oftentimes, the sought-after solution is the one sparsest in a basis suitable for the problem at hand. A naive implementation would then attempt to minimize the ℓ_0-norm of the solution in said basis. However, the non-convexity of the ℓ_0 constraint makes gradient-based optimization nearly impossible. It is the compressed sensing (CS) community's great achievement to have shown that under general and reasonable circumstances, minimization of the convex ℓ_1-norm leads to the sparsest solution all the same, thus making the problem treatable with gradient-based optimization techniques.

Total variation (TV) regularization, which aims at minimizing the ℓ_1-norm of the x- and y-derivatives of the solution, (see (4.3)) seems to have been established as a physically reasonable constraint for reducing low spatial frequency artefacts in TIE phase retrieval [52, 127]. Since the resulting solutions exhibit sparse derivatives, TV-regularization should only be considered for piece-wise constant objects.

In this work a variety of example problems is presented where conventional TV-regularization falls short and where, as expected, especially the lower spatial frequencies are problematic. It is then demonstrated that a substantial improvement in reconstruction quality is obtained if instead the ℓ_0-norm of the x- and y-derivatives, symbolically denoted $\|\nabla\|_0$ in this work, is driven to below a certain user-defined threshold.

Since gradient-based optimization cannot be invoked to make the solutions fulfill this non-convex constraint, the gradient flipping algorithm (GFA) is applied. GFA has been inspired by a class of algorithms known in crystallography as charge flipping (CF) algorithms [112], which have been shown to optimize problems with non-convex constraint sets and are able to overcome stagnation at local optima [135].

Since in both TV-regularization and $\|\nabla\|_0$ regularization, the basis which is constrained to be sparse, the gradient ∇ is the same, the improvements presented in this paper may solely be attributed to GFA's ability to deal with the non-convex constraint imposed by $\|\nabla\|_0$ regularization.

In Section 4.3 the principle of TVAL3 , a state-of-the-art TV-constrained PDE solver [106, 111], are summarized, and GFA is explained. In Section 4.4.1 the convergence of GFA is verified by comparing reconstructions of piece-wise linear objects to those obtained by TVAL3. In Section 4.4.3 the reconstruction of an object that's only partially piece-wise constant, TV-regularization contains significant low spatial frequency artefacts, $\|\nabla\|_0$ yields a much improved result. The results in Section 4.4.4 show $\|\nabla\|_0$'s superiority over TV-regularization when piece-wise linear objects are to be reconstructed. The same is true for our test on experimental data presented in section 4.5. In Section 4.6 the conclusions are drawn.

4.3 Reconstruction algorithms

In the following section, we explain the two distinct schemes to constrain the solution of the TIE, namely total variation minimization by the augmented Lagrangian method [107] and alternating direction [136] algorithms (TVAL3) and the gradient flipping algorithm (GFA) [117].

In the remainder of this paper (except for the experimental case presented in section 4.5), pure phase objects are assumed, leading to in-focus images of uniform intensity. Equation 4.1 thus simplifies to

$$\nabla^2 \varphi = -kdI_z. \tag{4.2}$$

4.3.1 TVAL3

In the TVAL3 scheme a compressed sensing problem with TV regularization is considered. Rewritten for the notations used in this paper, it reads

$$\min\ \mathrm{TV}(\varphi) \equiv \sum_i \|D_i\varphi\|_1, \quad \text{s.t. } \nabla^2\varphi = -kdI_z^{\mathrm{exp}}, \tag{4.3}$$

where $D_i\varphi$ is the 2×1 discrete-gradient vector at pixel i and dI_z^{exp} is the experimentally measured derivative of the intensity with respect to defocus.The above formulated objective may thus be described as "Of all possible solutions φ, (4.3) returns that with lowest TV".

In TVAL3, this problem is solved by minimizing the augmented Lagrangian, which is a combination of a squared penalty function and the classic Lagrangian function [106, 107]. This alleviates difficulties in connection to large squared penalty terms such as ill-conditioning and bias. As shown in [111], (4.3) can be solved fast and efficiently with an alternating directions approach.

It is worth mentioning that C. Li compared the performance of the TVAL3 with other packages such as l_1-magic [108, 109], TwIST [54] and NESTA [110] for different scenarios [106]. It was demonstrated that TVAL3 outperforms other stat-of-art implementations and has the potential to solve compressed sensing problems with TV minimization in an affordable time with high accuracy [106, 111].

Since TVAL3 is open source, it can be adjusted to one's specific needs. For this paper, the measurement matrix, ∇^2, was implemented implicitly as a two-dimensional convolution with the kernel

$$\frac{1}{4}\begin{pmatrix} 1 & 2 & 1 \\ 2 & -12 & 2 \\ 1 & 2 & 1 \end{pmatrix} \tag{4.4}$$

to avoid high memory load. The need for explicit boundary conditions was circumvented by not computing the Laplacian at the edges of the image, so that an image ϕ with dimensions $N \times N$, yields $\nabla^2\phi$ with dimensions $(N-2)\times(N-2)$. The estimated phase image is now two pixels larger in both directions than the measurements, and the boundary conditions are estimated along with the phase; in other words, TVAL3 now returns those boundaries yielding a minimum TV. For the reconstruction from experimental data in Sec. 4.5, absorption needs to be accounted for and thus the operator $\nabla I \nabla$ from eqn.(4.1) is implemented implicitly in TVAL3. This was done as a three-stage process, first the x- and y-derivatives are approximated as a central finite difference of second order accuracy, then both derivatives are multiplied with I, and finally both the x- and y-derivatives are derived with respect to x and y, respectively, and summed up. Again, the need for explicit boundary conditions was circumvented by not computing the Laplacian at the edges of the image, so that an image ϕ with dimensions $N \times N$, yields $\nabla(I\nabla\phi)$ with dimensions $(N-4)\times(N-4)$. The estimated phase image is now *four* pixels larger in both directions than the measurements.

4.3.2 Gradient flipping algorithm

In this section the gradient flipping algorithm (GFA) developed to solve the $\|\nabla\|_0$ problem will be described. The general expression (4.1) of the TIE is used to formulate the GFA. Reformulation for the special case (4.2) is trivial as one simply has to set $I = 1$. The numerical experiments in Section 4.4 all assume the special case (4.2) and thus no unfair advantage was given to $\|\nabla\|_0$ over TV-minimization.

The GFA is introduced to solve the $\|\nabla\|_0$-problem of finding the phase φ that has a certain fraction ϵ of its gradients equal to zero whilst satisfying the TIE, i.e.

$$\|\nabla\varphi\|_0 = (1-\epsilon)N^2 \text{ and } \nabla\left(I\nabla\varphi\right) = -k\frac{\partial I}{\partial z}, \tag{4.5}$$

with N^2 the number of pixels in the images. This goal is persued by iteratively flipping the sign of $\vec{\nabla}\varphi$ wherever its ℓ_1-norm is below a certain positive threshold.

The GFA makes use of the following two quantities, obtained from rearranging (4.1),

$$G = \nabla\varphi = -\frac{k}{I}\nabla\nabla^{-2}\frac{\partial I}{\partial z} \text{ and} \tag{4.6}$$

$$D = \frac{\partial I}{\partial z} = -\frac{1}{k}\nabla\left(I\nabla\varphi\right), \tag{4.7}$$

where ∇^{-2} is implemented as a division by q^2 in reciprocal space, with q the absolute value of the radial distance in reciprocal space. Furthermore, all arrays are padded to larger a size than that of the experiments to avoid problems from the periodic boundary conditions of the Fourier transforms.

At the ℓ^{th} iteration of the GFA, first the gradients are calculated

$$G^{(\ell)} = -\frac{k}{I}\nabla\nabla^{-2}D^{(\ell-1)}; \tag{4.8}$$

and then gradient flipping is applied,

$$G^{(\ell)} = \begin{cases} G^{(\ell)} & \text{if } \|G^{(\ell)}\|_1 > \delta \text{ and} \\ -\beta G^{(\ell)} & \text{if } \|G^{(\ell)}\|_1 \leq \delta, \end{cases} \tag{4.9}$$

where β is slightly below 1 and δ is chosen such that a fraction ϵ of pixels fulfills the second case; then $D^{(\ell)}$ is calculated,

$$D^{(\ell)} = -\frac{1}{k}\nabla\left(IG^{(\ell)}\right); \tag{4.10}$$

which is finally updated with the experimental measurements through

$$D^{(\ell)} = \begin{cases} D^{(\ell)} & \text{within the padding,} \\ \mathcal{F}^{-1}\left[h\mathcal{F}\left(D^{(\ell)}\right) + (1-h)\mathcal{F}\left(dI_z^{\exp}\right)\right] & \text{within the measured area,} \end{cases} \tag{4.11}$$

where $\mathcal{F}$ defines the Fourier transform and h is a Gaussian mask in reciprocal space:

$$h\left(q\right) = \exp\left(-R_{LP}^2 q^2\right). \tag{4.12}$$

The free parameter R_{LP} is chosen to minimize

$$\chi^2 = \frac{\sum\left[I^{\text{sim}}\left(R_{LP}\right) - I^{\exp}\right]^2}{\sum I^{\exp}}, \tag{4.13}$$

where $I^{\exp}$ are the experimental images, $I^{\text{sim}}\left(R_{LP}\right)$ are the images simulated from the phases obtained from the reconstruction with mask-width R_{LP}, and the summations run over the defoci and the image pixels.

The iterations start at $\ell = 1$ and $D^{(0)}$ is set to $dI_z^{\exp}$. When the algorithm is stopped, at iteration ℓ, the phase φ is calculated from

$$\varphi = -k\nabla^{-2}\nabla\frac{1}{I}\nabla\nabla^{-2}D^{(\ell)}. \tag{4.14}$$

The gradient flipping step in (4.9) is analogous to that in the charge flipping algorithms [112, 135] in crystallography, where the somewhat counter-intuitive notion was used that flipping the sign of entries with values below a certain positive threshold, drives these values to zero. In this work the same notion is employed to reach the goal in (4.5), with the small modification that the absolute value of the entries is compared against the threshold. This class of algorithms has proven to optimize problems with non-convex constraint sets and to be able to overcome stagnation at local optima [135].

4.4 Numerical experiments

4.4.1 Validation of GFA for piece-wise constant phase objects

Choosing various numerical phase-objects, we aim to investigate the performance of both algorithms namely, TVAL3 as well as GFA, for different scenarios namely, periodic and non-periodic boundary condition, partially piece-wise, piece-wise linear and the effect of noise. For all different scenarios, the intensity of the principal (focused) plane is assumed to be unity over the entire plane to mimic the pure phase-object condition. The right hand-side of eqn.(4.1) is computed by passing the original phase to the implemented two dimensional Laplace operator which resembles the ideal intensity variation along the optical axis.

A piece-wise constant head-phantom obtained by the Matlab expression '*phantom()*' is taken to be a pure phase-object with periodic boundary conditions as illustrated in Fig. 4.1(a). The intensity variation is shown in Fig. 4.1(d) and the reconstructed phase by means of GFA as well as TVAL3 are depicted in Fig. 4.1(b)

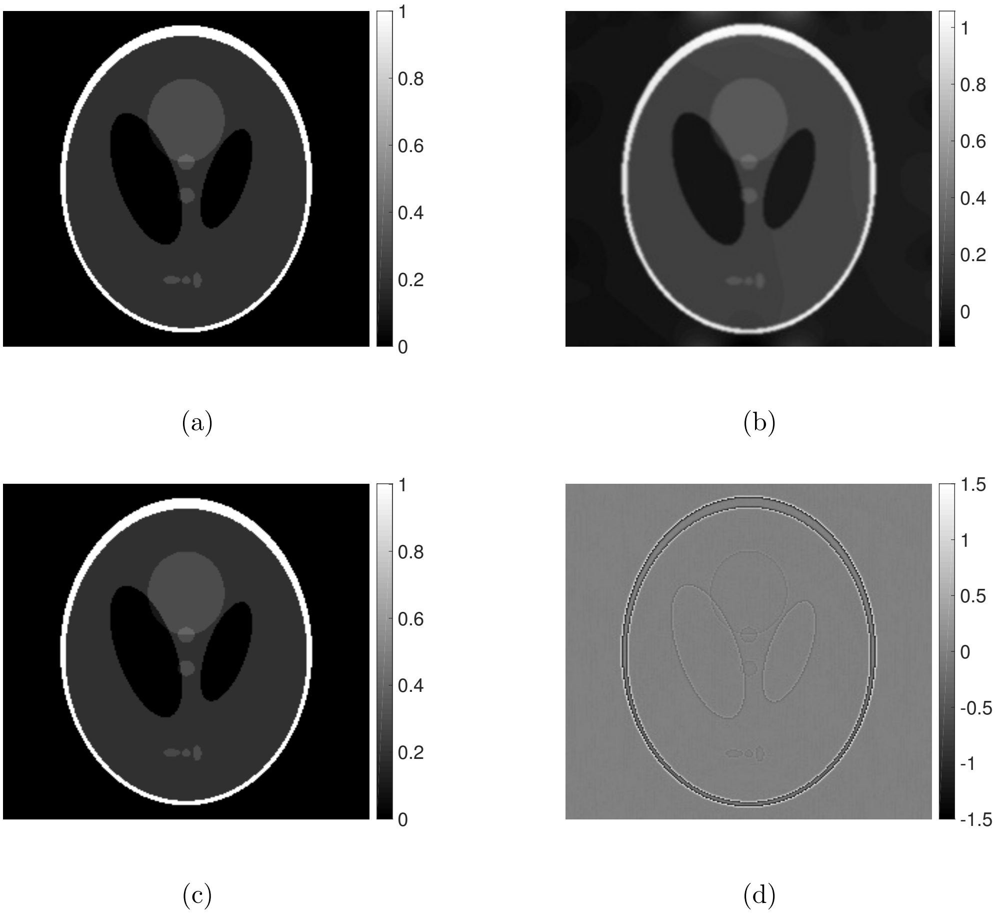

Figure 4.1: Periodic piece-wise constant phase object: a) Head-phantom original phase. b) Reconstructed phase by GFA. c) Reconstructed phase by TVAL3 d) Intensity variation along the optical axis.

and Fig. 4.1(c), respectively. It worth noting that the free parameters of the TVAL3 were optimized in such a way that no further improvement of the result could be observed.

In order to investigate the reconstruction ability of the algorithms in the case of non-periodic phase-objects, a shifted head-phantom depicted in Fig. 4.2(a) has been considered. The phases reconstructed by means of GFA as well as TVAL3 are shown in Figs. 4.2(b) and 4.2(c), respectively. The graphical representation of the measurement matrix is demonstrated in Fig. 4.2(d). Both algorithms retrieve the phase information successfully.

4.4.2 Reconstruction from noisy images

In order to evaluate the capability of both algorithms reconstruct the phase information in the presence of noise, we added 10% as well as 30% Gaussian noise. Figs. 4.3(a) and 4.3(b) show the reconstruction result of the head-phantom by means of GFA. Furthermore, Figs .4.3(c) and 4.3(d) illustrate the retrieved phase information employing the TVAL3 algorithm. The original phase is depicted in Fig. 4.3(e). In order to compare the reconstructed phases for the same measurement matrix,the root-mean-square error (RMSE) is used as a figure of merit. Table 4.1 shows the

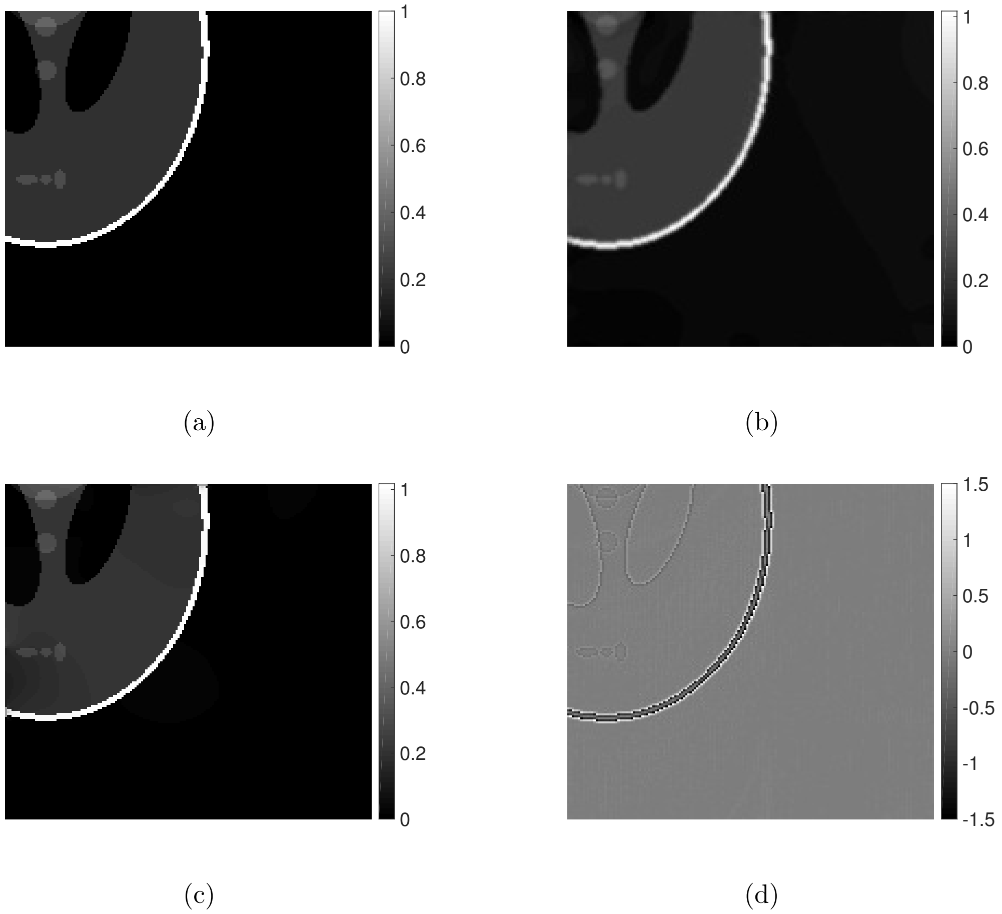

Figure 4.2: Non-periodic piece-wise constant phase object: a) Head-phantom original phase. b) Reconstructed phase by GFA. c) Reconstructed phase by TVAL3. d) Graphical representation of the measurement matrix.

RMSE for the aforementioned scenarios.

4.4.3 Partially piece-wise constant phase objects

To further investigate the performance of the GFA as well as the TVAL3 algorithm for a proper recovery of low frequency information, we constructed the partially piece-wise constant phase object shown in Fig. 4.4(a). This phase map can be obtained by the Matlab expression '*membrane()*'. Fig. 4.4(b) and Fig. 4.4(c) illustrates the reconstructed phase by means of GFA as well as TVAL3, respectively. Fig. 4.4(d) depicts the intensity variation dI_z^{exp}. It is worth noting that the TVAL3 parameters were optimized in multiple trials to obtain the best possible reconstruction , i.e. the one with the lowest RMSE. Moreover, the threshold parameter δ in GFA is refined during the reconstruction such that the number of flipped pixels is equal to one quarter of the field of view. The RMSE values of the reconstructed phase maps are shown in Table 4.1.

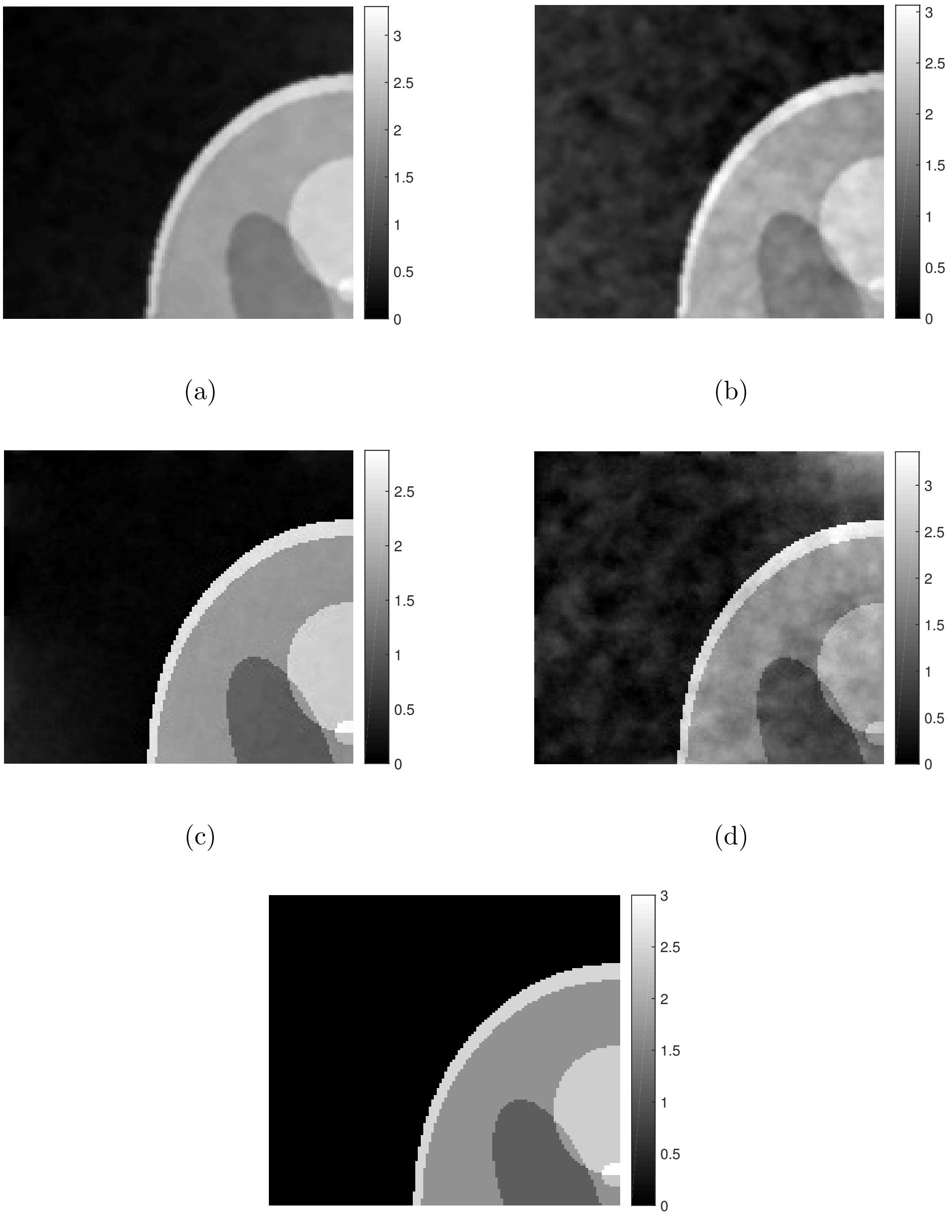

(a) (b) (c) (d) (e)

Figure 4.3: a) Reconstruction in the presence of 10dB noise by GFA. b) Reconstruction in the presence of 30dB noise by GFA. c) Reconstruction in the presence of 10dB noise by TVAL3. d) Reconstruction in the presence of 30dB noise by TVAL3. e) Original phase.

4.4.4 Piece-wise linear phase objects

Finally, the cameraman phantom shown in Fig. 4.5(a) from the Matlab built-in library of demo images was chosen as a piece-wise linear object to investigate and evaluate the capability of both phase retrieval algorithms to deal with those types of objects. Fig. 4.5(b) depicts the reconstruction phase by means of the TVAL3 approach in which $\mu = 2^5$ and $\beta = 2^4$. Fig. 4.5(c) illustrates the retrieved phase information by means of the GFA approach. The measurement matrix obtained by

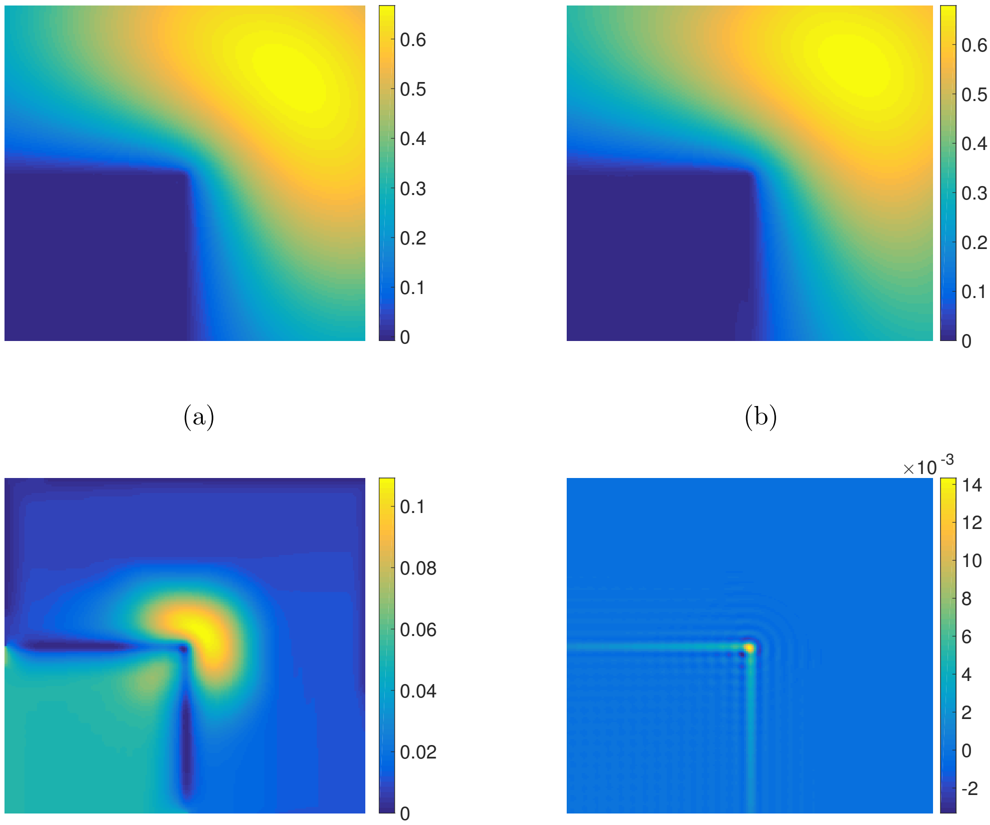

(a) (b) (c) (d)

Figure 4.4: Partially piece-wise constant phase object: a) Original phase. b) Reconstructed phase by GFA ($RMSE = 0.22$). c) Reconstructed phase by TVAL3 ($RMSE = 5.4$) d) Intensity variation in transverse plane.

applying (4.4) to the original phase is shown graphically in Fig. 4.5(d). It worth noting that again, for the TVAL3 based reconstruction the parameters have been chosen to minimize the RSME (see Table 4.1).

4.5 Experiment

Illustrated graphically in Fig. 4.6, a simple optical setup is employed to evaluate the performance of the two algorithms. The setup is comprised of a green laser emitting coherent light at a wavelength of $\lambda = 520$ nm, two lenses with focal lengths $f = 150$ mm, an iris aperture and a 2048×2048 CCD camera as a detector. The wing of a fly serves as a quasi-transparent object being placed at the distance r from the first lens where $f < r < 2f$. The iris diaphragm is positioned at the back focal plane of the first lens in order to limit the numerical aperture. Images were acquired at three different focal planes namely, $z = \Delta z$, $z = 0$ and $z = -\Delta z$ where the defocus step is $\Delta z = 1$ mm. Fig. 4.7(c) depicts the intensity variation along the optical axis which is computed from the under-focused (Fig. 4.7(b)) as well as the over-focused Fig. 4.7(a) image by the finite difference $dI_z^{\text{exp}} = \frac{I(\Delta z) - I(-\Delta z)}{2\Delta z}$.

Fig. 4.8(b) shows the reconstructed phase images obtained by means of the

(a)

(b)

(c)

(d)

Figure 4.5: Piece-wise linear phase object: a) Original phase. b) Reconstructed phase by TVAL3 ($RMSE = 1.7$). c) Reconstructed phase by GFA ($RMSE = 0.95$) d) Graphical representation of the measurement matrix.

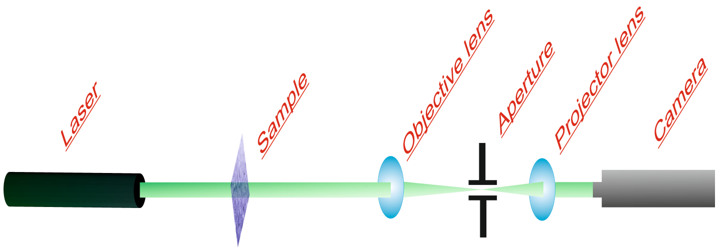

(a)

Figure 4.6: Schematic of optical setup

GFA while Fig.4.8(a) shows a conventional FFT solution which included the same padding used for the GFA but did not constrain the gradient of the phase. As clearly shown, the FFT-based reconstruction suffers from low-frequency artifact due to the periodicity of the field of view. The red line across the retrieved phase highlights the fact that the FFT-based reconstruction experiences a steep slope in the empty area where the phase should be flat (Fig. 4.8(d)) while the gradient-constrained solution is reasonably constant in the absence of any object and also in places where we expect a constant wing thickness, as shown in Fig. 4.8(e). The TVAL3 solution (Fig. 4.8(c)) fails to recover any low spatial frequency information within the wing at all.

	TV-regularization	$\|\nabla\|_0$ regularization
10% noise	1.26	3.3
30% noise	5.1	5
Partially piece-wise constant phase object	5.4	0.22
Piece-wise linear phase object	1.7	0.95

Table 4.1: RMSE of the TV-regularization as well as $\|\nabla\|_0$ regularization for different scenarios.

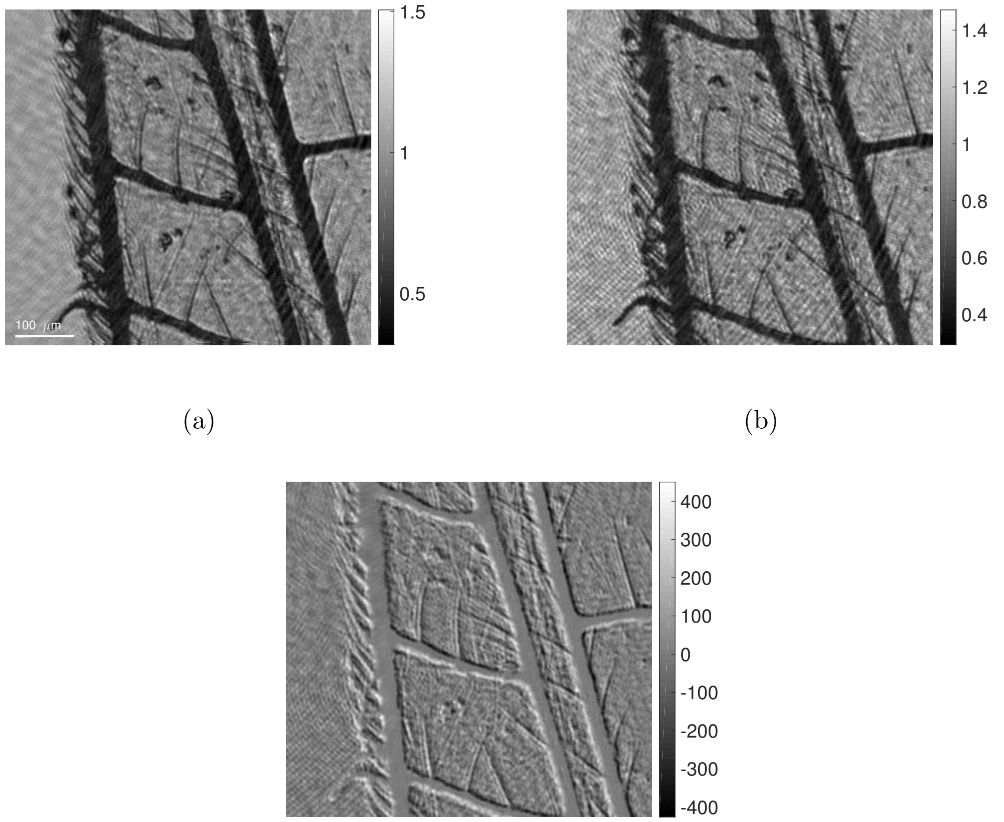

(a) (b) (c)

Figure 4.7: Experimental images a)Under-focused, b)Over-focused, c) Intensity variation along the optical axis.

4.6 Conclusions

In this paper, we compared two algorithms for removing low spatial frequency artefacts in solutions of the TIE by constraining them to be sparse in either the $l0$ norm or the $l1$ norm of their gradient, namely, gradient flipping and total variation minimization as implemented by TVAL3. While the latter imposes convex constraints in the spirit of Compressed Sensing, the former solves a non-convexly strained optimization problem. Both algorithms were able to recover piece-wise constant phase maps with and without periodic boundary conditions. In the case of noisy measurements, the GFA provided a solution which agreed slightly better with the input

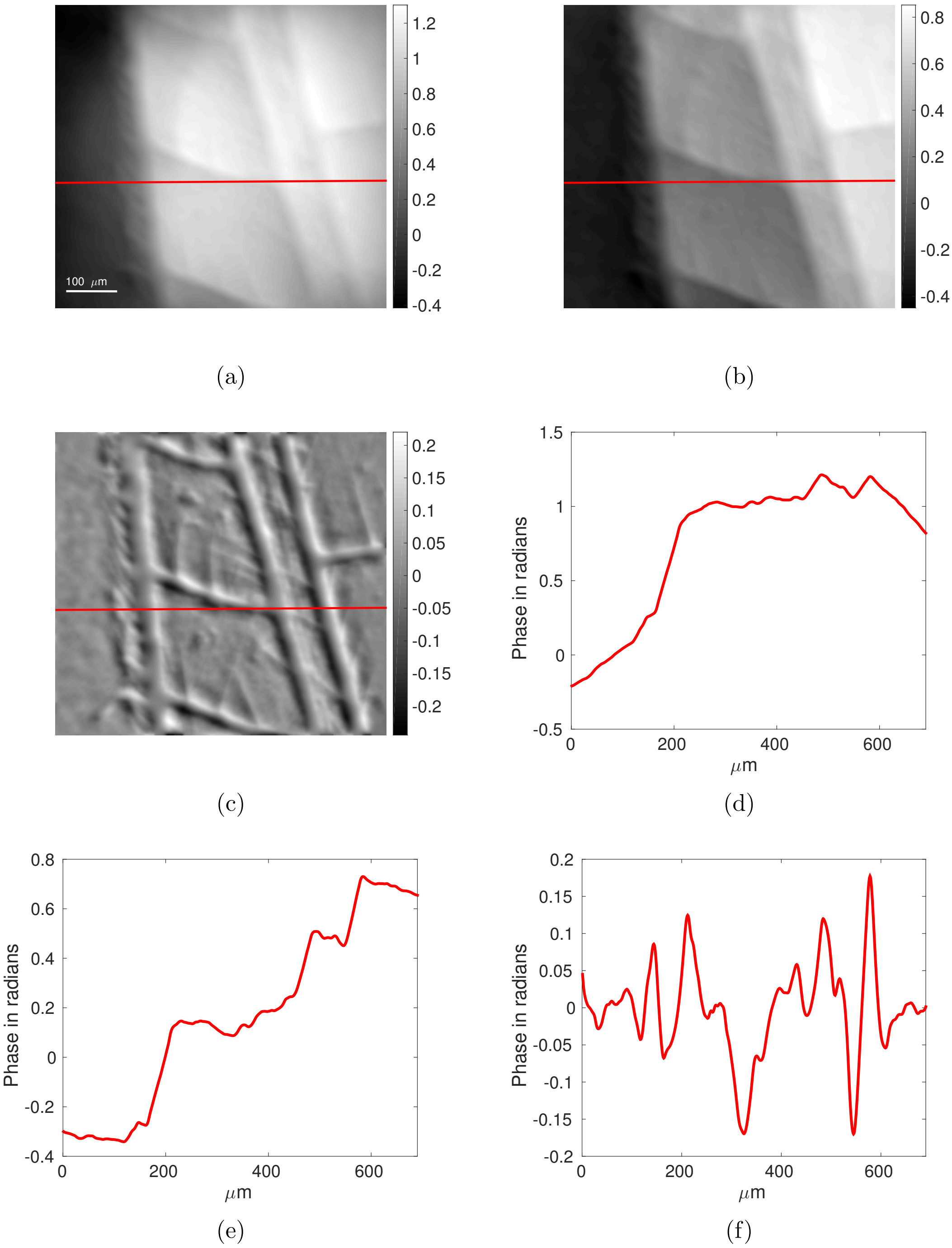

Figure 4.8: Reconstructed phase by a)FFT approach, b) GFA method, c)TV minimization approach. (d),(e) and (f) Line profiles extracted along the red lines in each of the phase maps graphically depicted above.

data at a high noise level of 30%, while performing slightly worse at a lower noise level of only 10%. For only partially piece-wise constant and piece-wise linear test objects, the GFA solution agreed much better with the original phase used to simulate the test data. In a test on experimental data the GFA provided a physically very reasonable solution, while the TV-constrained solution did not seem physically reasonable.

Chapter 5

Astigmatic Intensity equation

5.1 Overview

The focus of this research work was on the TIE up to here. However, in this chapter, the astigmatic intensity equation(AIE) is presented which unlike the TIE relies on the measurements obtained by rotating a cylindrical lens to distinct angles. This leads to an over-determined system of equation which is of great importance. An iterative algorithm is devised to solve the AIE based on fast Fourier transform. Later, periodic as well as non-periodic phase objects are chosen to investigate the performance of the algorithm in boundary value retrieval. Finally, to evaluate the ability of low as well as high frequency information reconstruction, the power spectrum of the reconstructed phase by means of AIE is compared with that of the TIE-FFT based approach as well as the original phase.

5.2 Derivation of Astigmatic intensity equation

In this section, the astigmatic intensity equation (AIE) which relates the variation of intensity to the phase shift due to the object being investigated will be derived.

To start our derivation, wave function in the image plane denoted by $\psi_i\left(x_i, y_i\right)$ is given by

$$\psi_i\left(x_i, y_i\right) = \mathcal{F}^{-1}\left\{\tilde{P}\left(-\lambda b\frac{k_x}{2\pi}, -\lambda b\frac{k_y}{2\pi}\right) \cdot \mathcal{F}\left\{\psi_o\left(x_i, y_i\right)\right\}\right\} \tag{5.1}$$

where k_x and k_y are the wave vector in the transverse plane and $\psi_o\left(x_i, y_i\right)$ denotes the object plane wave function. $\tilde{P}$ represents the general pupil function which is defined as

$$\begin{aligned} P\left(-\lambda b\frac{k_x}{2\pi}, -\lambda b\frac{k_y}{2\pi}, \phi_A\right) = P\left(-\lambda b\frac{k_x}{2\pi}, -\lambda b\frac{k_y}{2\pi}\right) \\ \exp\left(i\lambda\pi\left(\left(k_x^2 - k_y^2\right)\cos\left(2\phi_A\right) + 2k_xk_y\sin\left(2\phi_A\right)\right)\right). \end{aligned} \tag{5.2}$$

Denoting the Fourier transform of the object wave function by $\Psi_0\left(k_x, k_y\right)$, it can be written

$$\begin{aligned}\psi_i\left(x_i,y_i\right) &= \mathcal{F}^{-1}\left\{\tilde{P}\left(-\lambda b\frac{k_x}{2\pi},-\lambda b\frac{k_y}{2\pi}\right)\cdot\Psi_o\left(k_x,k_y\right)\right\} &(5.3)\\ &= \mathcal{F}^{-1}\left\{\Psi\left(k_x,k_y\right)\right\} &(5.4)\end{aligned}$$

where

$$\Psi\left(k_x,k_y\right)=\tilde{P}\left(-\lambda b\frac{k_x}{2\pi},-\lambda b\frac{k_y}{2\pi}\right)\cdot\Psi_o\left(k_x,k_y\right). \quad (5.5)$$

Therefore, the object wave function can be written as

$$\Psi\left(\vec{k_\perp},A,\phi_A\right)=\Psi_o\left(\vec{k_\perp}\right)\exp\left(i\lambda\pi\frac{A}{2}\left(\left(k_x^2-k_y^2\right)\cos\left(2\phi_A\right)+2k_xk_y\sin\left(2\phi_A\right)\right)\right), \quad (5.6)$$

where

$$\vec{k_\perp}=\begin{pmatrix}k_x\\k_y\end{pmatrix}. \quad (5.7)$$

Computing the derivative with respect to A to the object wave function yields

$$\begin{aligned}\frac{\partial}{\partial A}\Psi\left(\vec{k_\perp}\right) &= i\frac{\lambda\pi}{2}\left(\left(k_x^2-k_y^2\right)\cos\left(2\phi_A\right)+2k_xk_y\sin\left(2\phi_A\right)\right)\cdot\\ &\quad \Psi_0\left(\vec{k_\perp}\right)\cdot\exp\left(i\lambda\pi\frac{A}{2}\left(\left(k_x^2-k_y^2\right)\cos\left(2\phi_A\right)+2k_xk_y\sin\left(2\phi_A\right)\right)\right) \quad (5.8)\\ &= i\frac{\lambda\pi}{2}\left(\left(k_x^2-k_y^2\right)\cos\left(2\phi_A\right)+2k_xk_y\sin\left(2\phi_A\right)\right)\Psi\left(\vec{k_\perp}\right)\end{aligned}$$

To remind our-self, we consider a function $g\left(v\right)$ with Fourier transform $G(k_v)$. The following relation can be derived from the Fourier principle

$$\begin{aligned}\mathcal{F}\left(\frac{\partial^N}{\partial x^N}g(x)\right) &= i^Nk_x^N\cdot\mathcal{F}\left(g(x)\right) &(5.9)\\ i^{-N}\mathcal{F}^{-1}\left(\mathcal{F}\left(\frac{\partial^N}{\partial x^N}g(x)\right)\right) &= \mathcal{F}^{-1}\left(k_x^N\cdot\mathcal{F}\left(g(x)\right)\right) &(5.10)\\ i^{-N}\frac{\partial^N}{\partial x^N}g(x) &= \mathcal{F}^{-1}\left(k_x^N\cdot G(k_x)\right). &(5.11)\end{aligned}$$

For the case of $N=2$, it follows

$$-\frac{\partial^2}{\partial x^2}g(x)=\mathcal{F}^{-1}\left(k_x^2\cdot G(k_x)\right). \quad (5.12)$$

Employing Eq.5.12, inverse Fourier transform is applied to Eq.5.8 which results ($\vec{x}=(x,y)$)

$$\begin{aligned}\mathcal{F}^{-1}\left(\frac{\partial}{\partial A}\Psi\left(\vec{k_\perp}\right)\right) &= \mathcal{F}^{-1}\left(i\frac{\lambda\pi}{2}\left(\left(k_x^2-k_y^2\right)\cos\left(2\phi_A\right)+2k_xk_y\sin\left(2\phi_A\right)\right)\Psi\left(\vec{k_\perp}\right)\right)\\ \frac{\partial}{\partial A}\psi(\vec{x}) &= -i\frac{\lambda\pi}{2}\left(\left(\frac{\partial^2}{\partial x^2}-\frac{\partial^2}{\partial y^2}\right)\cos\left(2\phi_A\right)+2\frac{\partial^2}{\partial x\partial y}\sin\left(2\phi_A\right)\right)\psi\left(\vec{x}\right) \quad (5.13)\\ \frac{\partial}{\partial A}\psi(\vec{x}) &= -i\frac{\lambda\pi}{2}\cos\left(2\phi_A\right)\left(\frac{\partial^2}{\partial x^2}-\frac{\partial^2}{\partial y^2}\right)\psi(\vec{x})-2i\frac{\lambda\pi}{2}\sin\left(2\phi_A\right)\frac{\partial^2}{\partial x\partial y}\psi(\vec{x}).\end{aligned}$$

An arbitrary wave function can be written as

$$\psi(\vec{x}, A, \phi_A) = \sqrt{I(\vec{x}, A, \phi_A)} \exp\left(i\varphi(\vec{x}, A, \phi_A)\right), \tag{5.14}$$

where the intensity is defined as $I(\vec{x}, A, \phi_A) = |\psi(\vec{x}, A, \phi_A)|^2$.

Substituting Eq.5.14 into Eq.5.13, one should calculate the following relations

$$\frac{\partial}{\partial A}\psi(\vec{x}) = \frac{1}{2\sqrt{I}}\frac{\partial I}{\partial A}\exp(i\varphi) + i\sqrt{I}\frac{\partial \varphi}{\partial A}\exp(i\varphi) \tag{5.15}$$

$$\frac{\partial}{\partial x}\psi(\vec{x}) = \frac{1}{2\sqrt{I}}\frac{\partial I}{\partial x}\exp(i\varphi) + i\sqrt{I}\frac{\partial \varphi}{\partial x}\exp(i\varphi). \tag{5.16}$$

$$\begin{aligned}\frac{\partial^2}{\partial x^2}\psi(\vec{x}) &= -\frac{1}{4I^{\frac{3}{2}}}\left(\frac{\partial I}{\partial x}\right)^2 \exp(i\varphi) + \frac{1}{2\sqrt{I}}\frac{\partial^2 I}{\partial x^2}\exp(i\varphi) + \frac{i}{\sqrt{I}}\frac{\partial I}{\partial x}\frac{\partial \varphi}{\partial x}\exp(i\varphi) + \\ &\quad + i\sqrt{I}\frac{\partial^2 \varphi}{\partial x^2}\exp(i\varphi) - \sqrt{I}\left(\frac{\partial \varphi}{\partial x}\right)^2 \exp(i\varphi)\end{aligned} \tag{5.17}$$

$$\begin{aligned}\frac{\partial^2}{\partial x \partial y}\psi(\vec{x}) &= -\frac{1}{4I^{\frac{3}{2}}}\frac{\partial^2 I}{\partial x \partial y}\exp(i\varphi) + \frac{1}{2\sqrt{I}}\frac{\partial^2 I}{\partial x \partial y}\exp(i\varphi) + \frac{i}{2\sqrt{I}}\frac{\partial I}{\partial x}\frac{\partial \varphi}{\partial y}\exp(i\varphi) \\ &\quad + i\frac{1}{2\sqrt{I}}\frac{\partial I}{\partial y}\frac{\partial \varphi}{\partial x}\exp(i\varphi) + i\sqrt{I}\frac{\partial^2 \varphi}{\partial x \partial y}\exp(i\varphi) - \sqrt{I}\frac{\partial^2 \varphi}{\partial x \partial y}\exp(i\varphi)\end{aligned} \tag{5.18}$$

It should be mentioned that the derivation with respect to y is similar to that of x. Substituting Eq.5.15 to Eq.5.18 into Eq.5.13 while keeping the real part and dividing to $\exp(i\varphi)$ leads to

$$\begin{aligned}\frac{1}{2\sqrt{I}}\frac{\partial I}{\partial A} &= -i\frac{\lambda\pi}{2}\cos(2\phi_A)\left[\frac{i}{\sqrt{I}}\frac{\partial I}{\partial x}\frac{\partial \varphi}{\partial x} + i\sqrt{I}\frac{\partial^2 \varphi}{\partial x^2} - \frac{i}{\sqrt{I}}\frac{\partial I}{\partial y}\frac{\partial \varphi}{\partial y} - i\sqrt{I}\frac{\partial^2 \varphi}{\partial y^2}\right] \\ &\quad -2i\frac{\lambda\pi}{2}\sin(2\phi_A)\left[\frac{i}{2\sqrt{I}}\frac{\partial I}{\partial x}\frac{\partial \varphi}{\partial y} + \frac{i}{2\sqrt{I}}\frac{\partial I}{\partial y}\frac{\partial \varphi}{\partial x} + i\sqrt{I}\frac{\partial^2 \varphi}{\partial x \partial y}\right].\end{aligned} \tag{5.19}$$

The above derivation can be further simplified by multiplying both side to $2\sqrt{I}$ which results

$$\begin{aligned}\frac{1}{2\pi\lambda}\frac{\partial I}{\partial A} &= \cos(2\phi_A)\left[\frac{\partial I}{\partial x}\frac{\partial \varphi}{\partial x} - \frac{\partial I}{\partial y}\frac{\partial \varphi}{\partial y} + I\left(\frac{\partial^2 \varphi}{\partial x^2} - \frac{\partial^2 \varphi}{\partial y^2}\right)\right] \\ &\quad + \sin(2\phi_A)\left[\frac{\partial I}{\partial x}\frac{\partial \varphi}{\partial y} + \frac{\partial I}{\partial y}\frac{\partial \varphi}{\partial x} + 2I\frac{\partial^2 \varphi}{\partial x \partial y}\right],\end{aligned} \tag{5.20}$$

which is called AIE.

Assuming $\phi_A = 0°$, then we have

$$\frac{1}{2\pi\lambda}\frac{\partial I}{\partial A} \overset{\phi_A = 0°}{=} 1 \cdot \left[\frac{\partial I}{\partial x}\frac{\partial \varphi}{\partial x} - \frac{\partial I}{\partial y}\frac{\partial \varphi}{\partial y} + I\left(\frac{\partial^2 \varphi}{\partial x^2} - \frac{\partial^2 \varphi}{\partial y^2}\right)\right] \tag{5.21}$$

$$= deriv1 \tag{5.22}$$

therefore,

$$deriv1 = \frac{\partial I}{\partial x}\frac{\partial \varphi}{\partial x} - \frac{\partial I}{\partial y}\frac{\partial \varphi}{\partial y} + I\left(\frac{\partial^2 \varphi}{\partial x^2} - \frac{\partial^2 \varphi}{\partial y^2}\right). \tag{5.23}$$

Furthermore, assuming $\phi_A = 45°$, then we have

$$\frac{1}{2\pi\lambda}\frac{\partial I}{\partial A} \overset{\phi_A = 45°}{=} 1 \cdot \left[\frac{\partial I}{\partial x}\frac{\partial \varphi}{\partial y} + \frac{\partial I}{\partial y}\frac{\partial \varphi}{\partial x} + 2I\frac{\partial^2 \varphi}{\partial x \partial y}\right] \tag{5.24}$$

$$= deriv2 \tag{5.25}$$

therefore,

$$deriv2 = \frac{\partial I}{\partial x}\frac{\partial \varphi}{\partial y} + \frac{\partial I}{\partial y}\frac{\partial \varphi}{\partial x} + 2I\frac{\partial^2 \varphi}{\partial x \partial y}. \tag{5.26}$$

5.3 Inversion of AIE

In this section, we will derived the inverse AIE by first writing it in matrix notation.

$$\frac{1}{2\pi\lambda}\frac{\partial I}{\partial A} = \frac{\partial I}{\partial x}\left[\cos(2\phi_A)\frac{\partial \varphi}{\partial x} + \sin(2\phi_A)\frac{\partial \varphi}{\partial y}\right] + \frac{\partial I}{\partial y}\left[-\cos(2\phi_A)\frac{\partial \varphi}{\partial y} + \sin(2\phi_A)\frac{\partial \varphi}{\partial x}\right]$$
$$+I\left[\cos(2\phi_A)\left(\frac{\partial^2 \varphi}{\partial x^2} - \frac{\partial^2 \varphi}{\partial y^2}\right) + 2\sin(2\phi_A)\frac{\partial^2 \varphi}{\partial x \partial y}\right] \tag{5.27}$$

$$= \begin{pmatrix} \frac{\partial I}{\partial x} & \frac{\partial I}{\partial y} \end{pmatrix} \begin{pmatrix} \cos(2\phi_A)\frac{\partial \varphi}{\partial x} + \sin(2\phi_A)\frac{\partial \varphi}{\partial y} \\ -\cos(2\phi_A)\frac{\partial \varphi}{\partial y} + \sin(2\phi_A)\frac{\partial \varphi}{\partial x} \end{pmatrix}$$
$$+I\left[\cos(2\phi_A)\left(\frac{\partial^2 \varphi}{\partial x^2} - \frac{\partial^2 \varphi}{\partial y^2}\right) + 2\sin(2\phi_A)\frac{\partial^2 \varphi}{\partial x \partial y}\right]. \tag{5.28}$$

$$= \begin{pmatrix} \frac{\partial}{\partial x} & \frac{\partial}{\partial y} \end{pmatrix} I \begin{pmatrix} \cos(2\phi_A)\frac{\partial}{\partial x} + \sin(2\phi_A)\frac{\partial}{\partial y} \\ -\cos(2\phi_A)\frac{\partial}{\partial y} + \sin(2\phi_A)\frac{\partial}{\partial x} \end{pmatrix} \varphi \tag{5.29}$$

with the operator $\vec{\nabla}_A$ defined as

$$\vec{\nabla}_A = \begin{pmatrix} \cos(2\phi_A)\frac{\partial}{\partial x} + \sin(2\phi_A)\frac{\partial}{\partial y} \\ -\cos(2\phi_A)\frac{\partial}{\partial y} + \sin(2\phi_A)\frac{\partial}{\partial x} \end{pmatrix} \tag{5.30}$$

$$= \begin{pmatrix} \cos(2\phi_A) & \sin(2\phi_A) \\ \sin(2\phi_A) & -\cos(2\phi_A) \end{pmatrix} \begin{pmatrix} \frac{\partial}{\partial x} \\ \frac{\partial}{\partial y}. \end{pmatrix} \tag{5.31}$$

Therefore, Eq.5.29 can be simplified in more compact form as following

$$\frac{1}{2\pi\lambda}\frac{\partial I}{\partial A} = \vec{\nabla} I \, \vec{\nabla}_A \varphi. \tag{5.32}$$

Solving Eq.5.32 for unknown φ leads to

$$\varphi = \frac{1}{2\pi\lambda}\vec{\nabla}_A^{-1}\left(\frac{\vec{\nabla}^{-1}\left(\frac{\partial I(\vec{x})}{\partial A}\right)}{I(\vec{x})}\right). \tag{5.33}$$

Now, we define the operator D_A as following

$$D_A = \frac{\partial}{\partial x} + i\frac{\partial}{\partial y}. \tag{5.34}$$

Therefore, the inverse of D_A represented by D_A^{-1} is

$$D_A^{-1} = \frac{D_A^*}{|D_A|^2} = \frac{\frac{\partial}{\partial x} - i\frac{\partial}{\partial y}}{\frac{\partial^2}{\partial x^2} + \frac{\partial^2}{\partial y^2}} = \left(\frac{\partial}{\partial x} - i\frac{\partial}{\partial y}\right)\triangle^{-1}, \tag{5.35}$$

where $\triangle^{-1}$ denotes the inverse Laplace. Employing the defined operator D_A as well as substituting in Eq.5.32 results

$$\begin{aligned}
\frac{1}{2\pi\lambda}\frac{\partial I}{\partial A} &= D_A I\, D_A\varphi && (5.36)\\
&= \left(\frac{\partial}{\partial x} + i\frac{\partial}{\partial y}\right)\left(I\left[\frac{\partial\varphi}{\partial x} + i\frac{\partial\varphi}{\partial y}\right]\right) && (5.37)\\
&= \frac{\partial I}{\partial x}\frac{\partial\varphi}{\partial x} + I\frac{\partial^2\varphi}{\partial x^2} + i\frac{\partial I}{\partial x}\frac{\partial\varphi}{\partial y} + iI\frac{\partial^2\varphi}{\partial x\partial y}\\
&\quad + i\frac{\partial I}{\partial y}\frac{\partial\varphi}{\partial x} + iI\frac{\partial^2\varphi}{\partial y\partial x} - \frac{\partial I}{\partial y}\frac{\partial\varphi}{\partial y} - I\frac{\partial^2\varphi}{\partial y^2} && (5.38)\\
&= \frac{\partial I}{\partial x}\frac{\partial\varphi}{\partial x} - \frac{\partial I}{\partial y}\frac{\partial\varphi}{\partial y} + I\left(\frac{\partial^2\varphi}{\partial x^2} - \frac{\partial^2\varphi}{\partial y^2}\right)\\
&\quad + i\left(\frac{\partial I}{\partial x}\frac{\partial\varphi}{\partial y} + \frac{\partial I}{\partial y}\frac{\partial\varphi}{\partial x} + 2I\frac{\partial^2\varphi}{\partial x\partial y}\right) && (5.39)\\
&= deriv1 + i\cdot deriv2. && (5.40)
\end{aligned}$$

We then replace the term $deriv1$ and $deriv2$ with Eq.5.22 as well as Eq.5.25, respectively. Therefore,

$$deriv1 = \frac{1}{2\pi\lambda}\frac{\partial I}{\partial A}\bigg|_{\phi_A=0^\circ} \tag{5.41}$$

$$deriv2 = \frac{1}{2\pi\lambda}\frac{\partial I}{\partial A}\bigg|_{\phi_A=45^\circ} \tag{5.42}$$

and hence, we have the following relation

$$\frac{\partial I}{\partial A} = \frac{\partial I}{\partial A}\bigg|_{\phi_A=0^\circ} + i\cdot\frac{\partial I}{\partial A}\bigg|_{\phi_A=45^\circ}. \tag{5.43}$$

Finally, the unknown phase can be computed by employing Eq.5.36

$$\begin{aligned}
D_A I\, D_A\varphi &= \frac{1}{2\pi\lambda}\frac{\partial I}{\partial A} && (5.44)\\
D_A I\, D_A\varphi &= deriv1 + i\cdot deriv2 && (5.45)\\
I\, D_A\varphi &= D_A^{-1}\left(deriv1 + i\cdot deriv2\right) && (5.46)\\
\varphi &= D_A^{-1}\left(\frac{D_A^{-1}\left(deriv1 + i\cdot deriv2\right)}{I}\right) && (5.47)
\end{aligned}$$

Of course, we want to idially average this for a number of different angles. This equation will generally result in a complex quantity for the phase φ. However, φ has to be real. The boundary conditions have thus to be adjusted to make φ real. This is done by padding the arrays we are working with and iteratively projecting between the constraints given by the experimental data and the constraint that φ has to be real.

5.4 Reconstruction algorithm

Intensity in the image plane denoted by $I(x, y, A) = I_A$ can be expanded utilizing the Taylor series to the first order as following

$$I_A = I_0 + A \frac{\partial I}{\partial A}\bigg|_{A=0}, \tag{5.48}$$

where $I(x, y, A = 0) = I_0$ is the intensity when astigmatism is zero. Therefore, the intensity variation with respect to the astigmatism amplitude reads as

$$\frac{\partial I}{\partial A}\bigg|_{A=0} = \frac{I_A - I_0}{A}. \tag{5.49}$$

Bearing in the mind that $I_{-A}(\phi_A) = I_A(\phi_A + 90°)$, therefore, Eq.5.49 is reformulated as

$$\frac{\partial I}{\partial A}\bigg|_{A=0} = \frac{I_A(\phi_A) - I_A(\phi_A + 90°)}{2A}. \tag{5.50}$$

Employing Eq.5.50, the term $deriv1$ and $deriv2$ is computed using the following relations

$$deriv1 = \frac{\partial I}{\partial A}\bigg|_{\phi_A=0°} = \frac{I_A(\phi_A = 0°) - I_A(\phi_A = 90°)}{2A} \tag{5.51}$$

and

$$deriv2 = \frac{\partial I}{\partial A}\bigg|_{\phi_A=45°} = \frac{I_A(\phi_A = 45°) - I_A(\phi_A = 135°)}{2A}. \tag{5.52}$$

Therefore, the unknown phase is computed by substituting Eq.5.51 as well as Eq.5.52 into Eq.5.47 which reads as

$$\varphi = D_A^{-1}\left(\frac{D_A^{-1}\left(\frac{I_A(\phi_A=0°)-I_A(\phi_A=90°)}{2A} + i \cdot \frac{I_A(\phi_A=45°)-I_A(\phi_A=135°)}{2A}\right)}{I_0}\right). \tag{5.53}$$

As mentioned earlier I_0 is the intensity in the reference plane where the astigmatism is zero. However, since removing the cylindrical lens in order to acquire zero astigmatic image is not experimentally feasible, we compute the intensity in reference plane from following relation

$$I_0 = \frac{1}{\sum \phi_A} \sum_{\phi_A} I_A(\phi_A). \tag{5.54}$$

Moreover, it is evident from Eq.5.53 that four images at distinct angles namely, $\phi_A = 0°$, $45°$, $90°$ and $135°$, should be recorded to visualize the unknown phase map.

The reconstruction algorithm starts by padding the reference intensity in order to prevent the periodic boundary condition effect inherent to Fast Fourier Transform(FFT) approach which is employed to compute the inverse Laplacian. Then, Eq.5.51 as well as Eq.5.52 are hired to compute the $derive1$ and $derive2$ quantities.

Having calculated intensity variation with respect to astigmatic amplitude for two distinct angle namely, $\phi_A = 0°$ and $\phi_A = 45°$, Eq.5.53 is used to compute the unknown φ. It is of great importance to note that φ is complex quantity and since, the phase is physical as well as real quantity, therefore, we keep the real part and ignore the imaginary part of the reconstructed phase. Then, the reconstructed φ is back-projected and substituted on the right hand side of Eq.5.45. Having computed the new intensity derivative, the information in the padded area is kept while the retrieved data is replaced by the experimental measurement in experimental area. This is done to ensure the consistency between simulated data and experimental information. We continue to iterate as long as the difference between subsequent phase reconstruction falls below a pre-defined threshold.

5.5 Numerical experiments

In this section, we would like to investigate the performance of the proposed reconstruction algorithm for different scenarios namely, phase with periodic boundary condition as well as non-periodic boundary condition and in the presence of the different levels of noise.

5.5.1 Periodic boundary condition

The Matlab head phantom is used as phase of a phase object with periodic boundary condition as shown in Fig.5.1(a). This phantom is obtained by Matlab command *'Phantom()'* with the pixel size of 0.01μm.

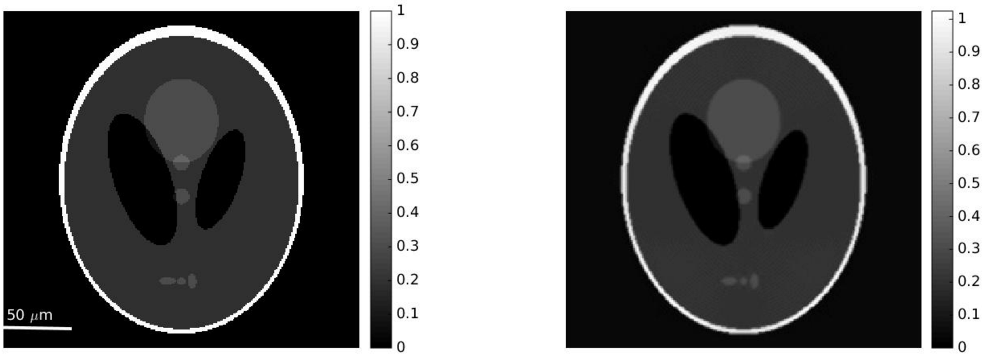

(a) (b)

Figure 5.1: a) Original phase. b) Reconstructed phase by proposed approach

The simulated images have been padded out from 256×256 pixels by a factor of two to yield image size of 512×512. Fig.5.2 illustrates the simulated images at the different angles with the astigmatic amplitude equal to $1mm$. Having obtained the simulated data for different angles, Eq.5.52 as well as Eq.5.51 are employed to yield the $derive2$ and $derive1$ quantities.

Having fed the algorithm with the simulated measurements, Fig.5.1(b) shows the reconstructed phase which visually resembles the original phase.

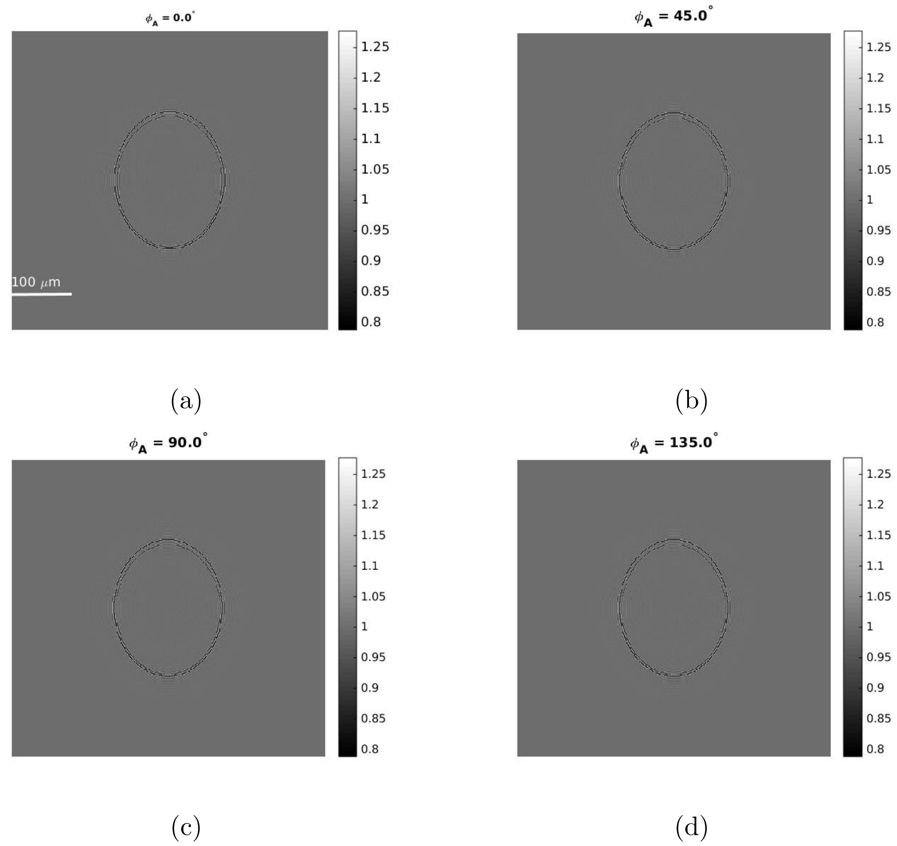

Figure 5.2: Simulated intensity images at different angles a) $\phi_A = 0°$, b) $\phi_A = 45°$, c) $\phi_A = 90°$, d) $\phi_A = 135°$

In order to evaluate the performance of the proposed algorithm in reconstruction of low as well as high spatial frequencies, we compare the power spectrum of the original phase with that retrieved by the proposed method as well as the TIE where we employed the FFT approach. As shown in Fig.5.3, the power spectrum of the reconstructed phase by proposed method based on the astigmatic set of equations is closer to the original one in comparison to that of the reconstructed by solving TIE via FFT approach especially, in very low as well as very high spatially frequencies. However, it is worth noting that both of the approaches namely, TIE and AIE, retrieved the middle range frequencies almost equally faithfully.

5.5.2 Non-Periodic boundary condition

In order to asses the performance of the proposed method in case of non-period boundary condition phase object, we construct a piece-wise non-periodic phase object which is shown in Fig.5.4(a). The size of the simulated test object is 624 × 624 pixels which is padded by a factor of two to yield a 1248 × 1248 image size with pixel size of 1μm. Fig.5.5 illustrates the simulated images at the different angles namely, $\phi_A = 0°$, $\phi_A = 45°$, $\phi_A = 90°$ and $\phi_A = 135°$ with the astigmatic amplitude equal to $1m$m.

Having provided the intensities at different angles, we let the algorithm iterate. Fig.5.4(b) shows the reconstructed phase. Fig.5.4(c) shows the data extracted along the red line to compare the retrieved boundary values of the reconstructed phase

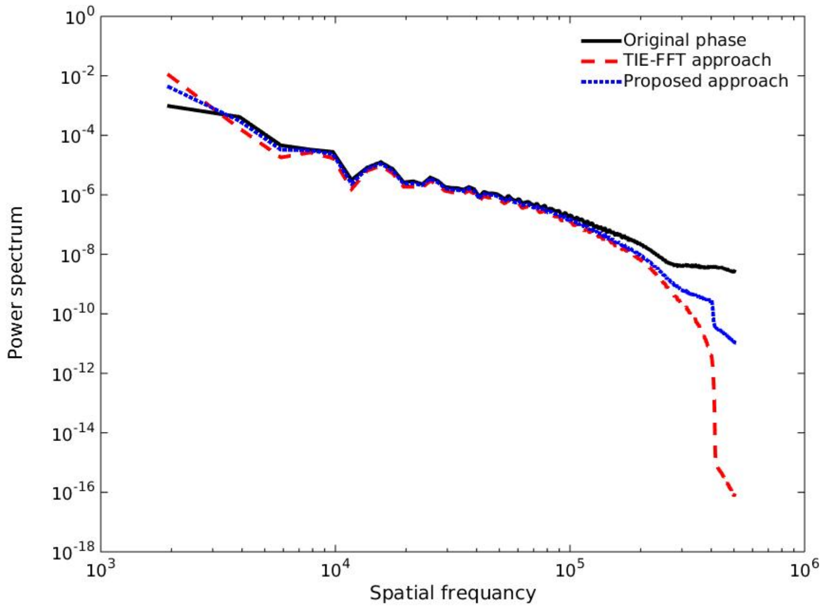

Figure 5.3: Power spectrum of the original phase as well as that of the reconstructed by suggested method and TIE-FFT approach

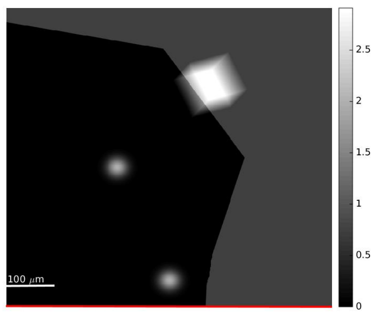

(a)

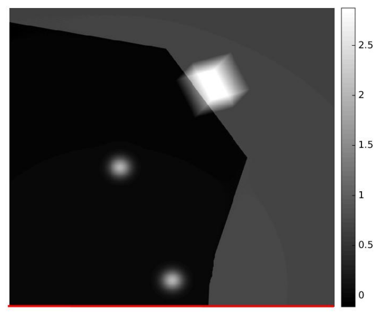

(b)

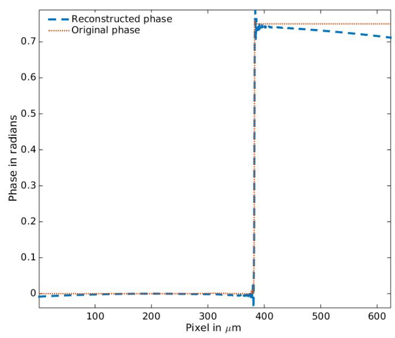

(c)

Figure 5.4: a)Original phase. b)Reconstructed phase. c)The line profile of the extracted data along the red line.

with that of the original. As shown clearly, the proposed approach is capable of reconstructing boundary values. We attribute this feature to the mathematical nature of the astigmatic equation which allow us to have over determined system of equation in which there is more than one measurement data for each point.

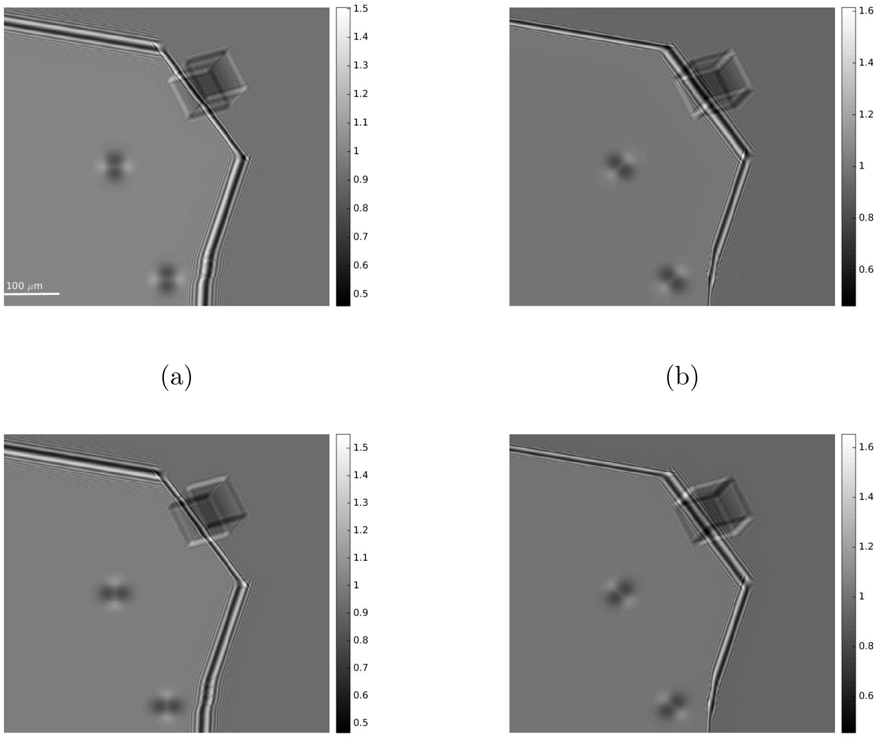

(a) (b) (c) (d)

Figure 5.5: Simulated intensity images at different angles a) $\phi_A = 0°$, b) $\phi_A = 45°$, c) $\phi_A = 90°$, d) $\phi_A = 135°$

In order to further analyze the suggested approach toward the AIE, we compare the power spectrum of the original phase with the reconstructed phase by the suggested approach and that of the TIE-FFT based approach. As shown in Fig 5.6, although both of the aforementioned algorithms are capable of reconstructing the middle range frequencies, but the proposed approach reconstructs the low and high spatially frequencies more precisely. Therefore, the proposed approach based on the astigmatic equation outperforms the TIE based approach as well as reflecting the superiority of the proposed approach to retrieve the low and high spatial frequencies.

5.6 Noise impact

In this section, we would like to evaluate the performance of the algorithm in the presence of the noise. Therefore, we corrupted the images in such a way that $PSNR = 24.92$ dB where PSNR is the peak signal to noise ratio defined as

$$PSNR = 10.\log_{10}\left(\frac{M^2}{MSE}\right) \tag{5.55}$$

where M is the maximum value of the image and MSE denotes the mean squared error.

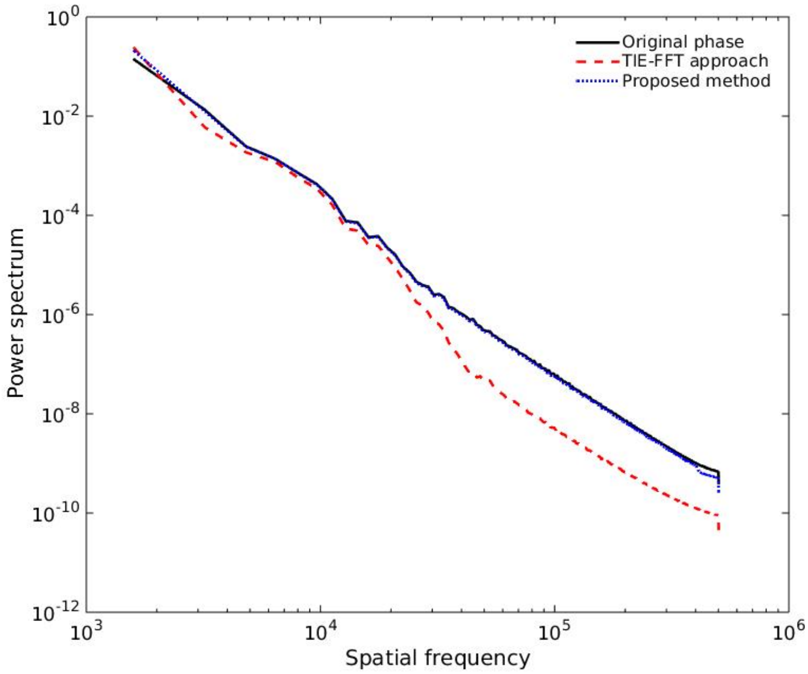

Figure 5.6: Power spectrum of the original phase as well as that of the reconstructed by suggested method and TIE-FFT approach

Having provided the measurements, we let the algorithm to iterate 1113 epochs. The reconstructed phase as well as the original phase are shown in Fig.5.7. We attribute the cloudy features of the reconstructed phase to the presence of the noise.

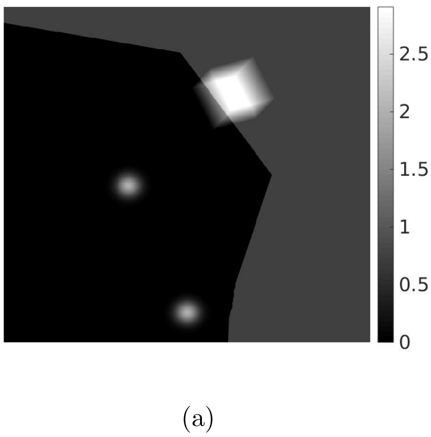

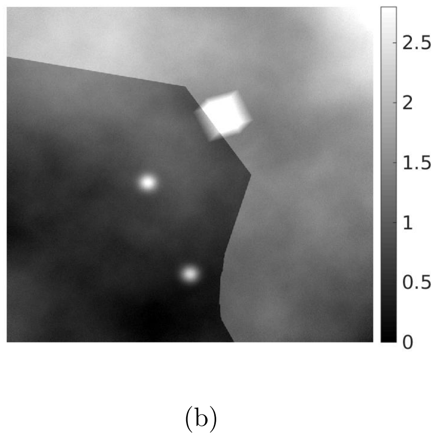

Figure 5.7: a) Original phase. b) Reconstructed phase by proposed approach

5.7 Summary

A novel phase reconstruction method based on the astigmatic intensity equation (AIE) is presented. AIE offers not only a simple experimental setup but also, an over determined system of equation. However, like TIE, AIE suffers from the non-uniqueness as well as ill-conditionedness of the solution. An iterative algorithm is suggested which benefits from the unique feature of AIE (i.e. over determined system of equation) in which boundary values in the padded area updated until the convergence criteria is fulfilled. Finally, numerical experiment shows that the AIE is not only capable of retrieving the boundary values but also, in comparison to the TIE, low frequency as well as high frequency information is reconstructed more precisely.

Chapter 6

Summary and conclusion

The transport of intensity equation (TIE) owing to its simple mathematical formulation as well as straight forward experimental procedure has applications across many disciplines such as optical microscopy, X-ray imaging, electron microscopy, etc. The TIE relates the intensity variation along the optical axis in transverse plane to the phase of the unknown object. However, being a second order elliptical partial differential equation, the need for boundary condition is inevitable in order to obtain a unique solution which is difficult to obtained experimentally. Therefore, the main focus of this research work is on proposing new algorithms to get around the problem of ill-conditionedness and non-uniqueness.

In chapter 2, a new combination of flux preserving as well as Dirichlet boundary conditions is presented. While flux preserving boundary conditions are applied to the outer field of view, the Dirichlet boundary condition is imposed to the perimeter of a polygon which covers the free area. A finite element based software namely, Comsol, is employed to impose the above-mentioned boundary condition on the experimental measurement to reconstruct the wave front of the wing of a fly as a quasi-transparent object under investigation. Besides, due to the fact that the TIE is an elliptical partial differential equation, the implemented multigrid solver minimizes the computation time. Furthermore, the effect of padding on both the proposed methods as well as the FFT approach is investigated. It is shown that although the proposed approach my benefit from increasing amount of the padding the FFT approach reflects strong low spatial frequency atifacts in the case of a non-periodic object due to the fact that the FFT implicitly assumes periodic boundary conditions which does not reflect the physical fact. Although the finite element based method is applicable in many cases there exist scenarios where the free area in the image plane is not accessible.

In chapter 3, the gradient flipping (GF) algorithm is presented. The GF combines the well known FFT solution of the TIE with the principle adapted from the charge flipping (CF) algorithm in order to find the sparsest solution in the gradient space. To accomplish the task, fist the intensity variation is padded to almost two times the original size and then the phase is computed by means of the FFT approach. Having computed the phase, the CF algorithm is implemented in the gradient space either to force all values below a certain predetermined threshold to zero or a certain percentage of values to zero. Later, the modified phase is utilized to calculate the new intensity variation. The boundary information in the padded area is kept while the simulated data is replaced by experimental data to assure the consistency between experimental data and boundary condition. Finally, the modified intensity variation is back-projected and the procedure continues until the convergence criteria is fulfilled. The application of the GF to experimental data and comparison with the conventional method demonstrate an improved retrieval of the low spatial frequencies of the phase especially where the phase is either non-periodic or non-piecewise linear.

In chapter 4, the phase reconstructed by two approaches namely, GF algorithm which introduced in the chapter 3 and the total variation minimization in which the l_1 norm of the gradient is minimized, for different scenarios are compared. It is shown for periodic as well as non-periodic piece-wise constant phase objects, both algorithm retrieve the phase information successfully. Furthermore, a partially piece-wise constant phase object is chosen to evaluate the ability of a proper low frequency reconstruction. As demonstrated in chapter 4, the GF's reconstruction manifests lower RMSE. While the TV-minimization based algorithm performs better in the presence of 10% noise, the GF algorithm reconstruction outperforms that of the TVAL3 in the presence of 30% noise. Finally, experimental demonstration reflects that the GF reconstruction provides physically reasonable solution in comparison to that of the TV-regularization based approach in which the low frequency information is missing and thus, did not seem physically reasonable. It is of great importance to note that the GF algorithm imposes a non-convex constraint, i.e. forcing the gradient below a certain threshold, while the TV-minimization approach imposes the convex constraint, i.e. minimization of l_1 norm. Therefore, it is strongly believed the introduction of the non-convex constraint will pave the way to increase the range of applicability of the TIE.

In chapter 5, a completely new approach toward wave front reconstruction with the astigmatic intensity equation (AIE) is presented. First, the derivation of the AIE is presented. It is shown that the AIE offers an over-determined system of equations which is of great importance. In other words, for each point on the phase map, more than one point in the measurement map exist in which the number of corespondent points depend on the number of measurements. It is worth noting that the AIE like the TIE has a unique solution for strictly positive intensity up a constant additive. An algorithm to solve the AIE is carefully devised and the performance of algorithm is investigated by several numerical examples. Periodic as well as non-periodic phase objects are chosen to evaluate the performance of the algorithm. It is shown that the suggested algorithm is capable of a successful reconstruction. To further analyze the ability of the AIE to reconstruct low as well as high spatial frequencies, the retrieved phases are compared with that obtained by employing the TIE-FFT based approach. The power spectrum of the reconstructed phases illustrate that the AIE reconstructs the low frequency as well as high frequency information more precisely.

Although the proposed algorithm performs successfully for the case of the test data, it is of great interest to investigate and evaluate the performance of the above-mentioned algorithm for the case of experimental data. However, one of the possible challenges would be the distortion due to the cylindrical lens. It needs further research on how to characterize the distortion of a corresponding optical setup and devise an algorithm to effectively remove the off-axis aberration and distortions. Furthermore, the AIE is derived under the assumption of a coherent light, however, most of the practical sources are incoherent or partially coherent. Thus more research is required to investigate the effect of different light sources on the AIE formulation. Moreover, accurate estimation of intensity variation plays a vital role in a precise reconstruction. Although the proposed algorithm in chapter 5 benefits from a simple finite difference method to estimate the intensity variation, more research on developing new approaches to estimate an accurate intensity variation is needed.

Appendix A

List of Publications and Conference contribution

[1] K. Song, C. T. Koch, J. K. Lee, D. Y. Kim, J. K. Kim, A. Parvizi, W. Y. Jung, C. G. Park, H. J. Jeong, H. S. Kim, *et al.*, “Correlative high-resolution mapping of strain and charge density in a strained piezoelectric multilayer,” *Advanced Materials Interfaces*, vol. 2, no. 1, 2015.

[2] A. Parvizi, J. Müller, S. Funken, and C. Koch, “A practical way to resolve ambiguities in wavefront reconstructions by the transport of intensity equation,” *Ultramicroscopy*, vol. 154, pp. 1–6, 2015.

[3] A. Parvizi, W. V. den Broek, and C.T.Koch, “Recovering low spatial frequencies in wavefront sensing based on intensity measurements,” *advanced structural and chemical imaging*, vol. Submitted, 2016.

[4] A. Parvizi, W. V. den Broek, and C.T.Koch, “The gradient flipping algorithm: introducing non-convex constraints in wavefront reconstructions with the transport of intensity equation,” *Optics Express*, vol. Submitted, 2016.

[5] P. Bakhtiarpour, A. Parvizi, M. Müller, M. Shahinpoor, O. Marti, and M. Amirkhani, “An external disturbance sensor for ionic polymer metal composite actuators,” *Smart Materials and Structures*, vol. 25, no. 1, p. 015008, 2015.

[6] A. Parvizi, C. Koch, “ Solving the transport of intensity equation using flux-preserving boundary conditions,” *IMC*, Prague(czech republic), 2014,

[7] A. Parvizi, C.T. Koch, “ A Charge Flipping Based Wavefront Reconstruction Algorithm by the Transport of Intensity Equation ,” *Microscopy Conference*, Göttingen(Germany), 2015,

[8] C. Ozsoy-Keskinbora, W. Van den Broek, A. Parvizi, C. Boothroyd, H.J. Kleebe, R. Dunin-Borkowski, P. van Aken , C.T. Koch“ An Overview of the Electron Holography Studies in Max Planck Institute for Solid State Research,” *Microscopy Microscopy Congress*, Istanbul(Turkey), 2015,

Bibliography

[1] Joseph W Goodman. *Introduction to Fourier optics*. Roberts and Company Publishers, 2005.

[2] William L Briggs, Steve F McCormick, et al. *A multigrid tutorial*. Siam, 2000.

[3] V. V. Volkov, Y. Zhu, and M. De Graef. A new symmetrized solution for phase retrieval using the transport of intensity equation. *Micron (Oxford, England : 1993)*, 33(5):411–416, January 2002. ISSN 0968-4328. URL http://www.ncbi.nlm.nih.gov/pubmed/24787811.

[4] VV Volkov, Y Zhu, and M De Graef. A new symmetrized solution for phase retrieval using the transport of intensity equation. *Micron*, 33(5):411–416, 2002.

[5] Peter W Hawkes. *Advances in imaging and electron physics*, volume 128. Academic Press, 2003.

[6] Frits Zernike. Phase contrast, a new method for the microscopic observation of transparent objects. *Physica*, 9(7):686–698, 1942.

[7] G Nomarski and AR Weill. Application à la métallographie des méthodes interférentielles à deux ondes polarisées. *Rev. Metall*, 2:121–128, 1955.

[8] Robert Hoffman and Leo Gross. Modulation contrast microscope. *Applied Optics*, 14(5):1169–1176, 1975.

[9] Parameswaran Hariharan. *Basics of interferometry*. Academic Press, 2010.

[10] P Cloetens, W Ludwig, J Baruchel, D Van Dyck, J Van Landuyt, JP Guigay, and M Schlenker. Holotomography: Quantitative phase tomography with micrometer resolution using hard synchrotron radiation x rays. *Applied Physics Letters*, 75(19):2912–2914, 1999.

[11] Wim Coene, Guido Janssen, Marc Op de Beeck, and Dirk Van Dyck. Phase retrieval through focus variation for ultra-resolution in field-emission transmission electron microscopy. *Physical Review Letters*, 69(26):3743, 1992.

[12] Michael Reed Teague. Deterministic phase retrieval: a green's function solution. *JOSA*, 73(11):1434–1441, 1983.

[13] Isi web of science. http://apps.webofknowledge.com/. Accessed: 2015 - June - 17.

[14] LJ Allen, HML Faulkner, KA Nugent, MP Oxley, and David Paganin. Phase retrieval from images in the presence of first-order vortices. *Physical Review E*, 63(3):037602, 2001.

[15] José A Rodrigo and Tatiana Alieva. Recovery of schell-model partially coherent beams. *Optics letters*, 39(4):1030–1033, 2014.

[16] José A Rodrigo and Tatiana Alieva. Rapid quantitative phase imaging for partially coherent light microscopy. *Optics express*, 22(11):13472–13483, 2014.

[17] TE Gureyev, Ya I Nesterets, DM Paganin, A Pogany, and SW Wilkins. Linear algorithms for phase retrieval in the fresnel region. 2. partially coherent illumination. *Optics communications*, 259(2):569–580, 2006.

[18] George Ade. On the validity of the transport equation for the intensity in optics. *Optics communications*, 52(5):307–310, 1985.

[19] A Barty, KA Nugent, D Paganin, and A Roberts. Quantitative optical phase microscopy. *Optics Letters*, 23(11):817–819, 1998.

[20] David Paganin and Keith A Nugent. Noninterferometric phase imaging with partially coherent light. *Physical review letters*, 80(12):2586, 1998.

[21] TE Gureyev, DM Paganin, AW Stevenson, SC Mayo, and SW Wilkins. Generalized eikonal of partially coherent beams and its use in quantitative imaging. *Physical review letters*, 93(6):068103, 2004.

[22] Adam M Zysk, P Scott Carney, and John C Schotland. Eikonal method for calculation of coherence functions. *Physical review letters*, 95(4):043904, 2005.

[23] Jonathan C Petruccelli, Lei Tian, and George Barbastathis. The transport of intensity equation for optical path length recovery using partially coherent illumination. *Optics express*, 21(12):14430–14441, 2013.

[24] Kazuo Ishizuka. Contrast transfer of crystal images in tem. *Ultramicroscopy*, 5(1):55–65, 1980.

[25] AV Martin, F-R Chen, W-K Hsieh, J-J Kai, SD Findlay, and LJ Allen. Spatial incoherence in phase retrieval based on focus variation. *Ultramicroscopy*, 106 (10):914–924, 2006.

[26] Christoph T Koch. A flux-preserving non-linear inline holography reconstruction algorithm for partially coherent electrons. *Ultramicroscopy*, 108(2):141–150, 2008.

[27] Emil Wolf. New theory of partial coherence in the space-frequency domain. part i: spectra and cross spectra of steady-state sources. *JOSA*, 72(3):343–351, 1982.

[28] Adam M Zysk, Robert W Schoonover, P Scott Carney, and Mark A Anastasio. Transport of intensity and spectrum for partially coherent fields. *Optics letters*, 35(13):2239–2241, 2010.

[29] Rudolph Emil Kalman. A new approach to linear filtering and prediction problems. *Journal of Fluids Engineering*, 82(1):35–45, 1960.

[30] Zhong Jingshan, Lei Tian, Justin Dauwels, and Laura Waller. Partially coherent phase imaging with simultaneous source recovery. *Biomedical Optics Express*, 6(1):257–265, 2015.

[31] Martin J Bastiaans. Application of the wigner distribution function to partially coherent light. *JOSA A*, 3(8):1227–1238, 1986.

[32] Chao Zuo, Qian Chen, Lei Tian, Laura Waller, and Anand Asundi. Transport of intensity phase retrieval and computational imaging for partially coherent fields: The phase space perspective. *Optics and Lasers in Engineering*, 71: 20–32, 2015.

[33] TE Gureyev, A Roberts, and KA Nugent. Partially coherent fields, the transport-of-intensity equation, and phase uniqueness. *JOSA A*, 12(9):1942–1946, 1995.

[34] EG Abramochkin and VG Volostnikov. Relationship between two-dimensional intensity and phase in a fresnel diffraction zone. *Optics communications*, 74 (3):144–148, 1989.

[35] Axel Lubk, Giulio Guzzinati, Felix Börrnert, and Jo Verbeeck. Transport of intensity phase retrieval of arbitrary wave fields including vortices. *Physical review letters*, 111(17):173902, 2013.

[36] J Matías Di Martino, Gastón A Ayubi, Enrique A Dalchiele, Julia R Alonso, Ariel Fernández, Jorge L Flores, César D Perciante, and José A Ferrari. Single-shot phase recovery using two laterally separated defocused images. *Optics Communications*, 293:1–3, 2013.

[37] Jelena A Schmalz, Timur E Gureyev, David M Paganin, and Konstantin M Pavlov. Phase retrieval using radiation and matter-wave fields: Validity of teague's method for solution of the transport-of-intensity equation. *Physical review A*, 84(2):023808, 2011.

[38] M Born and Emil Wolf. Principles of optics, 6th (corrected) ed, 1980.

[39] TE Gureyev, A Roberts, and KA Nugent. Phase retrieval with the transport-of-intensity equation: matrix solution with use of zernike polynomials. *JOSA A*, 12(9):1932–1942, 1995.

[40] Timur E Gureyev and Keith A Nugent. Phase retrieval with the transport-of-intensity equation. ii. orthogonal series solution for nonuniform illumination. *JOSA A*, 13(8):1670–1682, 1996.

[41] In Woo Han. New method for estimating wavefront from curvature signal by curve fitting. *Optical Engineering*, 34(4):1232–1237, 1995.

[42] Timur E Gureyev and Keith A Nugent. Rapid quantitative phase imaging using the transport of intensity equation. *Optics communications*, 133(1): 339–346, 1997.

[43] M Soto, S Ríos, and E Acosta. Role of boundary conditions in phase estimation by transport of intensity equation. *Optics communications*, 184(1):19–24, 2000.

[44] Aaron Lewis and Igor Tikhonenkov. Noninterferometric phase calculation for paraxial beams using intensity distribution. *Optics communications*, 246(1): 21–24, 2005.

[45] François Roddier and Claude Roddier. Wavefront reconstruction using iterative fourier transforms. *Applied Optics*, 30(11):1325–1327, 1991.

[46] KA Nugent, TE Gureyev, DF Cookson, D Paganin, and Z Barnea. Quantitative phase imaging using hard x rays. *Physical review letters*, 77(14):2961, 1996.

[47] Chao Zuo, Qian Chen, Lei Huang, and Anand Asundi. Phase discrepancy analysis and compensation for fast fourier transform based solution of the transport of intensity equation. *Optics express*, 22(14):17172–17186, 2014.

[48] Chao Zuo, Qian Chen, and Anand Asundi. Boundary-artifact-free phase retrieval with the transport of intensity equation: fast solution with use of discrete cosine transform. *Optics express*, 22(8):9220–9244, 2014.

[49] Andreĭ Tikhonov. *Solutions of ill-posed problems*.

[50] Kazuo Ishizuka and Brendan Allman. Phase measurement of atomic resolution image using transport of intensity equation. *Journal of electron microscopy*, 54(3):191–197, 2005.

[51] A Yan, X Wu, and H Liu. A robust general phase retrieval method for medical applications. *Journal of Instrumentation*, 8(05):C05007, 2013.

[52] Lei Tian, Jonathan C Petruccelli, and George Barbastathis. Nonlinear diffusion regularization for transport of intensity phase imaging. *Optics letters*, 37 (19):4131–4133, 2012.

[53] Lei Tian, Jonathan C Petruccelli, Qin Miao, Haris Kudrolli, Vivek Nagarkar, and George Barbastathis. Compressive x-ray phase tomography based on the transport of intensity equation. *Optics letters*, 38(17):3418–3421, 2013.

[54] José M Bioucas-Dias and Mário AT Figueiredo. A new twist: two-step iterative shrinkage/thresholding algorithms for image restoration. *Image Processing, IEEE Transactions on*, 16(12):2992–3004, 2007.

[55] Emmanuel Froustey, Emrah Bostan, Stamatios Lefkimmiatis, and Michael Unser. Digital phase reconstruction via iterative solutions of transport-of-intensity equation. In *Information Optics (WIO), 2014 13th Workshop on*, pages 1–3. Ieee, 2014.

[56] Shlomo Ta'asan. Multigrid one-shot methods and design strategy. *Lecture Notes on Optimization*, 4, 1997.

[57] Bindang Xue and Shiling Zheng. Phase retrieval using the transport of intensity equation solved by the fmg–cg method. *Optik-International Journal for Light and Electron Optics*, 122(23):2101–2106, 2011.

[58]

[59] TE Gureyev, A Pogany, DM Paganin, and SW Wilkins. Linear algorithms for phase retrieval in the fresnel region. *Optics communications*, 231(1):53–70, 2004.

[60] Timur E Gureyev. Composite techniques for phase retrieval in the fresnel region. *Optics Communications*, 220(1):49–58, 2003.

[61] James R Fienup. Phase retrieval algorithms: a comparison. *Applied optics*, 21(15):2758–2769, 1982.

[62] Jean Pierre Guigay, Max Langer, Renaud Boistel, and Peter Cloetens. Mixed transfer function and transport of intensity approach for phase retrieval in the fresnel region. *Optics letters*, 32(12):1617–1619, 2007.

[63] Max Langer, Peter Cloetens, and Françoise Peyrin. Regularization of phase retrieval with phase-attenuation duality prior for 3-d holotomography. *Image Processing, IEEE Transactions on*, 19(9):2428–2436, 2010.

[64] Nghia T Vo, Robert C Atwood, Herbert O Moser, Peter D Lee, Mark BH Breese, and Michael Drakopoulos. A fast-converging iterative method for x-ray in-line phase contrast tomography. *Applied Physics Letters*, 101(22):224108, 2012.

[65] D Van Dyck and W Coene. A new procedure for wave function restoration in high resolution electron microscopy. *Optik*, 77(3):125–128, 1987.

[66] Marco Beleggia, MA Schofield, VV Volkov, and Y Zhu. On the transport of intensity technique for phase retrieval. *Ultramicroscopy*, 102(1):37–49, 2004.

[67] M Soto, E Acosta, and S Ríos. Performance analysis of curvature sensors: optimum positioning of the measurement planes. *Optics express*, 11(20):2577–2588, 2003.

[68] Marcos Soto and Eva Acosta. Improved phase imaging from intensity measurements in multiple planes. *Applied optics*, 46(33):7978–7981, 2007.

[69] J Martinez-Carranza, K Falaggis, and T Kozacki. Optimum measurement criteria for the axial derivative intensity used in transport of intensity-equation-based solvers. *Optics letters*, 39(2):182–185, 2014.

[70] Laura Waller, Lei Tian, and George Barbastathis. Transport of intensity phase-amplitude imaging with higher order intensity derivatives. *Optics express*, 18(12):12552–12561, 2010.

[71] Bindang Xue, Shiling Zheng, Linyan Cui, Xiangzhi Bai, and Fugen Zhou. Transport of intensity phase imaging from multiple intensities measured in unequally-spaced planes. *Optics express*, 19(21):20244–20250, 2011.

[72] Shiling Zheng, Bindang Xue, Wenfang Xue, Xiangzhi Bai, and Fugen Zhou. Transport of intensity phase imaging from multiple noisy intensities measured in unequally-spaced planes. *Optics express*, 20(2):972–985, 2012.

[73] Zhong Jingshan, Rene A Claus, Justin Dauwels, Lei Tian, and Laura Waller. Transport of intensity phase imaging by intensity spectrum fitting of exponentially spaced defocus planes. *Optics express*, 22(9):10661–10674, 2014.

[74] Rui Bie, Xiu-Hua Yuan, Ming Zhao, and Li Zhang. Method for estimating the axial intensity derivative in the tie with higher order intensity derivatives and noise suppression. *Optics express*, 20(7):8186–8191, 2012.

[75] Abraham Savitzky and Marcel JE Golay. Smoothing and differentiation of data by simplified least squares procedures. *Analytical chemistry*, 36(8):1627–1639, 1964.

[76] Chao Zuo, Qian Chen, Yingjie Yu, and Anand Asundi. Transport-of-intensity phase imaging using savitzky-golay differentiation filter-theory and applications. *Optics express*, 21(5):5346–5362, 2013.

[77] Jiamin Wu, Xing Lin, Yebin Liu, Lei Tian, Laura Waller, and Qionghai Dai. Coded aperture pair for phase imaging. In *Computational Optical Sensing and Imaging*, pages CTh3C–4. Optical Society of America, 2014.

[78] Laura Waller, Shan Shan Kou, Colin JR Sheppard, and George Barbastathis. Phase from chromatic aberrations. *Optics express*, 18(22):22817–22825, 2010.

[79] TE Gureyev and SW Wilkins. On x-ray phase retrieval from polychromatic images. *Optics communications*, 147(4):229–232, 1998.

[80] Dieter Richter Georg Roth Thomas Brückel, Gernot Heger and Reiner Zor. *Neutron Scattering (2014)*. ForschungsZentrum Jülich GmbH, 2014.

[81] A Cimmino, GI Opat, AG Klein, H Kaiser, SA Werner, M Arif, and R Clothier. Observation of the topological aharonov-casher phase shift by neutron interferometry. *Physical review letters*, 63(4):380, 1989.

[82] BE Allman, PJ McMahon, KA Nugent, D Paganin, DL Jacobson, M Arif, SA Werner, et al. Phase radiography with neutrons. *Nature (London)*, 408 (6809):158–159, 2000.

[83] Eberhard Lehmann, Klaus Lorenz, Erich Steichele, and Peter Vontobel. Non-destructive testing with neutron phase contrast imaging. *Nuclear Instruments and Methods in Physics Research Section A: Accelerators, Spectrometers, Detectors and Associated Equipment*, 542(1):95–99, 2005.

[84] Herbert Hopster and Hans Peter Oepen. *Magnetic microscopy of nanostructures*. Springer Science & Business Media, 2006.

[85] S McVitie and M Cushley. Quantitative fresnel lorentz microscopy and the transport of intensity equation. *Ultramicroscopy*, 106(4):423–431, 2006.

[86] Marc De Graef and Yimei Zhu. Quantitative noninterferometric lorentz microscopy. *Journal of Applied Physics*, 89(11):7177–7179, 2001.

[87] Yimei Zhu, Viacheslav V Volkov, and Marc De Graef. Understanding magnetic structures in permanent magnets via in situ lorentz microscopy, interferometric and non-interferometric phase-reconstructions. *Journal of electron microscopy*, 50(6):447–455, 2001.

[88] VV Volkov and Y Zhu. Lorentz phase microscopy of magnetic materials. *Ultramicroscopy*, 98(2):271–281, 2004.

[89] A Kohn, AK Petford-Long, and TC Anthony. Magnetic potential in patterned materials determined using energy-dependent lorentz phase microscopy. *Physical Review B*, 72(1):014444, 2005.

[90] E Humphrey, C Phatak, AK Petford-Long, and M De Graef. Separation of electrostatic and magnetic phase shifts using a modified transport-of-intensity equation. *Ultramicroscopy*, 139:5–12, 2014.

[91] LA Rodríguez, C Magen, E Snoeck, L Serrano-Ramón, C Gatel, R Córdoba, E Martinez-Vecino, L Torres, JM De Teresa, and MR Ibarra. Optimized cobalt nanowires for domain wall manipulation imaged by in situ lorentz microscopy. *Applied Physics Letters*, 102(2):022418, 2013.

[92] LA Rodríguez, C Magén, E Snoeck, C Gatel, C Castán-Guerrero, J Sesé, LM García, J Herrero-Albillos, J Bartolomé, F Bartolomé, et al. High-resolution imaging of remanent state and magnetization reversal of superdomain structures in high-density cobalt antidot arrays. *Nanotechnology*, 25 (38):385703, 2014.

[93] Tim C Petersen, Vicki J Keast, and David M Paganin. Quantitative tem-based phase retrieval of mgo nano-cubes using the transport of intensity equation. *Ultramicroscopy*, 108(9):805–815, 2008.

[94] TC Petersen, M Bosman, VJ Keast, and GR Anstis. Plasmon resonances and electron phase shifts near au nanospheres. *Applied Physics Letters*, 93(10): 101909, 2008.

[95] VJ Keast, MJ Gladys, TC Petersen, Christian Dwyer, CT Koch, T Haber, and G Kothleitner. Energy-filtered phase retrieval using the transport of intensity equation. *Applied Physics Letters*, 99(22):221905, 2011.

[96] Jens Als-Nielsen and Des McMorrow. *Elements of modern X-ray physics*. John Wiley & Sons, 2011.

[97] TE Gureyev, C Raven, A Snigirev, I Snigireva, and SW Wilkins. Hard x-ray quantitative non-interferometric phase-contrast microscopy. *Journal of Physics D: Applied Physics*, 32(5):563, 1999.

[98] Andrew FT Leong, David M Paganin, Stuart B Hooper, Melissa L Siew, and Marcus J Kitchen. Measurement of absolute regional lung air volumes from near-field x-ray speckles. *Optics express*, 21(23):27905–27923, 2013.

[99] J Moosmann, V Altapova, L Helfen, D Hänschke, R Hofmann, and T Baumbach. High-resolution x-ray phase-contrast tomography from single-distance radiographs applied to developmental stages of xenopus laevis. In *Journal of Physics: Conference Series*, volume 425, page 192003. IOP Publishing, 2013.

[100] Andrei V Bronnikov. Theory of quantitative phase-contrast computed tomography. *JOSA A*, 19(3):472–480, 2002.

[101] Max Langer, Peter Cloetens, Jean-Pierre Guigay, and Françoise Peyrin. Quantitative comparison of direct phase retrieval algorithms in in-line phase tomography. *Medical physics*, 35(10):4556–4566, 2008.

[102] David Paganin, SC Mayo, Tim E Gureyev, Peter R Miller, and Steve W Wilkins. Simultaneous phase and amplitude extraction from a single defocused image of a homogeneous object. *Journal of microscopy*, 206(1):33–40, 2002.

[103] MA Beltran, DM Paganin, Kentaro Uesugi, and MJ Kitchen. 2d and 3d x-ray phase retrieval of multi-material objects using a single defocus distance. *Optics express*, 18(7):6423–6436, 2010.

[104] Amela Groso, Marco Stampanoni, Rafael Abela, Philipp Schneider, Srujan Linga, and R Müller. Phase contrast tomography: an alternative approach. *Applied physics letters*, 88(21):214104, 2006.

[105] Jonathan Barzilai and Jonathan M Borwein. Two-point step size gradient methods. *IMA Journal of Numerical Analysis*, 8(1):141–148, 1988.

[106] Chengbo Li. *Compressive sensing for 3D data processing tasks: applications, models and algorithms*. PhD thesis, Rice University, 2011.

[107] Jorge Nocedal and Stephen Wright. *Numerical optimization*. Springer Science & Business Media, 2006.

[108] Emmanuel J Candès, Justin Romberg, and Terence Tao. Robust uncertainty principles: Exact signal reconstruction from highly incomplete frequency information. *Information Theory, IEEE Transactions on*, 52(2):489–509, 2006.

[109] Emmanuel J Candes and Terence Tao. Decoding by linear programming. *Information Theory, IEEE Transactions on*, 51(12):4203–4215, 2005.

[110] Stephen Becker, Jérôme Bobin, and Emmanuel J Candès. Nesta: a fast and accurate first-order method for sparse recovery. *SIAM Journal on Imaging Sciences*, 4(1):1–39, 2011.

[111] Chengbo Li. An efficient algorithm for total variation regularization with applications to the single pixel camera and compressive sensing. Master's thesis, Rice University, 2009.

[112] Gábor Oszlányi and András Süto. The charge flipping algorithm. *Acta Crystallographica Section A: Foundations of Crystallography*, 64(1):123–134, 2007.

[113] T. C. Petersen, V. J. Keast, K. Johnson, and S. Duvall. Tem-based phase retrieval of p-n junction wafers using the transport of intensity equation. *Philosophical Magazine*, 87:3565–3578, 2007.

[114] C. Ophus and T. Ewalds. Guidelines for quantitative reconstruction of complex exit waves in HRTEM. *Ultramicroscopy*, 113:88–95, 2012.

[115] Axel Lubk, Giulio Guzzinati, Felix Börrnert, and Jo Verbeeck. Transport of Intensity Phase Retrieval of Arbitrary Wave Fields Including Vortices. *Physical Review Letters*, 111(17):173902–173905, October 2013. ISSN 0031-9007. doi: 10.1103/PhysRevLett.111.173902. URL `http://link.aps.org/doi/10.1103/PhysRevLett.111.173902`.

[116] J. Martinez-Carranza, K. Falaggis, T. Kozacki, and M. Kujawinska. Effect of Imposed Boundary conditions on the accuracy of Transport of Intensity based solvers. *SPIE Optical Metrology 2013*, 8789:87890N–87890N, May 2013. doi: 10.1117/12.2020662. URL `http://proceedings.spiedigitallibrary.org`.

[117] A. Parvizi, W. V. den Broek, and C.T.Koch. Recovering low spatial frequencies in wavefront sensing based on intensity measurements. *advanced structural and chemical imaging*, Submitted, 2016.

[118] Dennis Gabor et al. A new microscopic principle. *Nature*, 161(4098):777–778, 1948.

[119] R. W. Gerchberg and W. O. Saxton. A practical algorithm for the determination of the phase from image and diffraction plane pictures. *Optik*, 35:237–246, 1972.

[120] Earl J Kirkland. Improved high resolution image processing of bright field electron micrographs: I. theory. *Ultramicroscopy*, 15(3):151–172, 1984.

[121] P. Schiske. Zur frage der bildrekonstruktion durch fokusreihen. In *Proc. 4th Europ. Congr. on Electron Microscopy, Rome, Vol. 1*, pages 145–146, 1968.

[122] D. Paganin and K. A. Nugent. Noninterferometric Phase Imaging with Partially Coherent Light. *Physical Review Letters*, 80(12):2586–2589, March 1998. ISSN 0031-9007. doi: 10.1103/PhysRevLett.80.2586. URL `http://link.aps.org/doi/10.1103/PhysRevLett.80.2586`.

[123] D. Van Dyck, M. Op de Beeck, and W. Coene. A new approach to object wave function reconstruction in electron microscopy. *Optik*, 93:103–107, 1993.

[124] N. Streibl. Phase imaging by the transport equation of intensity. *Optics communications*, 49(1):6–10, 1984. URL `http://www.sciencedirect.com/science/article/pii/0030401884900798`.

[125] DV Sheludko, AJ McCulloch, M Jasperse, HM Quiney, and RE Scholten. Non-iterative imaging of inhomogeneous cold atom clouds using phase retrieval from a single diffraction measurement. *Optics express*, 18(2):1586–1599, 2010.

[126] Chao Zuo, Qian Chen, Weijuan Qu, and Anand Asundi. Direct continuous phase demodulation in digital holography with use of the transport-of-intensity equation. *Optics Communications*, 309:221–226, 2013.

[127] Alexander Kostenko, K Joost Batenburg, Heikki Suhonen, S Erik Offerman, and Lucas J van Vliet. Phase retrieval in in-line x-ray phase contrast imaging based on total variation minimization. *Optics express*, 21(1):710–723, 2013.

[128] Yunhui Zhu, Aamod Shanker, Lei Tian, Laura Waller, and George Barbastathis. Low-noise phase imaging by hybrid uniform and structured illumination transport of intensity equation. *Optics Express*, 22:26696–26711, 2014.

[129] C Ozsoy-Keskinbora, C. B. Boothroyd, R. E. Dunin-Borkowski, P. A. van Aken, and C. T. Koch. Hybridization approach to in-line and off-axis (electron) holography for superior resolution and phase sensitivity. *Scientific Reports*, 4, 2014.

[130] Shirly V. Pinhasi, Roger Alimi, Lior Perelmutter, and Shalom Eliezer. Topography retrieval using different solutions of the transport intensity equation. *J. Opt. Soc. Am. A*, 27.

[131] Colin Ophus and Timo Ewalds. Guidelines for quantitative reconstruction of complex exit waves in hrtem. *Ultramicroscopy*, 113:88–95, 2012.

[132] A. Parvizi, W. V. den Broek, and C.T.Koch. The gradient flipping algorithm: introducing non-convex constraints in wavefront reconstructions with the transport of intensity equation. *Optics Express*, Submitted, 2016.

[133] Michael Reed Teague. Deterministic phase retrieval: a Green's function solution. *Journal of the Optical Society of America*, 73(11):1434–1441, November 1983. ISSN 0030-3941. doi: 10.1364/JOSA.73.001434. URL `http://www.opticsinfobase.org/abstract.cfm?URI=josa-73-11-1434`.

[134] M. Beleggia, M. A. Schofield, V. V. Volkov, and Y. Zhu. On the transport of intensity technique for phase retrieval. *Ultramicroscopy*, 102(1):37–49, December 2004. ISSN 0304-3991. doi: 10.1016/j.ultramic.2004.08.004. URL `http://www.ncbi.nlm.nih.gov/pubmed/15556699`.

[135] Lukas Palatinus. The charge-flipping algorithm in crystallography. *Acta Crystallographica Section B: Structural Science, Crystal Engineering and Materials*, 69(1):1–16, 2013.

[136] Daniel Gabay and Bertrand Mercier. A dual algorithm for the solution of nonlinear variational problems via finite element approximation. *Computers & Mathematics with Applications*, 2(1):17–40, 1976.

Persönliche daten

Name	Amin Parvizi
Geburts-datum	21.09.1984
Staat-sangehrigkeit	Iranisch

Studium

2016-heute	Akademische mitarbeiter bei der Humboldt Universität zu Berlin
2015-2016	Fortsetzung der Doktorarbeit an der Humboldt Universität zu Berlin
2012-2015	Doktorand an der Universität Ulm - Thema: Phase Retrieval Algorithm in Inline Holography
2008–2011	Elektrotechnik, M.Sc., University of Malaya, Malaysia
2002–2006	Elekronik, B.Sc., Azad University, Yazd, Iran
1998–2002	High School, Shiraz, Iran

Berufstätigkeit

2016-heute	Akademische mitarbeiter bei der Humboldt Universität zu Berlin
2015-2016	Wissenschaftlicher Mitarbeiter an der Humboldt Universität zu Berlin
2012-2015	Wissenschaftlicher Mitarbeiter an der Universität Ulm
2006-2008	Projekt Manager bei Furuzan Niru in Shiraz, Iran

Sprachen

Deutsch	Gute Kenntnisse (B1 Zertifikat)
Englisch	Verhandlungssicher
Persisch	Muttersprache
Türkisch	Grundkenntnisse

Publications

2016 A. Parvizi, W. V. den Broek, and C.T.Koch. Recovering low spatial frequencies in wavefront sensing based on intensity measurements. *advanced structural and chemical imaging*, Submitted, 2016

2016 A. Parvizi, W. V. den Broek, and C.T.Koch. The gradient flipping algorithm: introducing non-convex constraints in wavefront reconstructions with the transport of intensity equation. *Optics Express*, Submitted, 2016

2015 Parisa Bakhtiarpour, Amin Parvizi, Martin Müller, Mohsen Shahinpoor, Othmar Marti, and Masoud Amirkhani. An external disturbance sensor for ionic polymer metal composite actuators. *Smart Materials and Structures*, 25(1):015008, 2015

2015 Kyung Song, Christoph T Koch, Ja Kyung Lee, Dong Yeong Kim, Jong Kyu Kim, Amin Parvizi, Woo Young Jung, Chan Gyung Park, Hyeok Jae Jeong, Hyoung Seop Kim, et al. Correlative high-resolution mapping of strain and charge density in a strained piezoelectric multilayer. *Advanced Materials Interfaces*, 2(1), 2015

2015 A Parvizi, J Müller, SA Funken, and CT Koch. A practical way to resolve ambiguities in wavefront reconstructions by the transport of intensity equation. *Ultramicroscopy*, 154:1–6, 2015

2013 Peyman Jahanshahi, Amin Parvizi, and Faisal Rafiq Mahamd Adikana. Three-dimensional modeling of surface plasmon resonance based biosensor. In *European Conference on Biomedical Optics*, page 880109. Optical Society of America, 2013

2009 SW Harun, R Parvizi, XS Cheng, A Parvizi, SD Emami, H Arof, and H Ahmad. Experimental and theoretical studies on a double-pass c-band bismuth-based erbium-doped fiber amplifier. *Optics & Laser Technology*, 42(5):790–793, 2010

2009 Amin Parvizi, Mehdi Hassani, Amir Hossein Mehbodnia, Saad Makhilef, and MR Tamjis. Adaptive network-based fuzzy inference approach of estimating of torque for 8 6 switched reluctance motor. In *Technical Postgraduates (TECHPOS), 2009 International Conference for*, pages 1–4. IEEE, 2009